Hiroshima University
Graduate School of Engineering
Department of System Cybernetics

Study of Dynamic Control for Balanced Walking of Humanoid Robots

PhD Dissertation

SUNANDAN DUTTA

March 2021

Study of Dynamic Control for Balanced Walking of Humanoid Robots

（ヒューマノイドロボットのバランス歩行のための動的制御に関する研究）

by

SUNANDAN DUTTA

D174932

A Thesis
Submitted to the Graduate School of Engineering
Hiroshima University
in partial fulfillment of the requirements for the degree of
Doctor of Philosophy
(Electrical Engineering)

Hiroshima University, Japan

March 2021

Hiroshima University
Graduate School of Engineering

Kagamiyama, 1-4-1 Higashi-Hiroshima City
Hiroshima, Japan 739-8527
TEL: +81-82-424-7505
FAX: +81-82-422-7039

CERTIFICATE

To whom it may concern

We hereby certify that this is a copy of the original doctoral thesis by Mr. SUNANDAN DUTTA. This doctoral thesis was successfully defended and officially accepted in the partial fulfillment of the requirements for the degree of Doctor of Philosophy.

Advisory and Examination Committee:

Prof. Naoto Yorino
Prof. Katsuhiko Takahashi
Prof. Ichiro Nishizaki
Prof. Makoto Tsukai

OFFICIAL SEAL OF
THE GRADUATE SCHOOL

_____
Atsushi Sugeta, Dr.
Dean, Graduate School of Engineering, Hiroshima University

Abstract

Humanoid Robots are important targets by roboticists to automate the human-centered society. Therefore humanoid robots are most popular research topics in the field of robotics. At the same time it is very challenging to implement a humanoid robot in the real world where the environmental factors like surface profile, rigid obstacles pose serious problems. Also, the dynamics of humanoid robot is highly nonlinear and difficult to control. Due to the presence of multiple joints, it is very difficult to implement control system hardware to control all joints at a time. Also the computational complexity for this implementation is too large to be implemented using open-source hardware platform, making the development very much restricted to laboratory rooms.

Therefore a lightweight humanoid robot is very much suitable over a heavy human-size robot for analyzing the postural stability of the robot on inclined surface. KONDO KHR-3HV robot of 1.5 Kg weight and 0.6m height is used for the investigation of the postural stability on an inclined surface. A force-sensor based position control system is proposed. The ankle-pitch motor is controlled by force-sensor feedback from the robot foot. This control system enables the robot to walk on inclined surface up to 8.5°. Beyond 8.5°, a gyro based control system is designed control the hip motor allowing the robot to stabilize its posture up to 10° of surface inclination. Theoretically the Inverted Pendulum Model is extended to include the effect of the surface inclination in order to model the stability of the robot. The model predicts the effect of feedback gain and initial motor-rotation in order to reduce the maximum overshoot in the transient response of the angular-pitch velocity of the robot. After implementing static stability control system for the robot on inclined surface, the dynamic walking of the robot was investigated on the inclined surface. In that case a gyro sensor was used to control the ankle-pitch motor up to a surface inclination of 8.88°. The torso-angular velocity is analyzed in both time domain and frequency domain for studying the vibration in the robot. Vibration in the robot is observed to be an effect due to the harmonics of the fundamental walking frequency of 1.73 Hz. In addition to the harmonics, the damped natural frequency due to the gyro feedback effects the frequency response of the robot. This causes increased vibration when the feedback control is introduced. One way to reduce the vibration is to increase the friction between the robot feet and surface. Increasing surface friction allows the robot to walk more stably with reduced vibration.

Acknowledgement

First I acknowledge my supervisor Prof. Naoto Yorino for giving me this opportunity to be a part of Electric Power and Energy System Laboratory (EPESL), Graduate School of Engineering, Hiroshima University. I would like to express my gratitude for his continuous support and guidance during my doctoral work. Also I would like to express my gratitude to my sub-advisors Prof. Katsuhiko Takahashi, Prof. Ichiro Nishizaki and Associate Professor Tsukai Makoto.

I would like to pay my sincere regards and gratitude to Prof. Mitiko Miura-Mattausch and Prof. Hans Jürgen Mattausch for their epitomized guidance to carry out the research on light-weight humanoid robot in HiSIM Research Center, Hiroshima University. Also I thank Associate Professor Tapas Kumar Maiti of DAIICT, India (former Associate Professor at Hiroshima University) for guiding me through the basics of robotics and preparation of experimental setup, in the early years of my doctoral work. I would like to thank my colleagues at HiSIM Research Center for their immense support which helped me to finish my doctoral thesis.

I would like to thank TAOYAKA Program for their financial support to carry out the research work for the thesis. Also, it was TAOYAKA program which gave me rare opportunities to develop robots based on the requirements of the society. I am thankful to them for teaching me the concept of "Reverse Innovation".

Last but not the least, I would like to express my love and gratitude to my parents, family members and friends for their constant support though the turbulent days of doctoral study and research.

SUNANDAN DUTTA

2021

Table of Contents

List of Figures

List of Tables

Abbreviations

IPM	Inverted Pendulum Model
ZMP	Zero Moment Point
MEMS	Micro-electromechanical system
SSP	Single Support Phase
DSP	Double Support Phase
COM	Center of Mass
COP	Center of Pressure
PD	Proportional-Derivative
PID	Proportional-Integral-Derivative

Chapter 1: Introduction

1.1 Research Background

Robots are important means to sustain and to develop a comfortable society [1-6] to live in. The intensive utilization of robot is being realized to reduce the necessity of the human efforts in different fields like agricultural [1,2], inspection and maintenance [3,4], or rescue operations [5-7]. The basic philosophy for the research, as followed in this thesis, is 'Reverse Innovation' [8] - which allows development of any technology according to the need of human beings. But at the same time Isaac Asimov's "Laws of Robotics" [9] are strictly followed as far as the consequence of the technology is concerned. In this chapter, three basic questions are answered:

1. Why a humanoid robot is chosen for the research purpose?
2. What field of application inspired this development of the humanoid robot?
3. What type of humanoid robot is chosen or in other words, what is special about the physical characteristics of the humanoid robot used for the research work?

1.1.1 Why is a humanoid robot chosen?

The working environment around us is built by human beings. The interior of houses and buildings, the staircase, the lanes between buildings, the walking path beside the driveways and many more – are specifically designed and planned especially for human dwellers. Then comes the tool used by the human beings. The tools are invented and designed so that they can be easily handled and operated by human beings. Shuuji Kajita has mentioned three important features of the humanoid robots in their book *Introduction to Humanoid Robotics* [10]. If those features are carefully followed, then the only robot that can work in human-based environments as it is and use the tools made for humans, is a humanoid robot having a "human like shape". So, the best robot to apply in our daily activities is a humanoid robot.

1.1.2 What field of application?

Humanoid robots are finding various applications in our daily life, but one potential application is post-disaster survey and rescue [6]. 'Human-shape' and human-sized robots with weight comparable to that of an adult human being are applied to similar situations. This is observed in both simulation platforms like Choreonoid [11] and real-time testing

like the application of the robot to simulated environments of DARPA Robotics Challenge (DRC) [12].

If those environments are carefully observed, most of the simulation or real-time experiments are carried out on a concrete surface which is strong enough to bear the robot load. That is quite usual in case of nuclear power plant or inside a mine. At the same time it must be kept in mind that the rate of damage to the Japanese household is highest due to various natural disaster as compared to the nuclear power plants or other industrial establishments. For example let's consider the situation of Japanese wooden houses. Okada and Takai [13] documented the damage patterns of the wooden houses due to earthquake. It is observed that significant number of effected houses are partially damaged where the supporting columns and beams are severely damaged. This reduces the load-bearing capacity of the supporting-structure.

During the post-disaster surveillance and rescue work it is very dangerous to send human rescuers to those partially damaged structures because the weight of human rescuers can cause further damage to the structure. Also it may cause injury even death to the rescuers and also to the trapped human life (if any) under the damaged structure. Aftershock effects may also cause injury to the human rescuers working in the affected environment. Therefore keeping in the mind the severity of the damaged structure, instead of human rescuers it is wise to send humanoid robots. Additionally considering the load-bearing capacity of the partially-damaged structure, the weight of the robot must be low. This

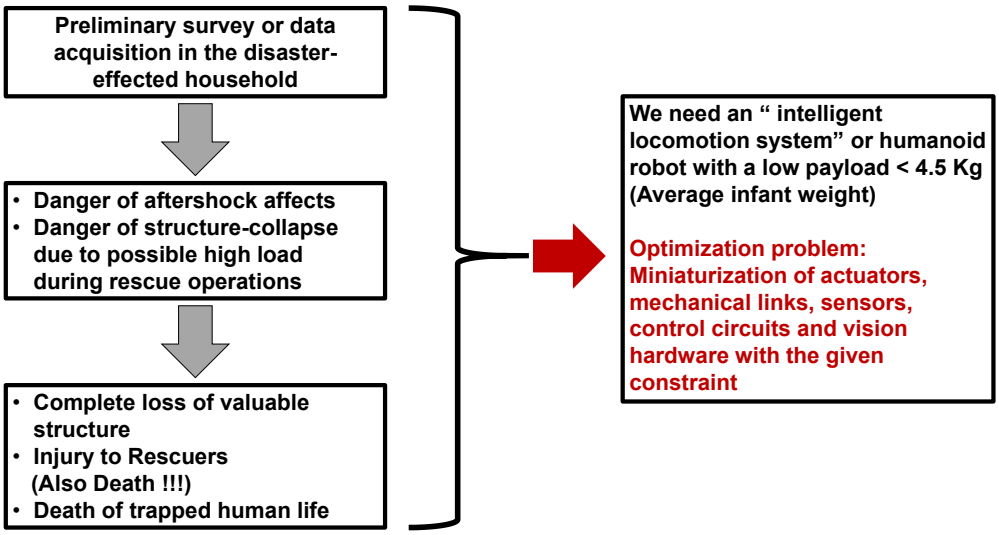

Fig. 1.1. The partially damaged environment inside a Japanese wooden house requires light-weight 'intelligent' humanoid robot for risk-free preliminary survey and data acquisition.

situation justifies the work carried out with light-weight humanoid robot in this thesis. An overall picture of the situation discussed above, is shown in Fig.1.1.

1.1.3 What type of humanoid robot is used?

Following the discussion carried out in previous section, the weight of the robot is determined to be very lower than the weight of an adult human or conventionally developed humanoid robots. This is the basic reason behind the working on a light-humanoid robot. In this thesis a light-weight humanoid robot of 1.5 Kg weight [14] is used.

It is important to revisit the features of the humanoid robots as discussed by Kajita et al. [10]. The third feature says that "humanoid robots have human-like shape". Sometimes research works on light-weight humanoid robots or "toy robots" are not considered to be "mainstream robotics-research" by many members of the research community. But based on the established and accepted features of humanoid robots it can be argued that light-weight toy-sized robots are also humanoid robots even though they are not human-sized. This is because Kajita et al emphasizes on the 'shape' of the robot, rather than 'size'.

1.2 Research Objectives

In the previous section the background of the research is presented and three basic questions are investigated and answered. The humanoid robots in general, places various challenges in front of the research community [15]. The dynamics of a humanoid robot is highly nonlinear leading to unpredictable behavior of the robot. Moreover it is a multivariable system which makes the design of the motor control system highly complicated to implement. Above all the changing surface profile poses to be a major problem for a terrain-blind (without vision based feedback) robot.

Also due to the light-weight feature of the robot body, additional problem like vibration is observed for the robot walking [16]. The primary objective of this thesis is to "stabilize the light-weight humanoid robot on an inclined surface".

Question may arise, why is an inclined surface chosen? Three main reasons can be given as follows:

1. Inclined surface is a very common and structured surface-profile often found in our surrounding environment.
2. Inclined surface modifies the gravity force on the robot-body allowing to study the gravity compensation needed to stabilize the robot-posture.

3. Surface friction due to inclined surface effects the robot-dynamics.

To achieve the objective mentioned above, the investigation presented in the thesis is divided into two main parts – static stability control and dynamic stability control.

1.2.1 Static stability control

Static stability control discusses the postural stability of the robot when the robot is not walking. For a robot standing on an inclined surface, there is a threshold surface inclination beyond which the robot with the reference posture will fall. In static stability control, the control strategies for keeping the robot-posture stable beyond that threshold surface inclination are discussed.

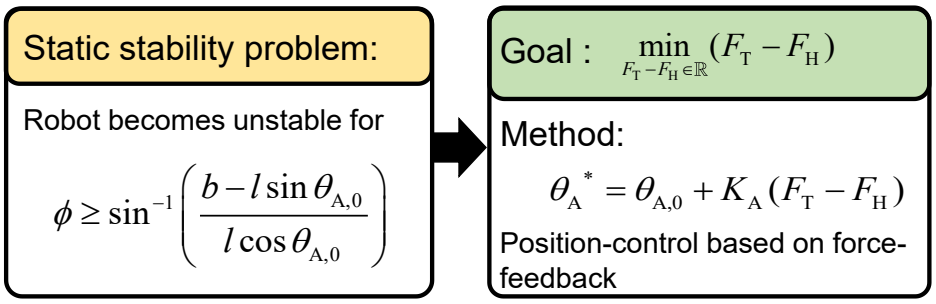

ϕ : surface inclination
$\theta_{A,0}^*$: corrected reference ankle-pitch motor angle
$\theta_{A,0}$: reference ankle-pitch motor angle
K_A : proportional feedback gain
F_T, F_H : toe and heel force at the robot foot respectively
b : length of the robot foot
l : height of the robot's center of mass from ankle

Fig. 1.2. Robot standing on an inclined surface faces the 'static-stability problem' which means it can continue to stand with the same posture up to a certain surface inclination. Beyond that surface inclination the robot-posture must be controlled to ensure static stability.

While investigating the static stability of the robot on inclined surface, it is found that the gyro-sensor based feedback control is necessary to control the robot posture beyond a certain surface inclination [17]. Therefore the working principle of the vibratory-gyro sensor is studied and an electromechanical model of the gyro sensor is proposed [18]. This allows the researcher to incorporate the circuit behavior of the sensor into the dynamics of the robot. The gyro-sensor model is used to simulate the robot-dynamics when the robot is applied with an external push-force [19]. The robot-posture is controlled based on the ankle-strategy [20], where the ankle-pitch motor angle is controlled based on the angular

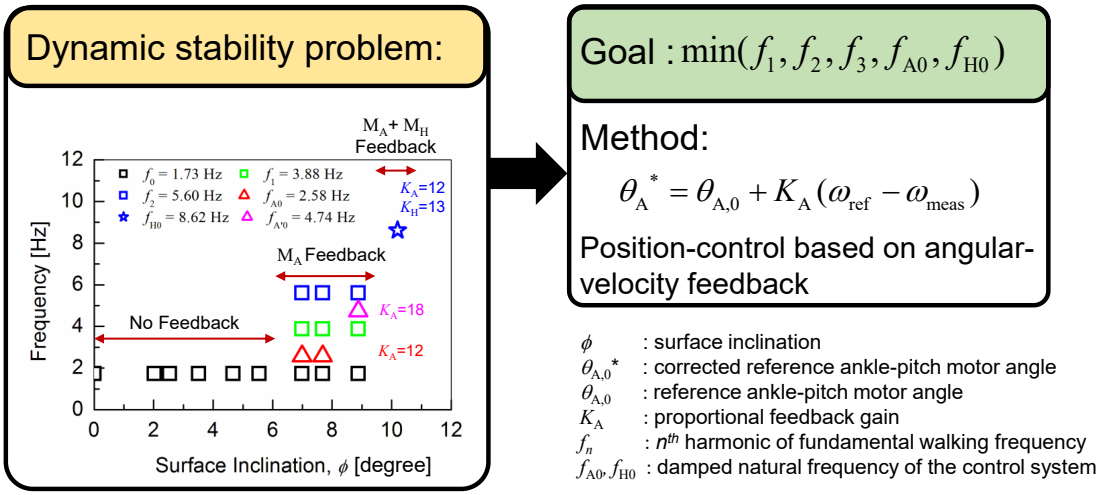

Fig. 1.3. Robot walking on an inclined surface faces the 'dynamic-stability problem' which means additional frequency components are observed in addition to the fundamental walking frequency. The goal is to reduce the high-frequency contribution making the robot walking stable.

velocity feedback measured by the gyro sensor. This concludes the static stability control part of the thesis. An overall picture of the static stability control is shown in Fig. 1.2.

1.2.2 Dynamic stability control

In this thesis, dynamic stability explains the stability of the robot when the robot walks on the inclined surface. When a robot walks, there exists is a gait cycle (and corresponding fundamental walking frequency f_0). The fundamental walking frequency is observed when the walking pattern of the robot is analyzed in the frequency domain (hereafter f-domain) [16]. Here the walking pattern is characterized by the pitch-angular-velocity of the robot torso. The angular-pitch velocity is measured by a gyros sensor integrated to the torso of the robot.

When the robot walks down an inclined surface, it is observed that the robot can walk with the pre-programmed walking pattern up to a critical surface inclination. Beyond that surface inclination, the posture of the robot (ankle-pitch motor and hip-pitch motor) is controlled by the pitch-angular velocity measured by the gyro sensor.

Beyond the critical surface-inclination, vibration is observed in the light-weight humanoid robot, which changes the walking pattern of the robot. The change in the walking pattern with increasing the surface inclination, can be explained by analyzing the measured angular-pitch velocity in the f-domain. Vibration causes instability in the robot-walking.

The instability can be explained and reduced by identifying the frequency peaks. This is novel approach where the stability of the robot is analyzed in frequency domain solely depending on the analysis of one physical quantity: the pitch-angular velocity of the robot. The position of the contributing frequency-peaks are determined by the surface inclination and the magnitude of the feedback gain. The origin of the frequency peaks can be explained by analyzing the response of a second-order velocity-feedback control of a nonlinear inverted pendulum system. The model gives a method to reduce the high-frequency contribution reducing the vibration in the robot, making the walking stable. An overall picture of the dynamic stability control is shown in Fig. 1.3.

1.3 Thesis Outline

The thesis consists of six chapters. The research topics discussed in the chapters are summarized as follows:

- **Chapter 1** discusses the basic objective of the work outlining a brief overview of the design and application of the humanoid robot. It discusses the motivation of the work and concluding with the outline of the thesis.

- **Chapter 2** discusses the previous work carried out in the field of humanoid walking -stability. Two main aspects of the robot stability are discussed namely, the control methods for postural stabilization and the vibration control in humanoid robots.

- **Chapter 3** presents the investigation of the static stability of the robot. The static stability of the robot is analyzed on an inclined surface. The proposed position-control system is based on the force-sensor feedback from the robot feet. The robot can stabilize its posture on inclined surface up to a surface inclination of 8 degrees. Beyond 8 degrees, a gyro sensor based position control system is used to stabilize the robot on inclined surface up to a surface inclination of 10.2 degrees.

- **Chapter 4** discusses the application of gyro sensor to the humanoid robot. An electromechanical model of the gyro sensor is experimentally verified from the dynamic characteristics of analog gyro sensor KRG-4. The gyro sensor model is used to model the push recovery strategy for the robot on a plane surface. The model was experimentally verified by the push-recovery experiments.

- **Chapter 5** discusses the robot walking control based on a novel gyro sensor based feedback control system. The achievements are divided into two parts. The first part discusses the walking pattern modelling of the robot and the frequency response of the robot walking on an uninclined surface. In order to stabilize the robot walking on an inclined surface, a gyro-sensor based feedback control systems is proposed. The experimental results shows that as the surface inclination is increased higher harmonics of the fundamental walking frequency and damped natural frequency of the control system effects the robot walking. This increases the vibration in the robot, thus making the robot walking unstable. So an optimization of the controller gain is implemented based on the tradeoff between the surface friction and the vibration. Therefore adjusting the controller gain, the vibration is reduced.

- Chapter 6 provides a conclusion of the thesis, where the contributions of the study are discussed. In addition, some recommendations for future research are presented.

A unified picture of the organization of the thesis is given below. The author considers it will be helpful for the readers to understand the workflow and major contribution of the thesis. In the Fig.1.4 the contents of the thesis are divided into three parts, viz.

- Part I. Problem statement,
- Part II. Static stability control
- Part III. Dynamic stability control

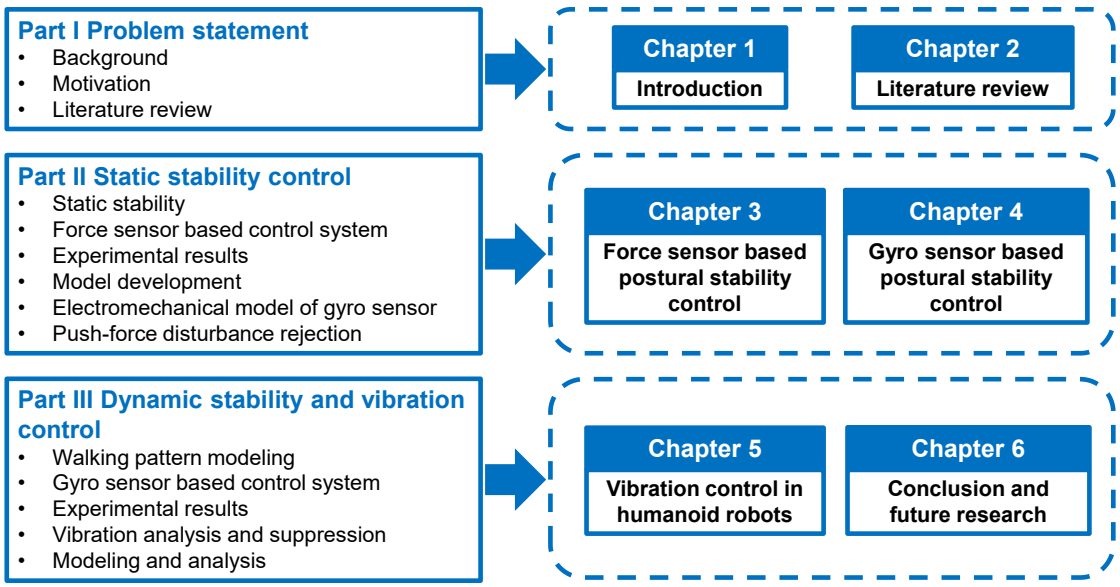

Fig. 1.4. A unified picture of the organization of the thesis is given for the readers to understand the workflow and major contribution of the thesis.

Chapter 2: Literature Review

This chapter discusses the literature review on the stability of humanoid robot. The organization of the chapter is as given below. In section 2.1 a survey of the control methods for static stability control of the humanoid robot is given. The survey is followed by the outcomes and drawbacks of the control methods when their applicability to a light-humanoid robot is considered. At the end the originalities of this thesis in the field of static stability of the light-weight humanoid robot is listed. The originalities are discussed in detail in the following chapter 3.

Section 2.2 discusses the theoretical framework and literature over which the proposed electromechanical model for gyro sensor is developed. The electromechanical model of the gyro sensor is discussed in chapter 4. As introduced in previous chapter, the model for gyro sensor is used to analyze the dynamics of the robot when applied with a push-force. Section 2.3 presents the literature survey on the push-force disturbance rejection control. The push-force dynamics of the robot is discussed in the latter half of chapter 4.

At the end, in section 2.4 the previous works on dynamic stability of humanoid robot is discussed followed by the brief introduction to the originalities presented by this thesis in chapter 5.

2.1 Background of Static Stability

The robotics community have achieved large progress in the in the field of intelligent humanoid robots for using at various environments under various situations [21-24]. Accurate sensing of the surface-profile information [25-32] is required for controlling the walking of the robot on a given surface. So far the developments extensively use the terrain-information to stabilize the robot [28-29]. The information from the environment is collected by vision based sensors [33-34]. So, “blind” humanoid-robot i.e. without any camera to sense the surrounding, is a worst-case scenario for robot-posture control while walking [30-32].

So far the publications on the ‘blind’ humanoid robots have focused on the walking analysis [35-38]. Model based control like Zero Moment Point (ZMP) control was introduced to analyze the stability of the humanoid robot [10, 39]. This control system was used in industry-level humanoid robots like HONDA humanoid robot [40] or the HRP

series of AIST-Japan [41,42]. However, unlike the well-solved control problems as those for robot manipulators [43,44], the development of robust control for walking of humanoid robot has not reached practical implementation till now. Recently, control systems developed on the principles of Machine Learning (ML) algorithms, such as supervised-learning algorithms [45-47] and reinforcement-learning algorithms [48,49], are being applied to biped-stability control [35], [37], [39], [50-52] to achieve better walking stability and improving the agility of the humanoid robots. To implement such ML-based control methods in light-weight robots, one faces major problems of increased complexity of hardware. Unnecessary hardware payload increases the weight on the robot making it lesser suitable design for potential applications. Therefore, it is difficult to implement such ML-based control methods into a commercial low-cost open-source hardware platform and then integrate the platform to the light-weight robot. In summary, the previously proposed walking-control methods cannot be use to efficiently realize the balancing of the light-weight humanoid robots. Further, the balancing of light-weight robots on an inclined surface is more difficult as compared to that of a heavy-weight robot [30-32]. This largely depends on the dimension of the barrier or surface geometry. Considering the scalability rules [53], very few research works on balancing the light-weight humanoid robots have been reported [54-55] so far. Tamura *et. al.* [54] proposed a method to control the stability of light-weight humanoid robots. This avoids the calculation-overhead and also the effect of noise in the measurement of the ZMP. Implementation of the proposed control system showed, that the robot can only surpass an object of 0.5 cm height thus avoiding the obstacle, which is quite inadequate with respect to the more realistic uneven surfaces and obstacles. Moreover, the control scheme of [54] was only limited to surpassing obstacles and not applied to any kind of inclined surfaces (upslope or downslope). Yi *et. al.* [55] proposed a ZMP-based on-line-learning system, where the surface inclination is calculated while walking and the joint angles are adjusted to stabilize the posture robot. They have tested the control system for an uneven surface with 6% finite height change. But in that case effects of inclined surface on static stability and walking dynamics of the humanoid robot are not discussed.

The investigation presented in this thesis focusses on the development of low-cost, robust yet easy-to-control hardware of humanoid-robot-stability control. Considering the above survey, the novel contributions to this section include:

1. Force-sensor are attached to heel and toe of the robot-feet. The difference between the toe and heel forces are measured. This difference is measured and

plotted as a function of surface inclination. Based on the trend of the force-difference, a critical surface inclination is determined. Below the critical surface inclination, no sensor-based posture control is required.

2. Inverted Pendulum Model (IPM) [56-58] is extended to incorporate the information of the surface inclination.
3. Based on this extended IPM, a force sensor based control system is proposed for ankle-pitch-motor.
4. Compared to the conventional ZMP control [59], the proposed control system does not require the calculation of ZMP, thus reducing calculation overhead and noise. It is observed that the ankle-pitch motor plays important role in posture stabilization [56-57, 60] of humanoid robot, only ankle-pitch-motor is controlled. This further reduces calculation overhead as compared to the conventional approach based on inverse kinematics [10].

2.2 Electromechanical Modelling

The control systems developed so far incorporates sensors to measure the disturbances caused by the environment. Therefore the circuit level analysis of these components are very much necessary prior to the overall analysis of the robot. This robot components like gyro sensors are generally implemented in the robot simulator as a mathematical functions, which do not analyze the circuit-level behavior of the sensor. The performance of the robot in a macroscopic level is largely guided by the microscopic behavior of the electronic components. Therefore, analysis of these components are needed for developing a specific robot system.

Lots of research efforts are given mainly to develop the efficient control algorithms for robot-system controller [61]. But, the hardware design of the controller and peripherals for the robust performance of the robot system are analyzed to a much lesser degree [10, 62-63]. In this thesis special focus is given on the circuit level analysis of the robot components and how the circuit level performance effect the overall dynamics of the robot. This is done to bridge between the electronic behaviors of the robot components to the dynamic behavior of the multibody systems like humanoid robot. The future purpose of this work is to incorporate the circuit level description into the robot multibody physics simulators.

2.3 Push-Force Recovery

Hemami *et.al.* [57] discussed the static stability of an inverted pendulum in order to model robot walking based on the principles of the inverted pendulum. The static stability margin [57] of a robot is calculated from the potential energy of the footed-inverted pendulum. The margin is independent of the mass of the robot and depends on the physical parameters of the robot like height of the center of mass and length of the foot. Vukobratovic *et.al.* [59] introduced the ZMP as a criteria to measure the stability-margin for humanoid robots. The ZMP control is used in order to control the robot-motor angles based on the feedback of ground reaction force [10]. However, the control strategies vary depending upon the magnitude of the force exerted on the robot body. The most basic strategy for canceling disturbance due to small-magnitude force, is compensating the torque at ankle-pitch motor. Hemami *et. al.* [64] discussed the ankle strategy considering an inverted pendulum model. The hip strategy i.e. compensating the torque at hip motor was introduced considering the inverted pendulum model of 2-degrees-of-freedom (DOF). Hoffmann [65] argued that basic ankle strategy is realized with adjusting the Center of Pressure (COP) or ZMP by changing the tangential ground-reaction force with the ankle motor. Therefore it is observed that the control strategies indicates towards the utilization of ZMP approach only. With the hip strategy, larger tangential ground-reaction force is generated causing postural stabilization at higher disturbance force. In this thesis as a primitive step, the ankle strategy is implemented for the light-weight robot based on the pitch-angular velocity of the robot-torso. The use of the gyro sensor instead of force sensor (for calculating the ZMP) reduces the computational complexities as carried out in human seized robot.

2.4 Walking Dynamics and Gait Analysis

The most important feature of an ideal human-walking pattern or “gait pattern” is observed in its periodicity [67], and this periodic gait-pattern is defined from the physiological point of view. Various experiments have been carried out by prosthesists, to assess the human gait-pattern [67-77] and include an analysis of basic parameters, like velocity or number of steps per unit time. [68]. The joint angle of the robot leg and the ground-reaction force are most often studied among all the different parameters, to characterize the periodicity of the human gait [67-71]. For the characterization purpose, a frequency analysis of these measurable quantities is often carried out using the Fourier

series expansion [69-71]. However, such Fourier analysis was in most cases limited to the study of human patients, to determine the change in their walking dynamics due to various physical problems and diseases [74]. With the development of an Inertial Measurement Unit (IMU), based on a Micro Electro-Mechanical System (MEMS), the studies of orientation and force at each of the joint angles for human beings or humanoid robots have become more advanced [76-78].

To analyze the periodicity of any physical signal, frequency-domain analysis is considered to be a fundamental approach. In the humanoid-robotics field, the Fourier series expansion is applied to generate the gait pattern for the robot's basic walking motion, which can be modeled as a superposition of sinusoidal joint-angle variations [79,80]. Kajita et al. [81] used frequency-domain analysis to suppress vertical vibrations in the HRP-4C robot. In [82], a frequency-domain classification of surfaces, based on the robot vibrations, is reported but not yet applied to the humanoid-robot control. Liu et al. [83] designed a vibration-reduction controller for elastic joints, implemented in a humanoid manipulator. The terminologies of resonant and anti-resonant frequencies with respect to the compliance modeling in motors were discussed in detail, highlighting the frequency-domain analysis of the vibrations. But the control system was only applied to static manipulators, while the vibration effect on humanoid-robot dynamics was not reported. Very few works on the stability of humanoid robots, which exploit the Fourier analysis of the gait-data, have been reported. Kim et al. [84] reported vibration responses during leg lifting of a humanoid robot in the swinging phase, but did not adequately discuss the overall effect on the gait data, e.g., on the COM position or on the angular-pitch velocity components of robot's COM.

Consequently, the purpose of the dynamic stability control in this thesis is to analyze the balancing mechanism of a humanoid robot on inclined surfaces, to achieve stable walking with the help of motor-feedback control and Fourier analysis of the robot's angular-pitch velocity, which is measured for one gait-cycle during the experiments. The angular-pitch velocity of the robot is measured while walking on different surface inclinations and analyzed in the frequency domain, where the origin of the observed periodicity disturbances of the robot-gait is investigated. The novel contributions of this part of the thesis include:

- Proposal of a gyro-sensor-based feedback-control system to control the ankle-pitch and hip-pitch motors of the robot for stable walking on inclined surfaces. The control system enables the robot to walk stably on a downslope surface of inclination up to 10.2°. The feedback controller is easy to implement in a commercial, low-cost, mass-

produced and open-source hardware platform that can be integrated easily into a light-weight humanoid robot.

- The ankle-pitch and hip-pitch motors play a significant role in posture stabilization [57,10]. Therefore, initially for smaller surface inclinations, the ankle-pitch motor is controlled and for larger surface inclinations both ankle-pitch and hip-pitch motors are controlled. This reduces the computational complexity compared to the inverse-kinematics-based approaches in conventional ZMP-based control [10, 85, 86].
- The angular-pitch velocity of the robot is considered to be a characteristic of the robot-gait, is measured by the gyro sensor for the walking robot and is analyzed in the frequency domain. A novel usage of the Fourier analysis for the angular-pitch velocity is proposed to determine the cause of postural instability on inclined surfaces. Also, the effect of the feedback gain on the robot gait on inclined surfaces is analyzed.
- It is experimentally observed that increased friction between robot feet and inclined surface reduces the robot vibrations at larger surface inclinations. The results of robot-walking experiments with increased friction represents an optimization approach for the feedback gain to reduce vibrations in the robot at increased surface inclinations.
- The IPM, used to model the robot walking, is extended for inclined surfaces. An additional gyro-sensor-based feedback loop is included in the model to explain the Fourier response of the angular-pitch velocity. Further, the IPM is extended to include the nonlinearity, induced by the surface inclination, to explain the harmonics observed in the Fourier Transform of the angular-pitch velocity.

Chapter 3: Force Sensor Based Postural Stability Control

3.1 Introduction

In this chapter the force sensor based static stability control method is discussed. For analyzing the static stability the light-weight humanoid robot KONDO KHR-3HV [14] is integrated with force sensors on heel and toes of each foot as shown in a schematic of the robot in Fig. 3.1. This is done to measure the heel and toe forces on each foot. Robot balancing experiments are carried over to measure the forces on the toe and heel. Based on the experimentally-measured forces the posture-control system is developed for the robot, standing on an inclined surface.

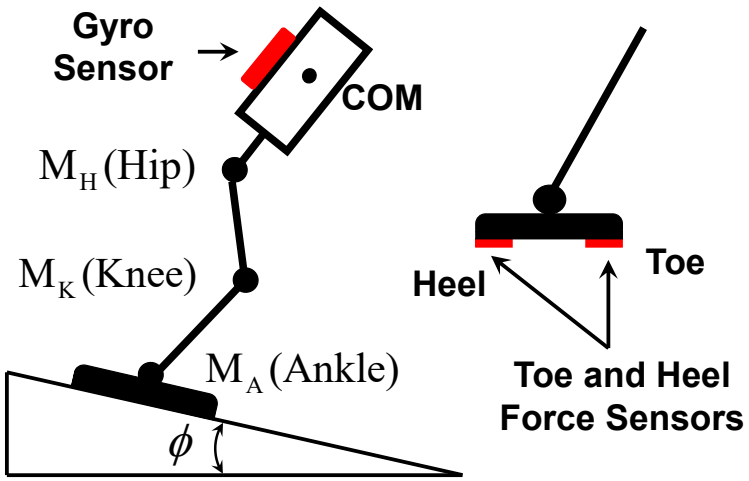

Fig. 3.1. Experimental setup for robot-walking experiments on an inclined surface.

Table I. KONDO KHR-3HV Robot Physical Parameters

Parameter	Unit	Value
Height of Robot	m	0.4
Height of Robot COM	m	0.3
Length of Robot Foot	m	0.12
Mass[+]	Kg	1.5
Degrees of Freedom*	-	17

[+]The mass of the robot is measured after integrating sensors and the controller in the backpack.
*The degrees of freedom of a robot is equal to the number of motors used in the robot.

The chapter is organized as, section 3.2 discusses the experimental setup and the static experiments carried out with the light-weight humanoid robot on inclined surfaces. Then the experimental results are discussed in detail. In section 3.3, the Inverted Pendulum Model (IPM) is extended to model the robot and to incorporate the surface inclination in order to explain the experimental results. The hardware of the force sensor based feedback control system and the necessity of a gyro sensor to stabilize the robot at higher surface inclination is discussed in section 3.4. Section 3.5 concludes the chapter highlighting the outcomes of the static stability experiments.

3.2 Robot Balancing Experiments

A commercial light-weight humanoid robot KONDO KHR-3HV is used [14] in the experiment. The investigation for measuring the characteristics for robot stability is carried out with the robot (see Table I for the physical parameters of the robot). The robot has 17 motors, out of which 3 motors for each leg are used to realize the basic walking of the robot. A schematic representation of the robot with these 3 motors (M_A=Ankle-pitch motor, M_K=Knee Motor and M_H=Hip-pitch motor) on each leg are shown in Fig. 3.1.

3.2.1 Experimental setup

Two resistive force sensors (toe and heel) are attached under the bottom of each foot, as shown in Fig. 3.1. In order to analyze the balancing mechanism of the robot, a surface is inclined by an angle ϕ. The force on each sensor is measured. The surface inclination is gradually increased from 0^o to around 10^o. The experimental setup is shown in Fig.3.2 and the experiments are performed in following three stages:

1. The toe and heel forces are measured using the force sensors when the robot is standing on the inclined surface.
2. Due to increasing the surface inclination, the robot becomes unstable at a certain surface inclination. Beyond that the ankle-pitch motor (M_A) is rotated based on the difference between the toe and heel forces. The ankle rotation makes the robot posture stable.
3. At higher surface inclination of around 8.88^o, the robot cannot stand solely based on the compensating torque at the ankle-pitch motor. So, the hip-pitch motor (M_H) is also rotated according to the angular-pitch velocity of the robot-torso measured by the gyro-sensor. This further allows the robot to stand stably at higher surface inclination around 10^o.

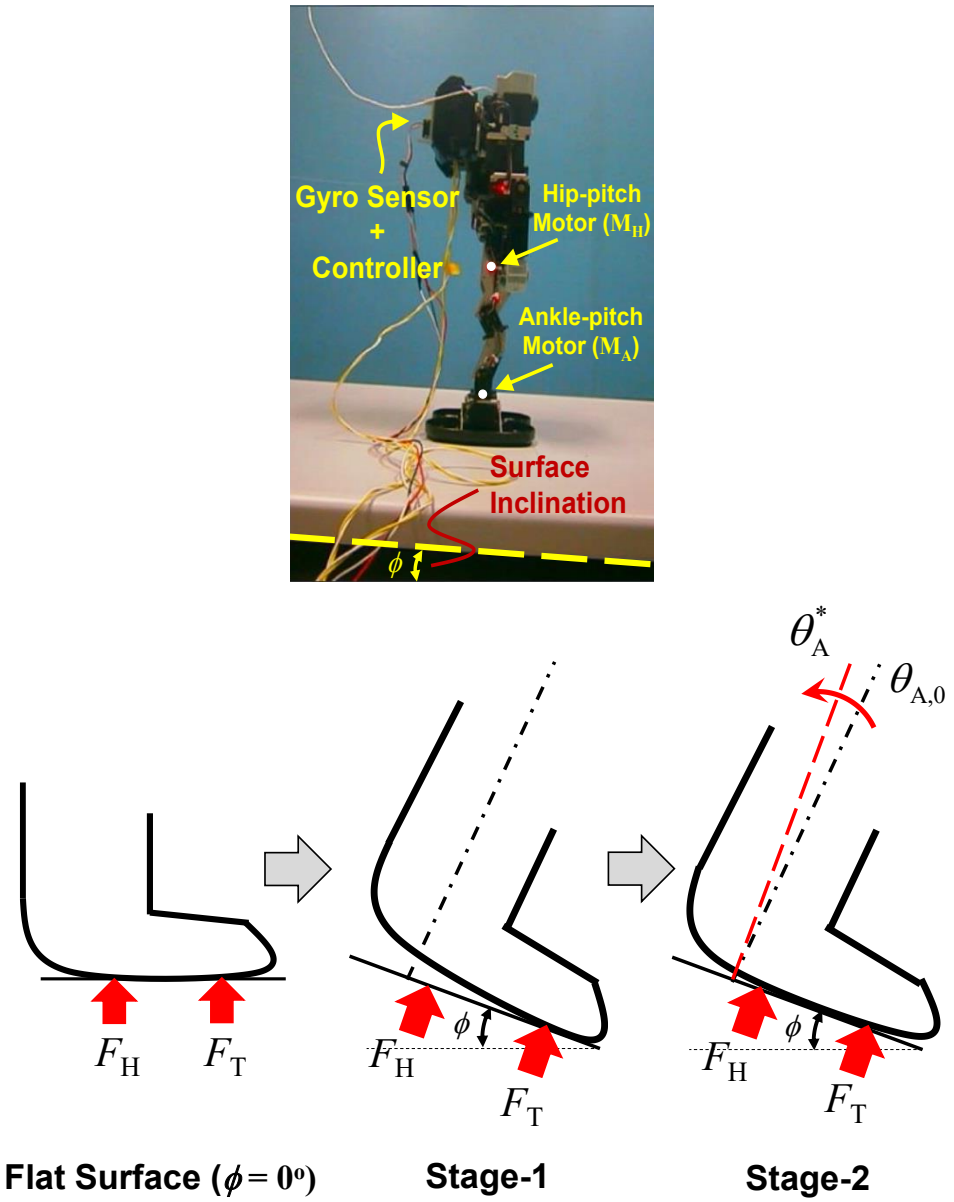

Fig. 3.2. Measurement setup (top) for the robot experiments and the stages of robot control carried out during the experiment (below).

3.2.2 Experimental Results

Fig. 3.3 schematically explains the Single Support Phase (SSP) and the Double Support Phase of the robot walking. The robot is said to be in DSP when the robot is standing on the inclined surface supporting on both feet and in SSP when the robot stands solely supporting on one leg while lifting the other. In this investigation, the SSP of the robot is considered. Fig. 3.4(a) gives toe and heel forces on the left leg as a function of time, when

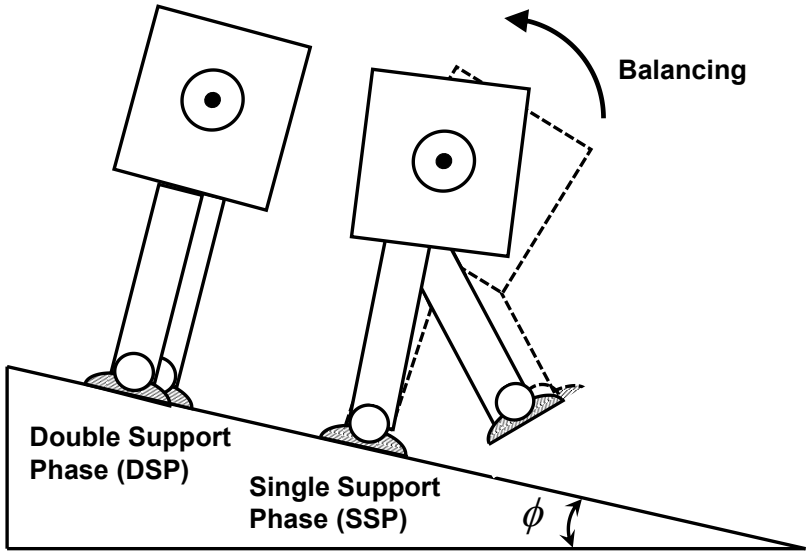

Fig. 3.3. The experiments are carried out for the Single Support Phase (SSP) when the robot lifts one leg, supporting on the other.

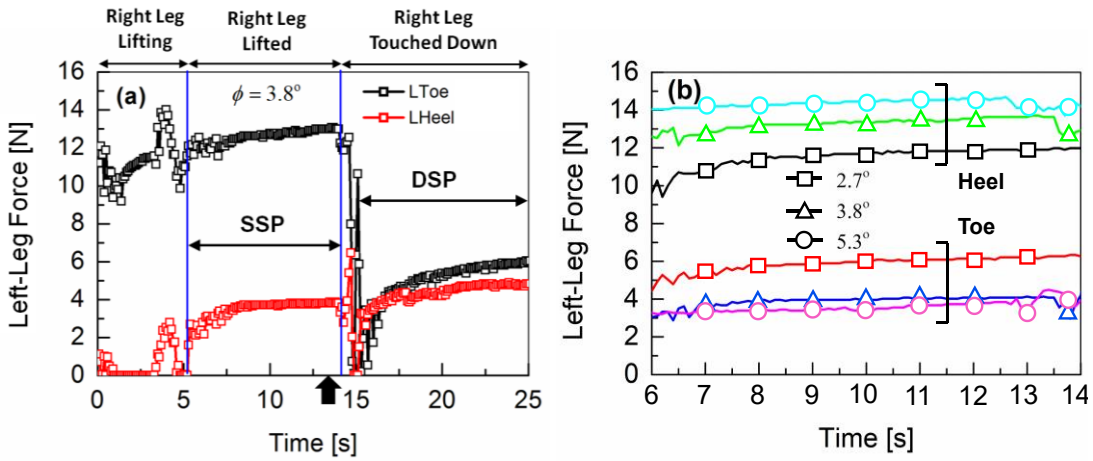

Fig. 3.4. (a)The heel and toe forces acting on the foot of the robot while the robot is standing on an inclined surface of surface inclination 3.8°. (b) The toe and heel forces measured for various surface inclination.

the right leg goes through the process of lifting, then being stably lifted and afterwards touching down again onto the surface of surface inclination of 3.8°. The toe and heel forces on the left foot, are shown in Fig.3.4 (b) for increasing surface inclinations during the SSP, when the right foot is lifted. The cases of different surface-inclinations, 2.7°, 3.8° and 5.3° are identified by the different symbols. With increased surface inclination, the difference

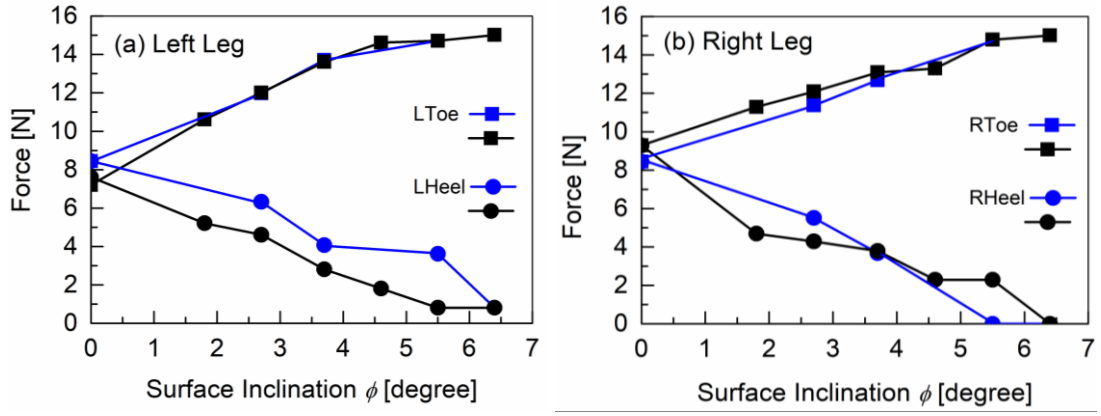

Fig. 3.5. The toe and heel forces of the robot for (a) left and (b) right leg measured at the point indicated with a black arrow in Fig.3.4(a).

between the toe and heel forces increases. Fig. 3.5 shows the measured toe- and heel-forces as a function of surface inclination ϕ (a) for left leg and (b) for right leg. The measurements are taken the time shown by a black arrow in Fig. 3.4(a). It is observed in Fig. 3.5 that the toe force increases while the heel force decreases with increasing ϕ when the robot walks downslope. When the surface inclination reaches to 6.4°, it is observed in the experiments that the robot is balanced only on the toe. This is observed in the measurement when the heel force is becoming zero and toe force is approximately equal to the weight of the robot. It is observed in the experiments, that the robot falls forward when the surface inclinations is increased beyond ϕ = 6.4°.

Beyond the surface inclination of ϕ = 6.4°, the robot-experiments are performed following the 2nd stage. The ankle-pitch motor (M_A) is adjusted by the difference (Δ) between the toe and heel forces of the supporting leg. This prevents the forward falling of the robot by assuring that the full contact of the robot foot with the inclined surface. In Fig. 3.6 the measured force difference Δ is plotted as a function of ϕ for $\phi < 8.5°$.

The measurements verify that the robot-posture can be balanced up to a surface of inclination equal to 7.6° by adjusting only the ankle-pitch motor M_A. Beyond that surface inclination, the robot falls forward again. Therefore, hip-pitch motor M_H is additionally controlled, corresponding to the 3rd measurement stage. The results of the measured force differences are shown in Fig. 3.6. The hip-pitch motor is controlled by the pitch-angular velocity of the robot-torso. With the additional control of the hip-pitch motor the robot can sustain a stable posture up to 9.6° surface inclination.

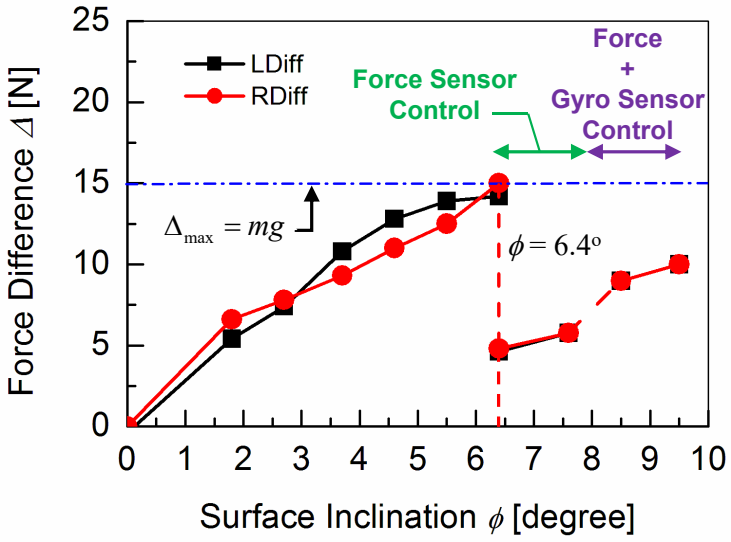

Fig. 3.6. The difference of the toe and heel forces at the robot-foot, as a function of the surface inclination.

3.3 Model Development

The purpose of the modelling is to theoretically explain the measurements obtained from the experiments. The robot motion on the inclined surface with inclination ϕ is modeled by extending the Inverted Pendulum Model (IPM) [56-58]. The IPM incorporates the information of surface inclination and explains the change in the static stability margin of the robot. Based on the IPM, the force sensor based control systems is designed to adjust the ankle-pitch motor adjustment effective robot balancing.

3.3.1 IPM for Robot-Foot-Centric Balancing

The IPM describes the motion of the robot, where the COM of the robot is connected by a link to a fulcrum. The model and model parameters are shown in Fig.3.7(a) [56, 58] and the principal variables and parameters used in the model are listed in Table II. For simplicity, the entire robot mass m is assumed to be concentrated at the point C of the pendulum, which represents the COM of the robot. The connecting links between the fulcrum (point A) and COM of the robot are assumed to be massless. Here a footed IPM is considered. The model assumes a massless foot of length $2b$, measured from the toe (point O) as shown in (see Fig. 3.7(b)). The ankle-pitch motor M_A is the adjusted first following the second stage of the experiments. Thus, the two angles θ_H and θ_K are here set to be

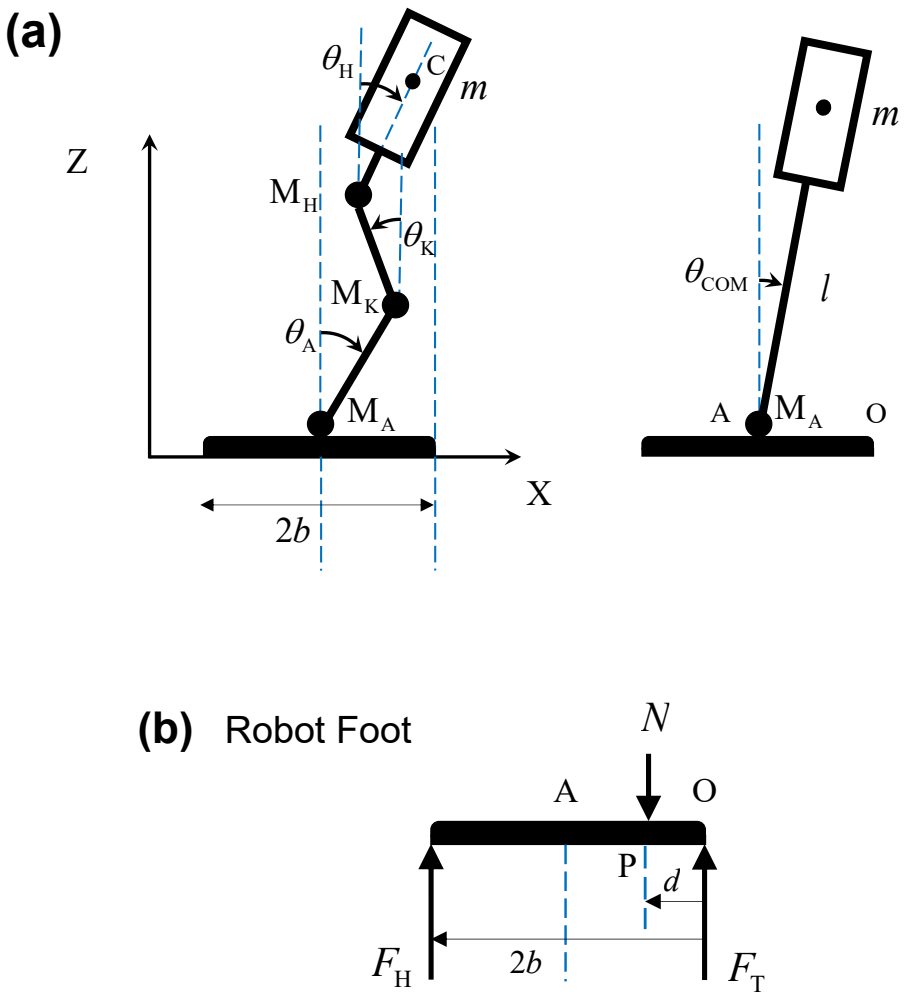

Fig. 3.7. (a) Inverted pendulum model (IPM) and its simplification considering ankle-pitch motor control. (b) Free-body diagram of the robot foot.

constants (reference value), so at first, that the robot's stabilization is studied focusing on controlling the ankle-pitch-motor angle θ_A. Therefore, θ_{COM} is equal to θ_A.

Considering the above assumptions and simplifications, the equation of motion for the IPM can be written as [56]

$$J_A\ddot{\theta}_A = -mgl\sin\theta_A + N\times(b-d) \tag{3.1}$$

where J_A (= ml^2) is the moment of inertia of the pendulum about the point A, and g is the acceleration due to gravity. The first term on the right-hand side of (3.1) describes the rotational torque due to the gravity, and the second term describes the compensating torque induced counter the effect of gravity in order to stabilize the robot posture. From (3.1) it can be seen, that the vertical ground reaction force provides the necessary compensating

Table II. Variables and parameters used in the Inverted Pendulum Model (IPM)

Parameter	**Symbol**	**Unit**
Robot COM link length	l	m
Mass	m	kg
Earth's surface acceleration	g	$m \cdot s^{-2}$
Ankle-pitch motor	M_A	-
Knee motor	M_K	-
Hip-pitch motor	M_H	-
Ankle-pitch-motor angle	θ_A	degree
Knee-motor angle	θ_K	degree
Hip-pitch-motor angle	θ_H	degree
Center-of-Mass-position angle	θ_{COM}	degree
Foot length	$2b$	m

torque for static stability of the robot. The resultant ground reaction force N is acting on the robot foot at point P, called the Zero Moment Point (ZMP) [58], which is assumed to be at a distance of d from the point O, as shown in Fig. 3.7(b). Here a free-body diagram of the robot foot is considered. The two force sensors, attached to the toe and heel of the robot foot measures the vertical forces (shown by upward arrow) acting on the robot foot. This is shown in Fig. 3.7(b). The forces denoted by F_H and F_T are respective vertical reaction forces acting on heel and toe of the robot foot. It is observed in Fig. 3.7(b that the vertical forces N and F_H generates moments around the point O. Under equilibrium, the net moment about the point O should be equal to zero and the torque-balance equation is given by

$$F_H \times 2b = N \times d \tag{3.2}$$

Therefore, the vertical forces acting on the toe and heel can be expressed in terms of the resultant vertical ground reaction force.

$$F_T = N \times \left(\frac{2b-d}{2b} \right); \quad F_H = N \times \left(\frac{d}{2b} \right) \tag{3.3}$$

where $F_T + F_H = N$. The force-difference Δ is defined as the difference between toe and heel reaction forces,

$$\Delta = F_T - F_H = N \times \left(\frac{b-d}{b} \right) \tag{3.4}$$

Now substituting (3.4) into (3.1), the equation of motion can be rewritten as,

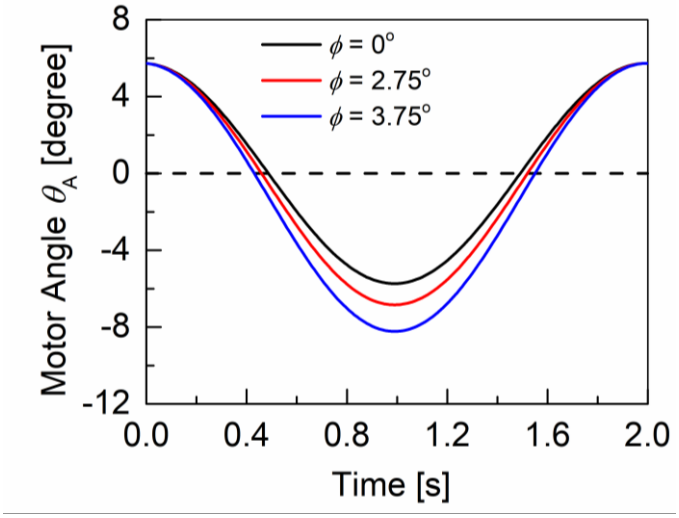

Fig. 3.8. The shift of the oscillation of the motor angle θ_A around θ_A=0 for $\phi > 0$. The asymmetrical nature of the angle is caused by the surface inclination.

$$J_A \ddot{\theta}_A = -mgl \sin\theta_A + (\Delta \times b) \tag{3.5}$$

Therefore, the equation of motion is now expressed in terms of the measured sensor data $\Delta = F_T - F_H$. Equation (3.5) confirms, that an increase in the force difference Δ indicates that a higher compensating motor-torque is required to adjust the robot posture.

3.3.2 Extension of IPM for Inclined Surface

Based on the results of the robot-balancing measurements shown in Fig. 3.6, modeling of the inverted pendulum is extended to incorporate the surface inclination ϕ. In that case the equation of motion (3.5) can be written as

$$J_A \ddot{\theta}_A = -mgl \sin(\theta_A + \phi) + \Delta \times b \tag{3.6}$$

where the first term of the right-hand side contains the surface inclination ϕ. Fig. 3.8 shows numerical solution for θ_A of (3.6) for different surface inclinations. As expected the solution of (3.6) is a sinusoidal waveform which means that the motor angle θ_A oscillates symmetrically around θ_A=0° for ϕ=0°. However, when the surface inclination is increased the oscillation about the horizontal axis becomes asymmetrical. The target of the control is to make the waveform symmetrical by adjusting the motor angle.

The robot maintains its equilibrium when the surface inclination is below ϕ_{cr}. In that caaes it can be assumed that the resultant torque at motor M_A is equal to zero. Therefore,

the force difference Δ under static stability equilibrium can be derived from (3.6) as

$$\Delta = \frac{mgl\sin(\theta_A + \phi)}{b} \tag{3.7}$$

(3.7) gives the force difference Δ as a function of the surface inclination ϕ and the ankle-pitch motor's angle θ_A. The maximum theoretical value of Δ is equal to the weight of the robot (=mg). θ_{A0} is the initial value of θ_A which can be calculated from (3.7) by assuming $\phi = 0^o$ and using the measured value for the force difference Δ on a flat surface.

The critical inclination ϕ_{cr} is measured to be equal to 6.4°. The angle ϕ_{cr} can be theoretically calculated by setting Δ equal to weight of the robot.

$$\Delta_{max,theo} = \frac{mgl\sin(\theta_{A0} + \phi_{cr,theo})}{b} \tag{3.8}$$

Substituting $\Delta_{max,theo} = mg$ and $\theta_{A0} = 0^o$, it can be seen, that $\phi_{cr,theo}$ is solely determined by only the robot structure as

$$\phi_{cr,theo} = \sin^{-1}\left(\frac{b}{l}\right) \tag{3.9}$$

Considering the potential energy of the inverted pendulum [57] and minimizing the potential energy leads to $\phi_{cr,theo} = \tan^{-1}(b/l)$, which is reduced to (3.9) in this practical case of $(b/l) << 1$. (3.9) is extended to incorporate the initial θ_{A0}, leading to

$$\phi_{cr,theo} = \sin^{-1}\left(\frac{b - l\sin\theta_{A0}}{l\cos\theta_{A0}}\right) \tag{3.10}$$

Equation (3.10) describes, that the $\phi_{cr,theo}$ is modified by θ_{A0}, as shown in Fig. 3.9. $\phi_{cr,theo}$ can be calculated with (3.10) for the initial condition θ_{A0}. In this analysis θ_{A0} and $\phi_{cr,theo}$ are determined to be equal to 0.05° and 5.7°, respectively. The theoretically calculated force-difference Δ calculated form (3.7) are compared with the measured results in Fig. 3.10. It is observed that measured Δ is not a linear function of ϕ, but has a weak saturating feature. Also, the measured critical surface inclination $\phi_{cr,exp}$ is equal to 6.4°, while the theoretical prediction gives $\phi_{cr,theo}$=5.7°. The reason for this is attributed to the friction effect between the robot feet and the ground surface. The surface friction can be modelled by the equivalent circuit method [87-88]. In this presented theoretical investigation, the contribution of the

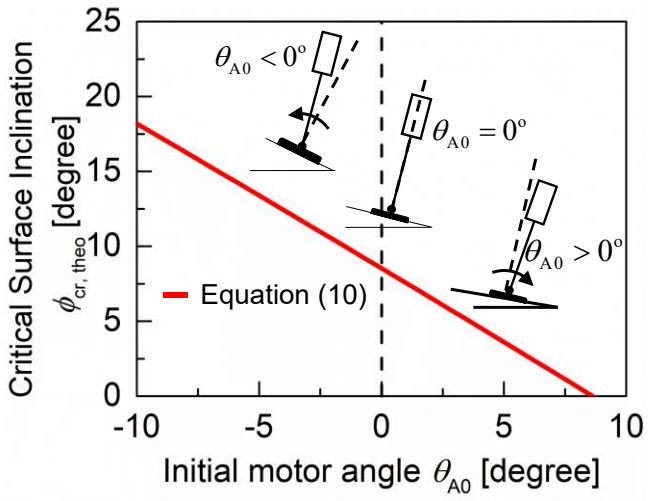

Fig. 3.9. Initial ankle-pitch motor angle of the robot determines the static stability margin of the robot according to the (3.10).

surface friction is neglected for robot balancing on inclined surface, and the measurements are performed surfaces with less friction.

3.3.3 Ankle-Torque Compensation

The compensating torque of the motor is expressed as a function of the force-difference Δ in the equation of motion of the inverted pendulum (see (3.6)).In these experiments, the adjustment of the angle θ_A is started beyond $\phi = \phi_{cr,exp}$. The equation of robot motion (3.6) on an inclined surface is rewritten by expressing the compensating torque as a function the reference angle θ_A^* (see also [56])

$$J_A\ddot{\theta}_A = -mgl\sin(\theta_A + \phi) + K_P(\theta_A^* - \theta_A) + K_I\int(\theta_A^* - \theta_A)dt + K_D\frac{d}{dt}(\theta_A^* - \theta_A) \quad (3.11)$$

$$= -mgl\sin(\theta_A + \phi) + u(t) \quad (3.12)$$

The gains K_P, K_I and K_D in (3.11) are experimentally extracted from the motor-armature voltage as a function of the difference between feedback-potentiometer voltage (the measured motor angle θ_A) and reference-voltage value (the reference angle θ_A^*). The difference between the voltages corresponding to θ_A^* and θ_A represents an error voltage e. This error voltage is used to control the armature voltage V_{arm} of the DC motor to generate the necessary torque. The internal circuitry of the servomotor control system is shown in Fig.3.11(a). The armature voltage V_{arm} is plotted as a function of the error voltage e for

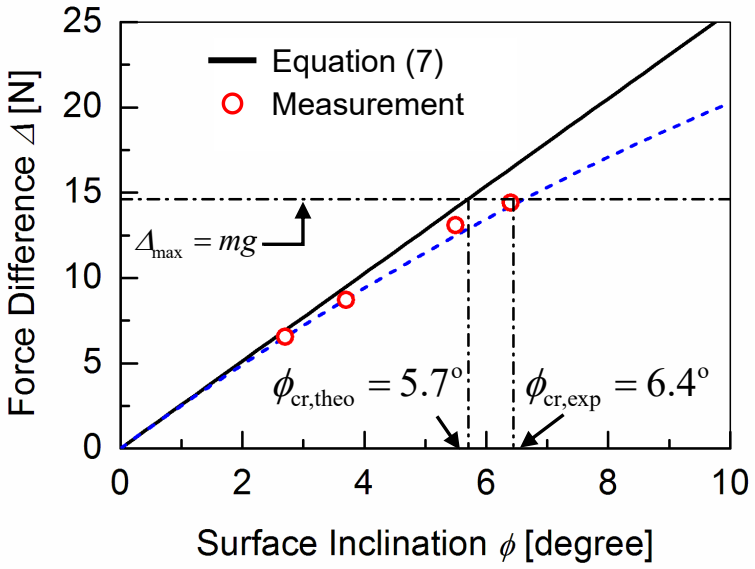

Fig. 3.10. Comparison of simulated (with low friction) and experimentally measured (with friction) force differences for both left and right leg of the robot.

three different reference angles θ_A^* (namely, -84.3°, 0° and +84.3°). The relation between e and V_{arm} is used to determine the PID control function $u(t)$ (see (3.12)). Fig. 3.11(b) shows the procedure to determine the gains K_P, K_I and K_D by fitting the experimental data of armature voltage as a function of error voltage. The experimentally determined values of the gains K_P, K_I and K_D are 69, 40 and 2, respectively, which are also listed in Fig. 3.11(b).

The motor angle θ_A is rotated to θ_A^* in to stabilize the robot posture by minimizing the Δ below Δ_{max}. The numerical solutions of (3.11) for different ϕ conditions are shown in Fig. 3.12(a). With increasing ϕ, these overshoots of θ_A become larger. This makes the robot posture increasingly unstable during the motor-adjustment. There is increased oscillation observed when the adjustment starts. Fig. 3.12(b) shows calculated pitch-angular velocities ω ($=d\theta_{COM}/dt$) of the robot-torso, when the motor adjustment is done. For $\phi = 7.6°$ only θ_A is adjusted. But at higher surface inclination, an additional θ_H-rotation is done for $\phi = 9.5°$. It is seen that the extended-IPM can predict the adjustment of the robot-body quite accurately, especially for the single-motor control for surface inclination $\phi = 7.6°$. The deviation for $\phi = 9.5°$ is mostly due to the additional θ_H control. The prediction, that a larger ϕ induces a larger overshoot in the angular-pitch robot-torso velocity ω, is confirmed by the measurements as well.

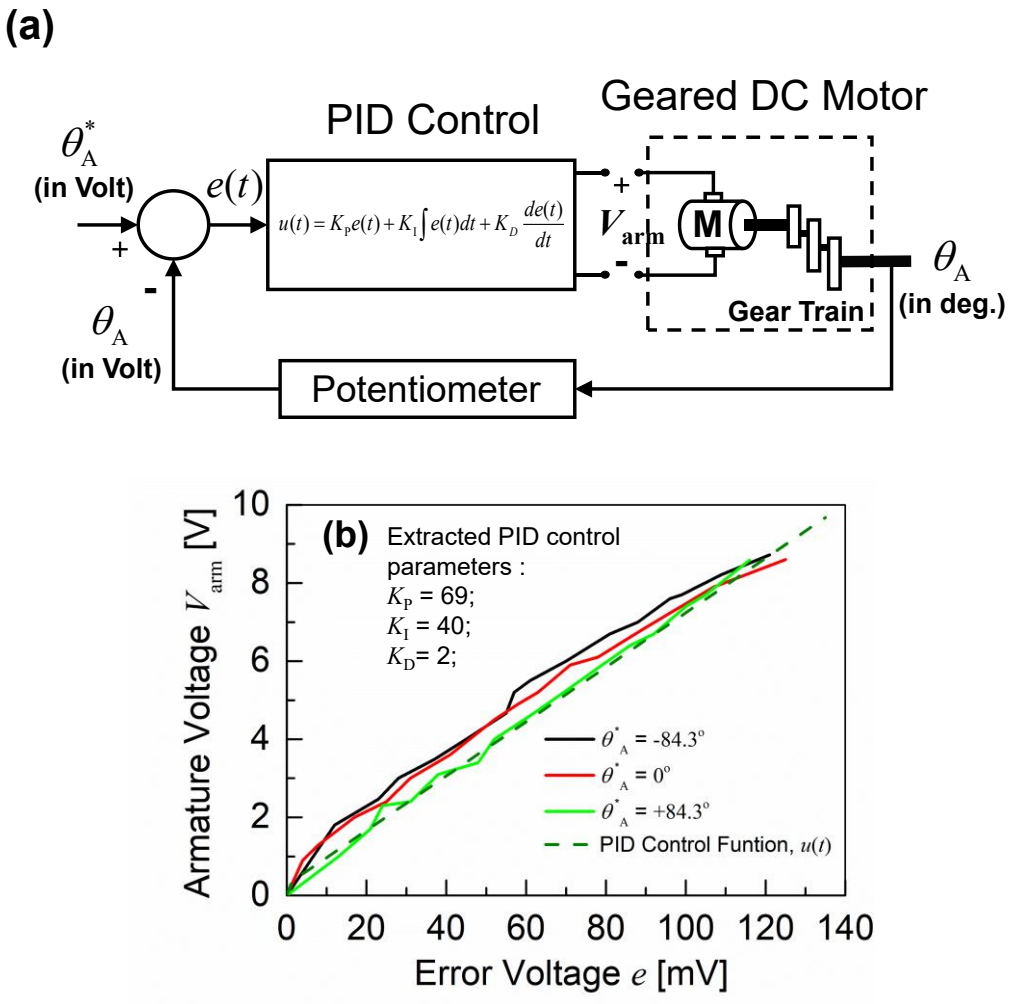

Fig. 3.11. (a) The PID control system implemented in the servomotor controller of the robot. (b) Measured results of armature voltage V_{arm} as a function of error voltage e for different reference angles θ_A^*.

The calculated and the measured maximum ω-overshoot are compared in Fig. 3.13. A drastic increase of ω is observed for $\phi > 7.6^o$, indicating the requirement of higher torque compensation at higher surface inclination. The sudden increase in overshoot also implies that posture control solely based on the force sensors under the robot feet is not sufficient to make the robot posture stable. This leads to the second stage of the experiments, where the angular velocity is used to control the robot posture beyond surface inclination of 7.6°.

3.4 Analysis of Measured Control Features

In Fig. 3.6, the measured Δ is plotted as a function of the surface inclination angle ϕ. The robot-posture control is done by implementing feedback control systems based on use

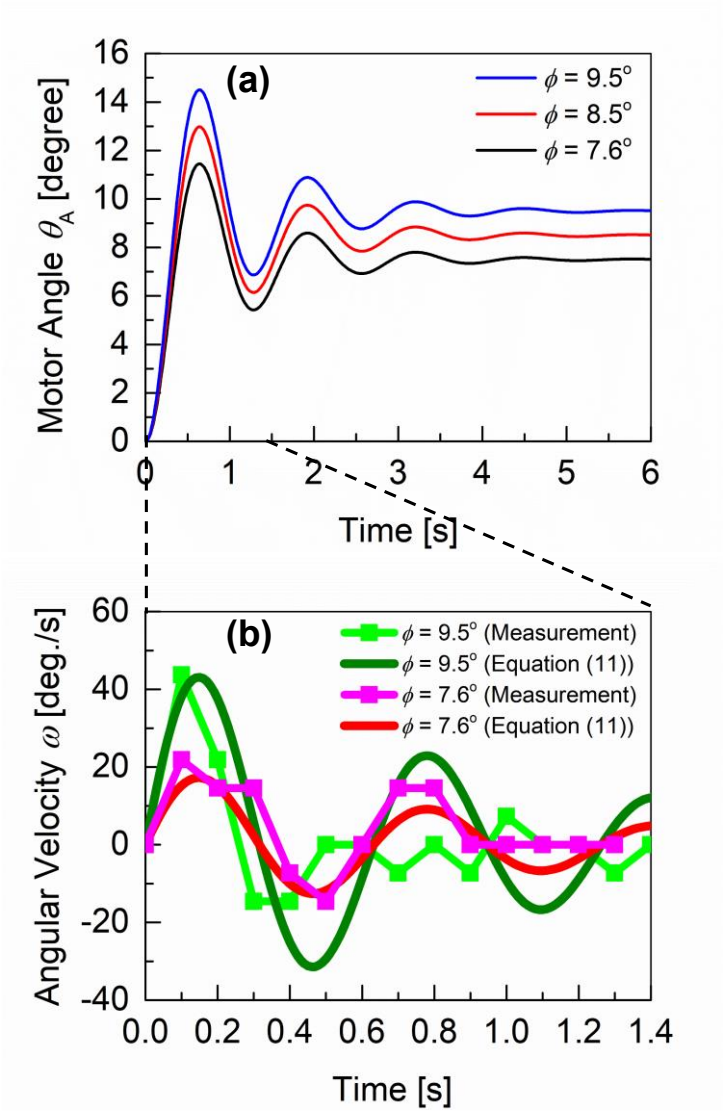

Fig. 3.12. (a) The adjustment of the ankle-pitch-motor angle θ_A according to (3.11), for different surface inclination (b) Simulation result for the torso-angular velocity ω of the robot in comparison to the gyro-sensor measurements.

measured data for Δ and ω of motion into the robot system, for surface inclinations $\phi \geq \phi_{cr,exp}$. The implementation is done as shown in Fig. 3.14. Two online streams of measured data are fed back independently. In the electrical feedback controlling of the robot, the θ_A* (and also θ_H*) are controlled by the measured data (Δ and ω) in the form

$$\theta_A^* = \theta_{A,0} + K_A \Delta \tag{3.13}$$

$$\theta_H^* = \theta_{H,0} + K_H(\omega_{ref} - \omega_{meas}) \tag{3.14}$$

where ω_{meas} and ω_{ref} are measured and reference value of the angular-pitch velocity, respectively. The reference value ω_{ref} for the angular-pitch velocity is equal to 0 deg/s. K_A

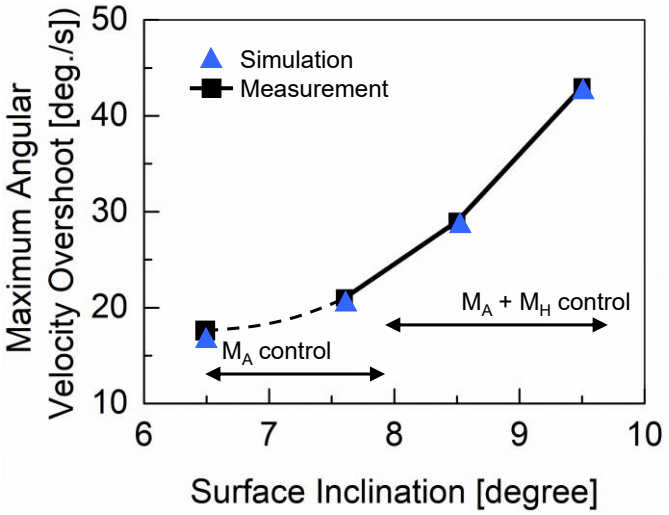

Fig. 3.13. The maximum overshoot of the torso-angular velocity of the robot increases abruptly beyond surface inclination 7.6°. This indicates the requirement of the hip-pitch motor-control at higher surface inclination.

and K_H are adjustable gain between the motor and its load. For higher compensating torque, needed to stabilize the robot-posture, higher K_A and K_H values are required.

The K_A value is set to 12, so that the most stable condition for ϕ =6.4° are realized. Based on the θ_A control, the Δ is reduced allowing the robot to keep a stable posture up to 7.6° surface inclination. According to Fig. 3.9 the θ_A rotation (i.e., the setting of a new θ_{A0}), should change the critical surface inclination ϕ_{cr}. However, it is found experimentally, that the robot falls down at much smaller surface inclinations ϕ than the expected $\phi_{cr,theo}$. Figure 3.15 adds the extension of the force difference at higher surface inclination when the ankle-pitch motor is controlled with increased K_A. With the increase in the surface inclination, a higher K_A value is required to increase the compensating-torque at the ankle-pitch motor of the robot for postural stabilization. But higher K_A causes instabilities due to increased vibration. Consequently, based on the trade-off between a sufficient torque to control the robot motors and vibration of the robot, K_A is optimized and implemented in the control system. As observed in the experiment, the robot can maintain a stable posture up to surface inclination of ϕ=8.88°, as plotted in Fig. 3.15 for K_A=14. Therefore, the control of ankle-pitch motor according to the ϕ increase is a viable solution to achieve a stable robot posture up to a certain surface inclination. To further increase the robot stability, the hip-pitch motor is to be controlled based on the angular-pitch velocity. With this sequential approach

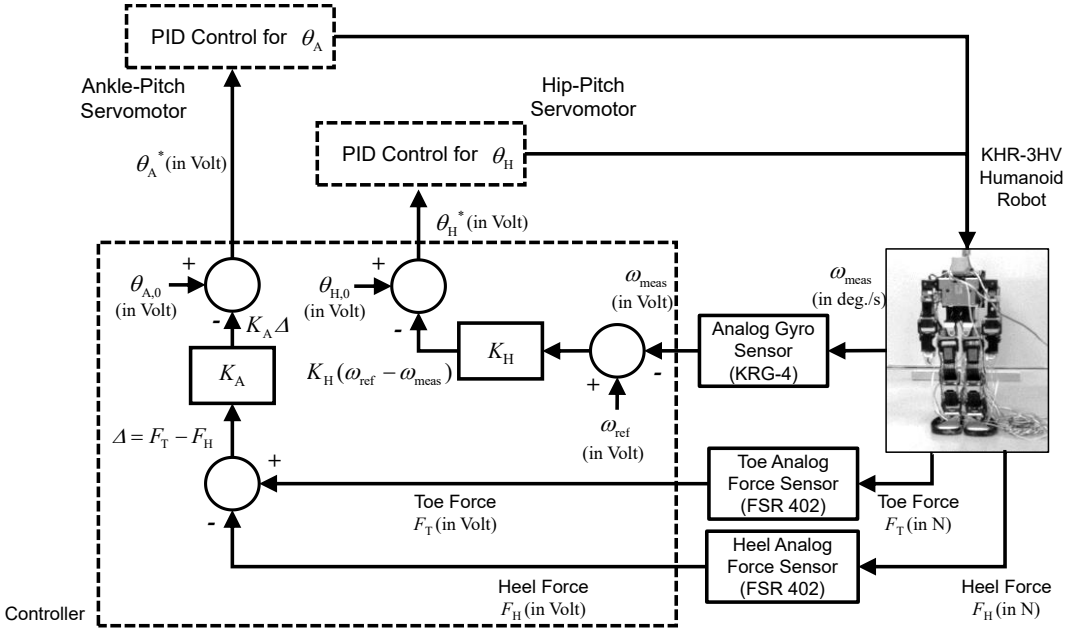

Fig. 3.15. The block diagram of the implemented control system for the ankle-pitch-motor angle θ_A and the hip-pitch-motor angle θ_H.

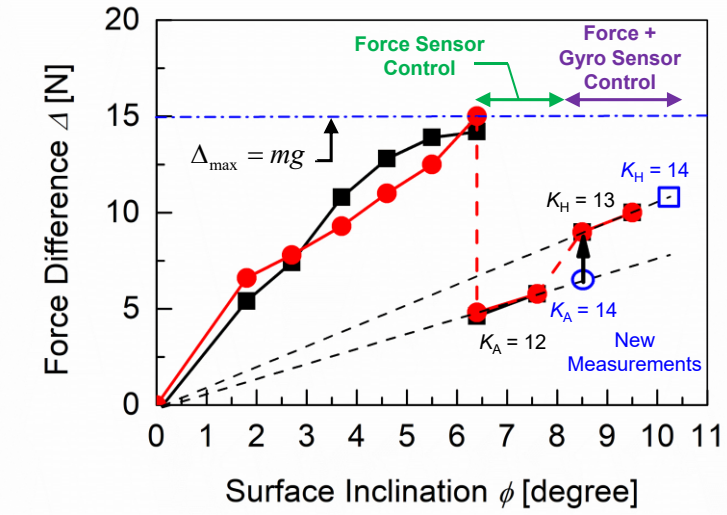

Fig. 3.14. At higher surface inclination, the robot-stability is improved due to feedback motor control and the adjustment of feedback-control parameters (see (3.13) and (3.14)).

to control, it is found that robot can maintain its stable posture up to 10.2° of surface inclination.

3.5 Conclusion

The focus has been given on the maintenance of static stability of the light-weight humanoid robot on inclined surfaces. The investigation starts with the experimental

observation of the robot posture stability on inclined surface followed by theoretical investigation to explain the experimental measurements. The surface-inclination ϕ is shown to be determinable from the difference Δ calculated form the measured toe and heel forces of each robot foot. The experimental observations and measurements reveal that the robot requires no feedback control up to a certain critical surface inclination ϕ_{cr}. Beyond ϕ_{cr} the robot falls forward on the downslope.

For surface inclinations beyond ϕ_{cr}, a force-sensor based feedback control of the ankle-pitch motor is introduced to sustain the surface connection of the robot feet. This reduces the force difference Δ between toe and heel of the robot feet, allowing the robot to keep a stable posture. When the surface inclination is increased further, however, the ankle-pitch-motor control alone is no longer sufficient to maintain the stable robot posture. Therefore, a gyro-sensor-based hip-motor adjustment is additionally introduced in order to control the robot posture.

In the theoretical investigation, the Inverted Pendulum Model (IPM) is extended to include the surface-inclination in order to explain the static stability margin of the robot standing on an inclined surface. This extended IPM can also accurately reproduce gyro-sensor-measured angular-pitch velocities during feedback control on inclined surfaces..

Generally, the Zero Moment Point (ZMP) is used to characterize robot instabilities on inclined surfaces. However, the developed method for using the measured force differences Δ between toe and heel forces is an alternative way to measure the robot-instability. The measurement provides a simpler and yet accurate approach.

Chapter 4: Gyro Sensor Based Postural Stabiity Control

4.1 Introduction

The chapter proposes a circuit level implementation of an electro-mechanical model of a single axis gyro sensor. The electro-mechanical model is developed in order to analyze the circuit level behavior of the sensor. The purpose of this analysis is to incorporate circuit behavior of the sensor into the robot-system simulation toolbox. This will enable to analyze the circuit effect of a particular sensor component on the dynamics of the robot. Generally speaking, this is an attempt to bridge the dynamic-response of a macroscopic system for a given microscopic response of a system integrated within it.

In the latter half of this chapter, an attempt is made to incorporate the circuit level model of the sensor to model a gyro-sensor based feedback control system in order to simulate the dynamic response of the robot to an external disturbance push-force. This work shows how circuit behavior of the gyro senor is incorporated to simulate the robot dynamics. The chapter is arranged in the following way.

In Section 4.2, the working principle of a vibratory gyro sensor is discussed followed by the circuit description of the gyro sensors in sections 4.2.2. The simulation results carried out with a SPICE circuit simulator [87-88] is discussed in section 4.2.3. Section 4.2.4 discusses the design and simulation results of an envelope detector used in the gyro sensor model. In section 4.2.5 the dynamic characteristics of the developed gyro sensor model are experimentally verified with the analog gyro sensor KRG-4 [99]. The section 4.3 discusses dynamics of robot when it is applied with an external push force. A gyro sensor based feedback control system is proposed in section 4.3.2 to stabilize the robot posture. The response of the robot dynamics is analyzed incorporating the electromechanical response of the developed gyro sensor and the control system was experimentally verified in Section 4.3.3. The robot with its push-force disturbance rejection system was exhibited in public robot competition ROBO-ONE at Kobe, Japan. The outcomes of the competition are briefly reported in section 4.4. Section 4.5 concludes the chapter.

4.2 Electromechanical Modelling

The single-axis vibratory gyro sensor is a micro-electro-mechanical system (MEMS). The electro-mechanical model is implemented in Verilog-AMS and simulated using an

$$\vec{F}_{\text{cor}} = 2m(\vec{v} \times \vec{\omega})$$

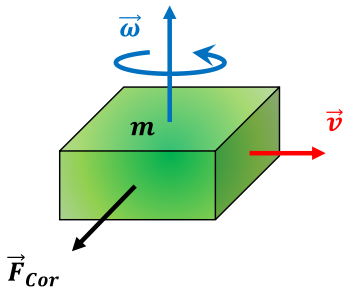

Fig. 4.1. The vibratory gyro-sensor is based on the Coriolis Effect.

SPICE circuit simulator to analyse the time-domain responses and frequency domain characteristics of the sensor circuits.

The vibratory gyro sensor is based on the principle of the Coriolis Effect. According to the Coriolis Effect, when a linearly moving (with velocity v) mass m is rotated with an angular-pitch velocity ω, the mass experiences a force proportional to the product of v and ω, in the direction perpendicular to both v and ω. The effect is shown in Fig. 4.1.

4.2.1 Gyro Sensor

Based on the principle of Coriolis Effect, the gyro sensor is developed. The vibratory single-axis gyros sensor has two circuits: driving circuit and sensing circuit [18]. From the principle of Coriolis Effect, it is seen that a mechanism is needed to drive the microscopic mass. For that purpose a driving circuit is used. When the mass detects an external angular velocity, the mass experiences a Coriolis force. For sensing this Coriolis force the sensing circuit is used. In the next section, the circuit are discussed in details.

4.2.2 Circuits of Gyro Sensor and Modelling

The driving and the sensing circuits of a single axis vibratory gyro sensor are shown in the Fig. 4.2(a) and 4.2(b). The driving circuit moves the central mass to oscillation. This is called the driving mode. The movable mass m is subjected to the driving mode by a sinusoidal force $F_1 = F_0 \cos 2\pi ft$. In the used gyro-sensor system, the mass is driven by the electrostatic force inside the combed finger structure, which is induced by the sinusoidal input voltage V_{in} of the driving circuit as shown in Fig. 4.2(a). The MEMS push-pull driver is shown to have this comb-like structure in Fig. 4.2(a). The lateral driving induces a linear velocity v.

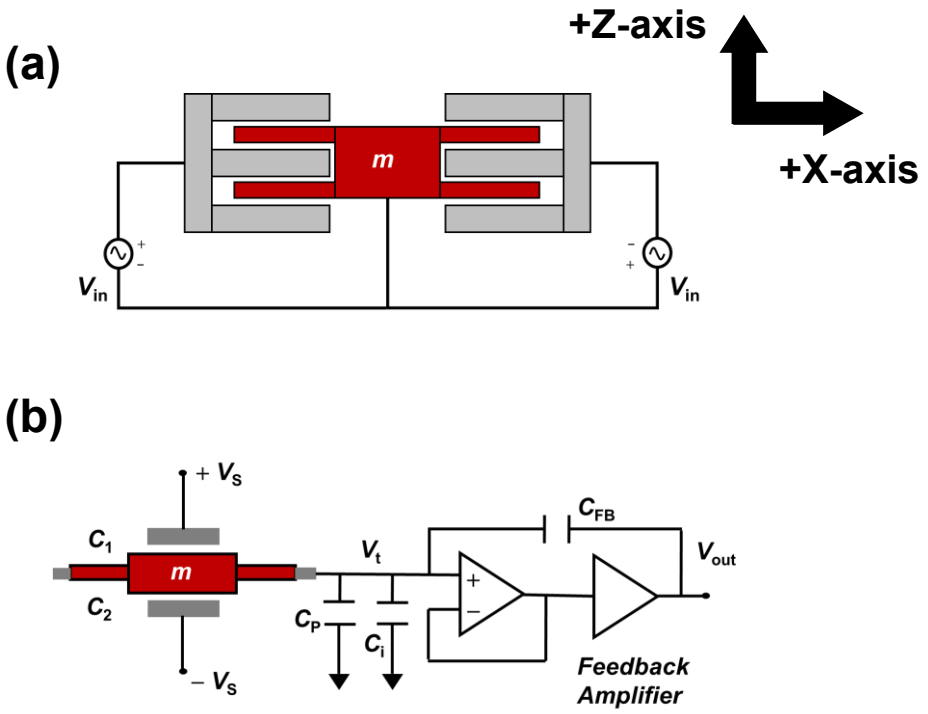

Fig. 4.2. (a) Driving Circuit of the vibratory MEMS gyro sensor. (b) Sensing circuit of the gyro sensor.

The modelling of this driving mechanism can be done by considering a mass suspended by spring-damper system as shown in electromechanical methodology in Fig. 4.3. The coordinate system used to represent the dynamics of the central mass is shown in Fig. 4.2. The mass is driven along X-axis, which is the driving axis. The generated electrostatic force F_1 (see step 1 and 2 of Fig. 4.3) drives the central mass with the driving velocity v. The second-order differential equation is solved to calculate the driving velocity v, describing the dynamics of the mass suspended by a spring and a damper (see step 2 of Fig. 4.3).

When the system is rotated around the +Y-axis (normal to the paper plane) with an angular velocity ω, a force F_{Cor} is induced on the moving mass along the +Z axis because of the Coriolis Effect. This force causes the central mass to oscillate also along Z-axis, which initializes the sensing mode of the gyro sensor. In the model, the Coriolis force is calculated as shown in step 4 of Fig. 4.3. The sensing circuit is used to sense the vertical displacement of the central mass due to movement in +Z direction. This is done by producing an equivalent electric signal which is proportional to the angular velocity applied to the central mass. The sensing circuit, shown in the Fig. 4.2(b), is based on the differential capacitive sensing. Initially, when the mass is being driven only along X-axis, the

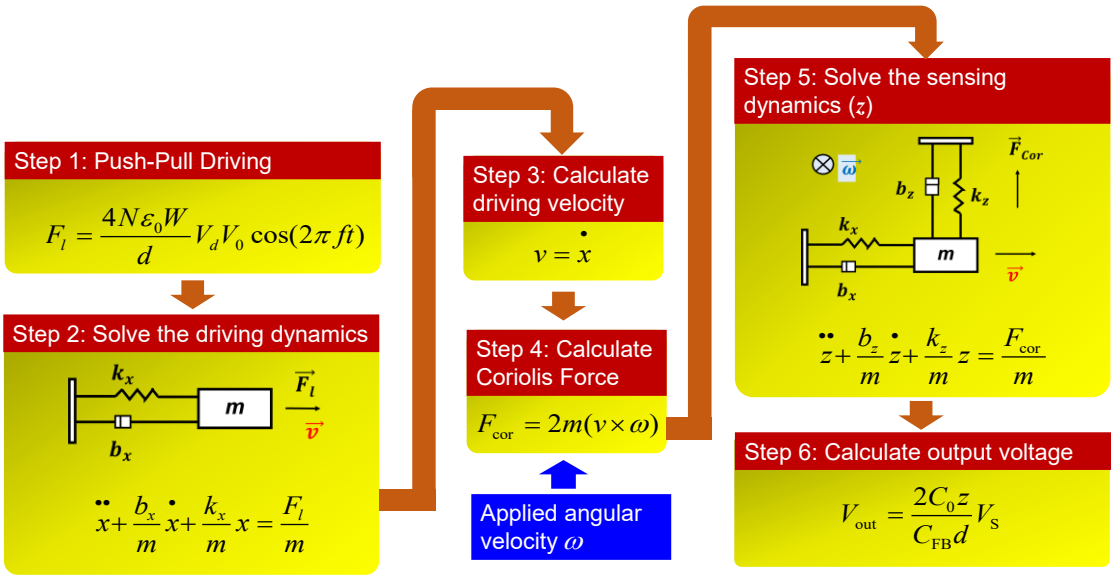

Fig. 4.3. The methodology of the electromechanical modeling of the driving and sensing circuits of the vibratory single axis gyro sensor.

capacitances C_1 and C_2 are equal. But when the mass oscillates along Z-axis due to the Coriolis force, C_1 and C_2 start to differ from each other. The difference between the two capacitances C_1 and C_2 is measured by the sensing circuit, which is converted into an equivalent electric voltage V_{out}. The difference in the capacitances is a function of the vertical displacement of the central mass. This displacement is calculated by solving the second-order differential equation as shown in step 5 of Fig. 4.3. The voltage is proportional to the vertical displacement (see step 6 of Fig. 4.3) and indirectly proportional to the input angular velocity ω and the Coriolis force F_{Cor}. The physical parameters of the gyro sensor model are given in Table III.

4.2.3 Simulation Results

Simulation results obtained using circuit simulator [87-88] with the developed equivalent circuit of the gyro sensor are shown in Figs. 4.4. V_{in} is the input voltage to the driving circuit (See Fig. 4.2(a)), which drives the central mass of the system. Fig. 4.4 shows the simulation result, where a sinusoidal angular velocity is considered. It is clearly observed that the envelope of V_{out} contains the information of the applied angular velocity. The input voltage V_{in} is amplitude modulated by the input angular velocity to give the output voltage V_{out}.

Table III. Gyro Sensor Model Parameters

Parameter	**Symbol**	**Unit**	**Value**
Sensor seismic mass	m	Kg	1.678×10^{-11}
Driving circuit damping coefficient	b_x	$N\cdot s\cdot m^{-1}$	8.5×10^{-7}
Driving circuit stiffness coefficient	k_x	$N\cdot m^{-1}$	0.07
Total number of fingers	N		160
Permittivity of space	ε_0	$m^{-3}\cdot Kg^{-1}\cdot s^{-4}\cdot A^2$	8.854×10^{-12}
Width of the comb finger	W	m	40×10^{-6}
Finger spacing	d	m	3×10^{-6}
Sensing circuit damping coefficient	b_z	$N\cdot s\cdot m^{-1}$	0.5×10^{-7}
Sensing circuit stiffness coefficient	k_z	$N\cdot m^{-1}$	0.2
Intrinsic capacitance between fingers	C_0	Farad	3×10^{-12}
Feedback capacitance of sensing circuit	C_{FB}	Farad	4×10^{-12}

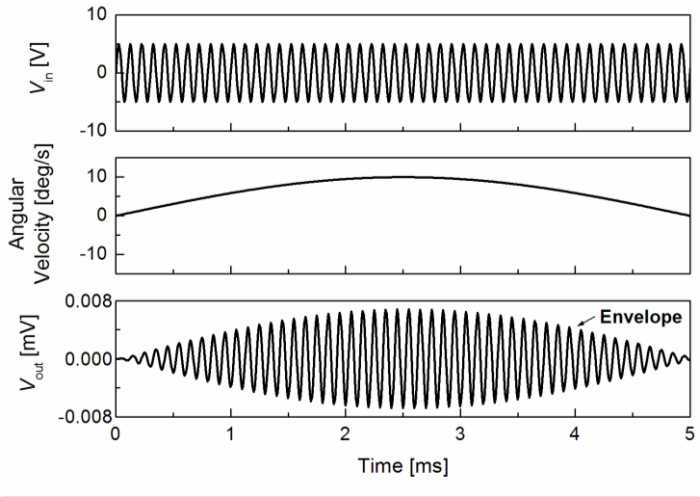

Fig. 4.4. The simulation result of the output of the gyro sensor model. The input voltage to the driving circuit V_{in} is amplitude modulated by the input angular velocity to give the output voltage V_{out}.

Therefore sensing circuit gives rise to an amplitude modulated waveform. The parameters used for the simulations are described in Table III. All the parameters except damping and stiffness coefficients are fixed initially to predict the dynamic behavior of gyro sensor. Then the stiffness and damping coefficients are adjusted very precisely to describe the mechanical model. As the model is based on the underlying physics the minute adjustments of the model parameters are sufficient to predict the experiment accurately.

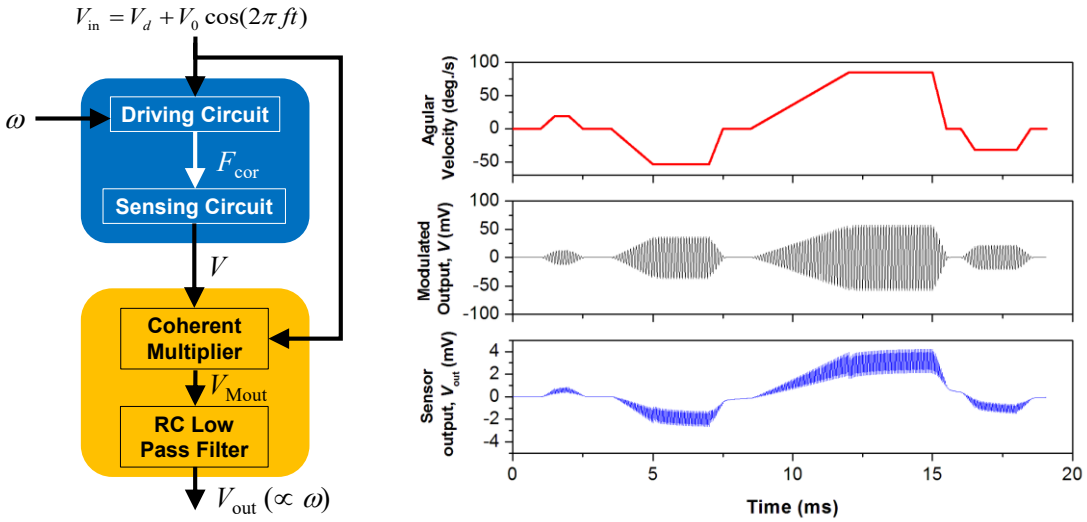

Fig. 4.5. A demodulator is designed based on the principle of the envelope detector. The envelope detector detects the envelope of the sensing circuit output *V*.

4.2.4 Envelope Detector

It is discussed in the previous section that the output of the sensing circuit contains the information of the angular velocity. For that an envelope detector (demodulator) is designed and integrated to the gyro sensor model. This is shown schematically in Fig. 4.5. The detector demodulates the output of the sensing circuit and produces the waveform of the applied angular velocity, shown also in Fig. 4.5. The RC low pass filter characteristics determine the accuracy of the output of the detector. The RC filter is designed based on the Nyquiest frequency of the output of the coherent multiplier.

4.2.5 Experimental Verification

In order to verify the developed electromechanical model, the static characteristics of the developed model is verified experimentally with an analog gyro sensor KRG-4 [99]. The results are shown in Fig. 4.6. The model parameters are adjusted so that the model values fit to the experimental values of output voltage for a given angular velocity applied to KRG-4. The figure shows that the modeled results predict the measurement nearly perfectly.

This concludes the development and experimental verification of an electro-mechanical model of a single-axis analog vibratory gyro sensor. Now, this model will integrated to

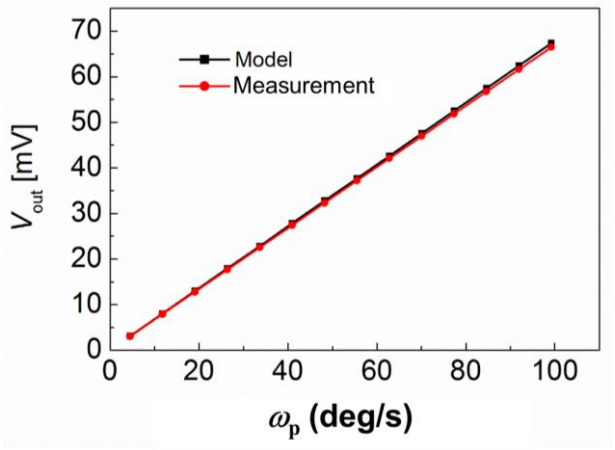

Fig. 4.6. Experimental verification of the developed electro-mechanical model of the single-axis vibratory gyro sensor.

control system for the robot in order to simulate the dynamics of the robot, when applied with an external push force.

4.3 Push-force Disturbance Rejection

4.3.1 Falling Dynamics

When an external push force is applied to a robot, the dynamics of the humanoid can be modelled with a constant-length inverted pendulum as shown in Fig. 4.7(a). Here a simple inverted pendulum with three degrees of freedom is considered denoted by ankle-pitch motor M_A, knee motor M_K and hip-pitch motor M_H. The links of motors are assumed to be massless and the total mass m is considered to be concentrated at center of mass (COM) of a bob. Initially, the hip, knee and ankle-motor angles are set to zero when the robot is standing on a flat surface. The distance of the robot COM from point A is equal to l i.e. the sum of the lengths of three links connecting the motors. The pendulum is assumed to have a massless feet of length b. When a constant force F is applied to the robot, the robot body rotates around the toe of the feet denoted by point O in Fig. 4.7(b). This is a situation of under-actuation [30] for the humanoid robot. Here, when a constant force F is applied to the robot, the COM of the robot follows a trajectory of an inverted pendulum with constant length L_0. Such a motion of the robot COM can be modelled with an inverted pendulum of constant length L_0, which can be written as

$$L_0 = \sqrt{l^2 + b^2} \tag{4.1}$$

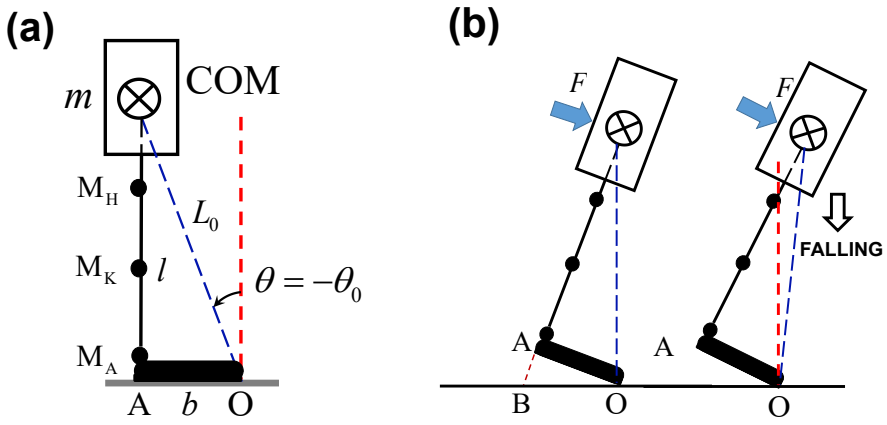

Fig. 4.7. An inverted pendulum model is used to model the robot dynamics when it is applied with an external push-force.

Initially when the robot is not exerted with the push-force, the inverted pendulum is stable at an angle of $\theta = \theta_0$. The initial angle can be geometrically derived from the configuration of the pendulum.

$$\theta = -\theta_0 = -\tan^{-1}\left(\frac{b}{l}\right) \tag{4.2}$$

From the potential energy calculation of the pendulum [57] it can be shown that the robot does not fall forward as long as the angle of the inverted pendulum rotates within the range of

$$-\theta_0 \le \theta \le 0 \tag{4.3}$$

It can be seen from (4.2) and (4.3) that this boundary condition for static stability is a function of robot-height and robot-foot length. This boundary is shown in Fig. 4.7(a) by a vertical dotted red line. The equation of motion of the inverted pendulum is given by

$$mL_0^2 \frac{d^2\theta}{dt^2} = mgL_0 \sin\theta + FL_0 \cos\theta \tag{4.4}$$

where m is the mass of the robot and g is the acceleration due to gravity. The force F is applied to the robot until it starts to fall down (see Fig. 4.7(b)). The angular velocity of the inverted pendulum undergoing the negative-pitch motion is calculated from the first-order derivative of the solution to (4.4). The calculation results of the angular velocity as a

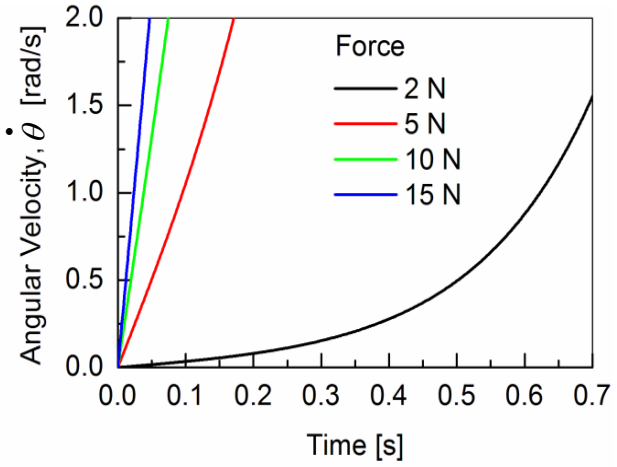

Fig. 4.8. Experimental verification of the developed electro-mechanical model of the single-axis vibratory gyro sensor.

function of time for increasing magnitude of the constant push-force F, are shown in Fig.4.8.

The transient response of angular velocity as shown in Fig. 4.8 highlights two important aspects of the control mechanism for stabilizing the robot-posture i.e. to oppose the disturbance caused by the push-force. First, higher magnitude of applied force requires higher magnitude of compensating force in order to stabilize the posture of the robot. This is indicated by the slope of the transient response. Second, the response time plays a crucial role in case of stabilizing the robot-posture. Higher force requires faster response from the robot to stabilize its posture. The response time of the control system largely depends on the internal circuit of the feedback control system.

4.3.2 Control System

The implemented control system is shown in Fig. 4.9. In this work, only the ankle-pitch motor angle is controlled by the pitch-angular velocity measured by the gyro sensor. For simulating the robot-dynamics based on the (4.4), the electromechanical model of the gyro sensor is integrated to the conventional control system for geared DC servomotor. The change in the angular-pitch velocity of the robot COM is measured by the gyro. The measured angular-pitch velocity is compared with the reference angular-pitch velocity of the robot torso. The difference between the reference and measured angular-pitch velocity is used to control the ankle-pitch motor angle as shown in Fig. 4.9. Now the ankle-pitch motor rotates changing the motor-angle from reference to a new value. This will change

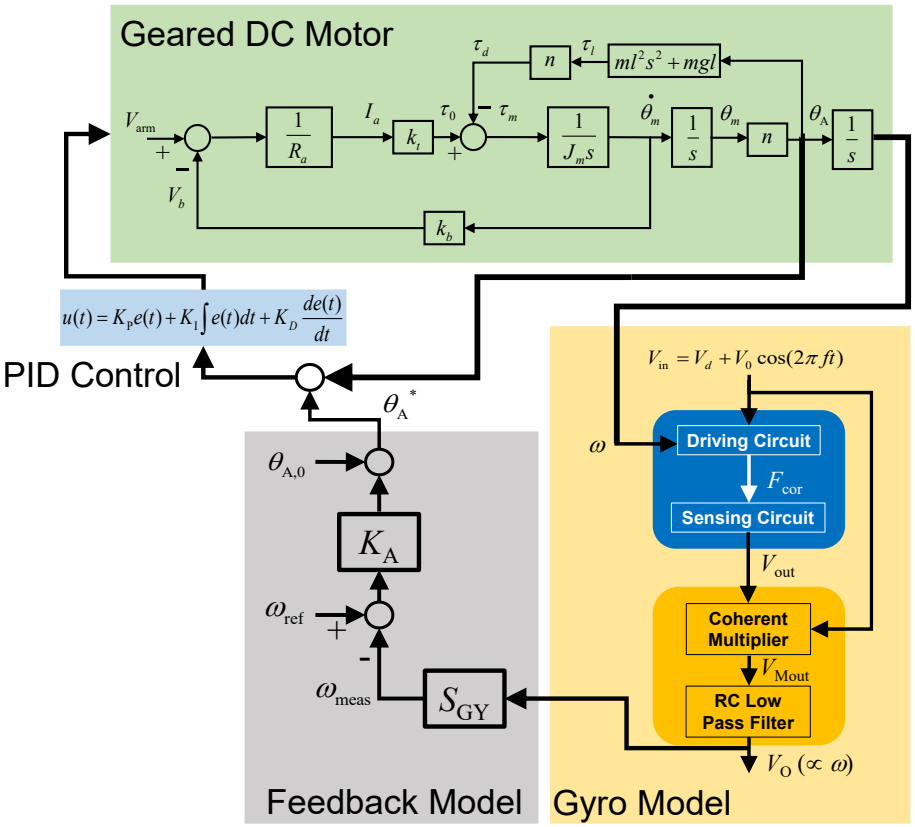

Fig. 4.9. Experimental verification of the developed electro-mechanical model of the single-axis vibratory gyro sensor.

the length of the constant length inverted pendulum form L_0 to L and the new length L no more a constant value but a function of the ankle-pitch motor angle. In order to consider the change in L, the (4.4) can be re-written as,

$$ML^2 \frac{d^2\theta}{dt^2} = MgL\sin\theta + FL\cos\theta \tag{4.5}$$

$$L = \sqrt{L_0^2 + 2bl\sin\theta_A} \tag{4.6}$$

The control mechanism of the robot posture by rotating the motor angle θ_A is shown in Fig. 4.10. As the reference ankle-pitch motor angle changes, the motor rotates due to the compensating torque controlled by the in-built PID controller. The x-axis projection of the robot-COM is considered as a reference point to be controlled by the ankle-torque compensation. In Fig. 4.11 the transient response of the COM projection is shown. To ensure the postural stability for this inverted pendulum, the x-axis projection has to follow the boundary condition (derived from (4.3)) given by

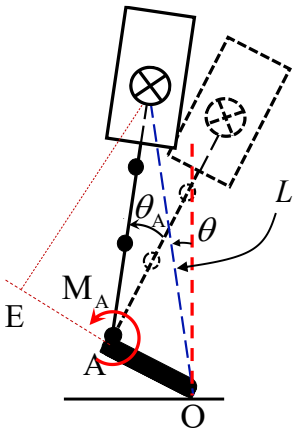

Fig. 4.11. The compensation of ankle-pitch motor stabilize the robot posture. The implemented control system brings the robot within the static stability margin (4.3), preventing the falling down.

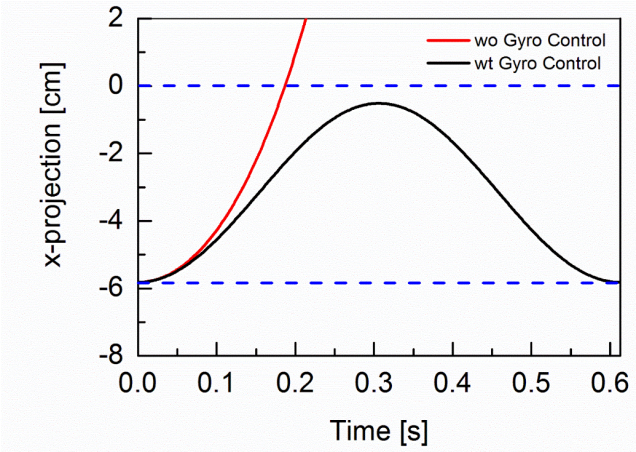

Fig. 4.10. The projection of the robot-COM is brought back by the ankle-pitch motor compensation in order to stabilize the robot posture.

$$-b \le x_{\text{COM}} \le 0 \tag{4.7}$$

In Fig. 4.11, it is observed that the gyro sensor based feedback control system brings the *x*-axis projection of robot-COM within this limit (4.7), thus preventing the robot from falling down.

4.3.3 Experimental Verification

The proposed control system is experimentally verified using the humanoid robot KONDO KHR-3HV. The robot is exerted with a push-force from front and behind to verify the control system when the robot is undergoing the positive and negative pitch motions

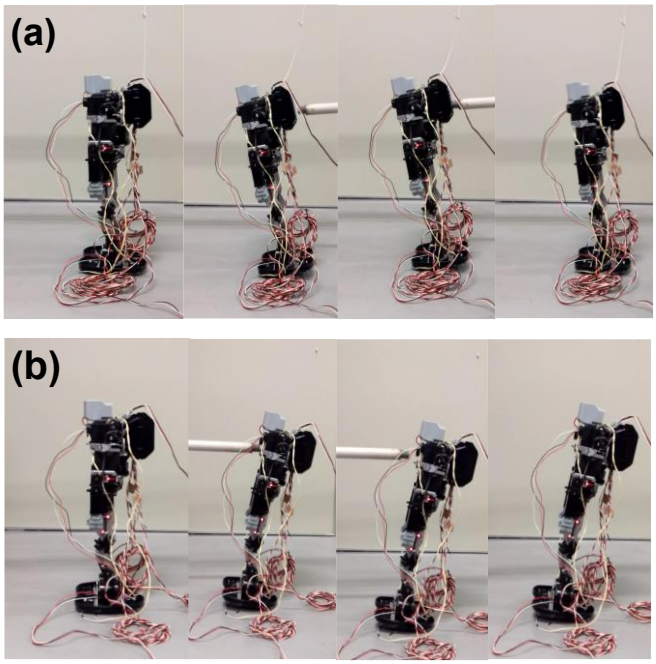

Fig. 4.12. Push recovery experiments when the robot is undergoing negative pitch motion and positive pitch motion (b).

respectively. The negative and positive pitch-motion control of the are shown in Fig. 4.12(a) and (b) respectively.

4.4 On-site Implementation

Recently human-robot interaction (HRI) research has gained momentum specially focussing on the usefulness of the robots in the real world. The research on the push-force recovery can be considered to be a very basic part of HRI research. This focusses on the physical interaction between human and robot. It is true that we say this to be a disturbance from the robot-side, but this disturbance is very realistic when we talk from an interaction point of view.

The disturbance control system proposed in this thesis was tested in a robot-robot interaction platform. The robot KHR-3HV integrated with the push-force disturbance control system participated in the 18th ROBO-ONE Light competition and 34th ROBO-ONE competition held in Kobe, Japan on February 22-23, 2019 (see Fig. 4.13). The competition staged battle between light-weight robots, where the control strategies of robots to encounter external disturbances imparted by opponent robot, is tested. The robot qualified in the first two rounds and could successfully secure its place up to the semi-final.

Fig. 4.14. Battle of light-weight humanoid robot in ROBO-ONE Light Competition. (Image Source: Biped Robot Association, Japan)

Fig. 4.13. Robot KONDO KHR-3HV with the integrated push-recovery control system designed by HiSIM Research Center, Hiroshima University. The story was covered by Japanese magazine ROBOCON. (Image Source: ROBOCON Magazine, May Issue, 2019)

The work was covered in the media as well as in the magazine ROBOCON (in Japanese) as shown in Fig. 4.14.

The observations regarding the performance of the robot during the competition directs the researcher towards some basic future-work to be carried out for the development of the light-weight robots. The possible take-over from this work are given as follows:

- Development of physics engine based simulation environment for studying the robot-robot interaction.

- Implementation of the postural control strategy based on hip-torque compensation followed by step-over strategy. This strategies are realized in human-sized robots, but not yet implemented for light-weight humanoid robot.

4.5 Conclusion

This chapter presented an electromechanical model of an analog single-axis vibratory MEMS gyros sensor. The model is implemented in Verilog-AMS and the circuits are simulated in a commercial SPICE simulator. The transient characteristics of the gyro sensor shows the requirement of an envelope detector to detect the applied angular-pitch velocity. The modulated out of the sensing circuit is fed to the envelope detected comprising of a coherent multiplier and a RC low pass filter. The filter characteristics of the RC low pass filter determines the frequency response of the output of the detector. The static characteristics of the gyro sensor is experimentally verified with an analog gyro sensor KRG-4.

Further the gyro sensor model is integrated to a control system for stabilizing the robot posture when the robot is exerted with an external push force. The dynamics of the robot is modelled with a constant length inverted pendulum. The pitch-angular velocity of the robot is measured by the gyro-sensor model to control the ankle-pitch-motor angle. This makes the robot stable by restricting the COM-projection to be within the static stability margin of the robot. The control system was verified experimentally for the positive and negative pitch motion of the robot when exerted with a constant force.

This chapter marks the end of the investigation on the static stability of the robot. The following chapter presents the dynamic control of the robot-walking and discusses the vibration control in light-weight robot.

Chapter 5: Vibration Control in Humanoid Robots

5.1 Introduction

Light-weight humanoid robots comes with a problem of vibration while walking. This vibration is observed when the joint-angle motors are controlled by feedback angular velocity of the robot. In the previous chapter it is observed that angular velocity of the robot plays important role in controlling the robot-posture when the robot is subjected to external disturbance, be it an external push-force or gravity force. For that, an extensive analysis of the gyro sensor is carried out, as it helps the author to understand the working of the sensor to measure the angular-pitch velocity of the robot-torso.

In this chapter the measured angular-pitch velocity is used to control the robot posture, when the robot walks on an inclined surface. A gyro-sensor-based feedback-control system to control the ankle-pitch and hip-pitch motors of the robot for stable walking on inclined surfaces is proposed. The gyro-sensor is integrated at the backpack of the robot as shown in Fig. 5.1. The ankle-pitch motors and hip-pitch motors are observed to play significant role in stabilizing the robot posture while walking on an inclined surface. The pitch-motor

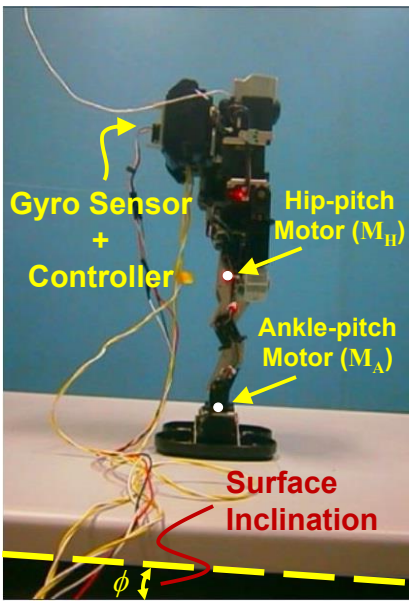

Fig. 5.1. KONDO KHR-3HV Humanoid Robot integrated with a gyro sensor for balancing on an inclined surface with inclination angle ϕ.

angles are controlled in a stepwise manner (see Fig. 5.2) based on the difference between the measured and reference angular-pitch velocity of the robot. The reference pitch-angular velocity of robot is modelled using an Inverted Pendulum Model (hereafter IPM). The walking pattern implemented in the robot is characterized by a gait cycle period of 2.31s as shown in Fig. 5.3(b). This gait cycle period corresponds to a fundamental walking frequency f_0=1.73 Hz. When the angular-pitch velocity is analyzed in the frequency domain, the frequency f_0 is observed to have a prominent peak.

At higher surface inclination, the ankle-pitch motors and the hip-pitch motors are controlled by the measured angular-pitch velocity to stabilize the robot posture. This additional feedback-loop to the motor control systems gives rise to higher frequency-peaks when the gait pattern (angular-pitch velocity) is analyzed in frequency domain. This is the main reason behind the vibration in the robot.

The structure of this chapter is as follows. Section 5.2 describes the experimental setup used to carry out the walking experiments with the humanoid robot on an inclined surface with low surface friction. Then the experimental results are discussed. In section 5.3, the frequency-domain analysis of the angular-pitch velocity of the humanoid robot, obtained from the experiments (discussed in section 5.2), are presented. Section 5.4 describes the measured angular-pitch velocity of the robot walking on an inclined surface with increased

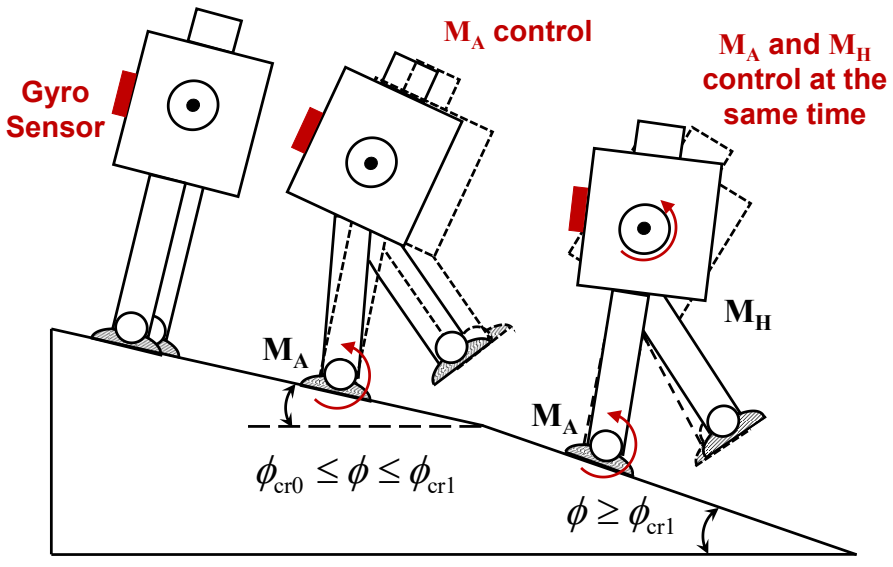

Fig. 5.2. The gyro-sensor measured angular-pitch velocity of the robot body is used to control the ankle-pitch motor (M_A) above a critical inclination ϕ_{cr0} and is then used additionally to control the hip-pitch motor (M_H) above a larger critical inclination ϕ_{cr1}, in order to balance the robot walking.

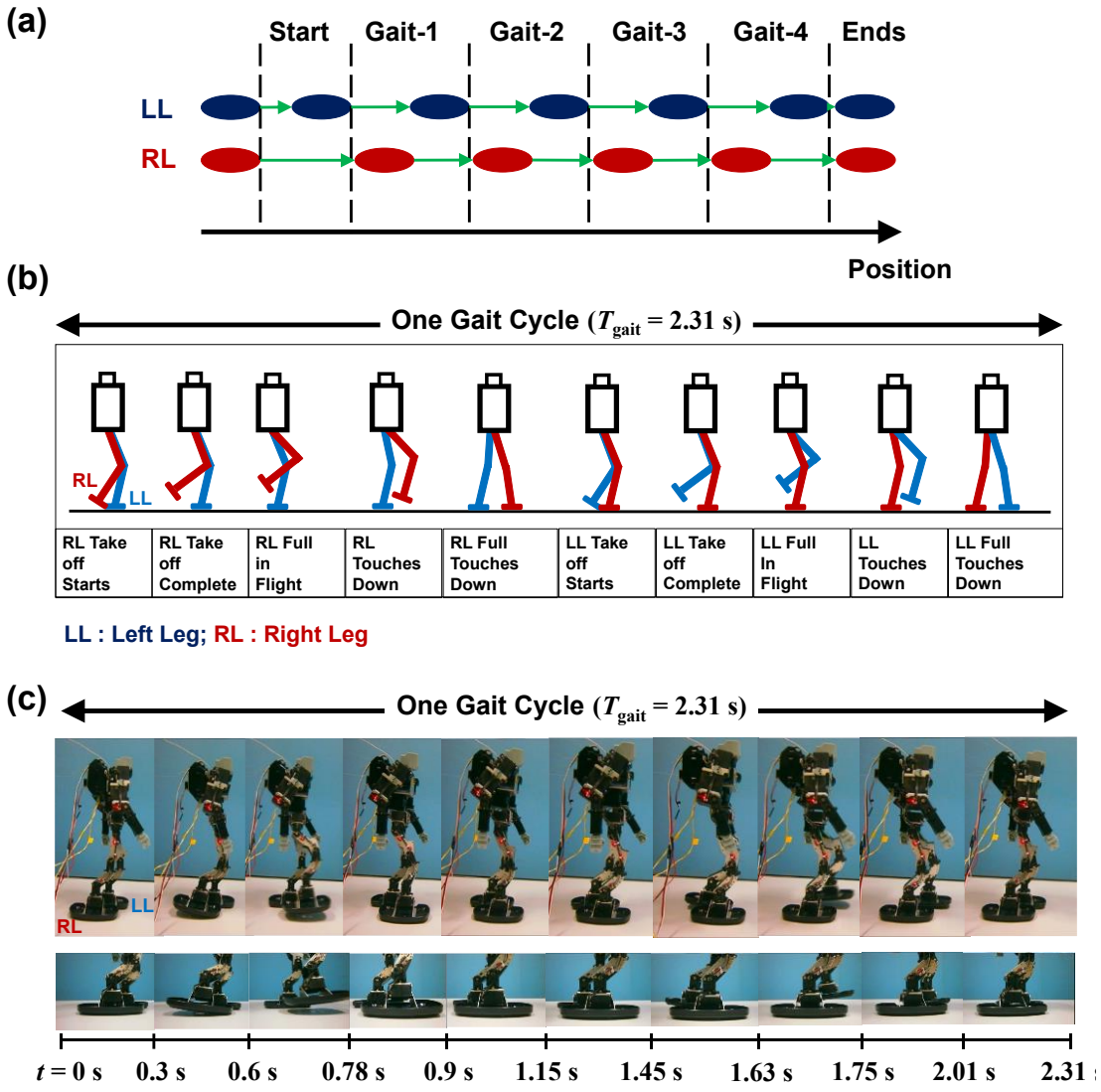

Fig. 5.3. (a) Walking pattern of the robot, illustrating the gait-cycle repetition of the robot, with one half of a gait cycle at the beginning, then 4 complete gait cycles and finally one half of a gait cycle at the end. (b) One gait cycle is zoomed to show the gait pattern of the robot KONDO KHR-3HV. T_{gait}: period of a gait cycle; T_{walk}: total time for which the robot has walked. (c) Photos showing the gait pattern implemented in one gait cycle of the robot with the zoomed foot-placements patterns at the bottom.

surface friction. In section 5.5 the IPM is extended to explain the frequency-response of the robot's gait pattern. A second-order control-system analysis is carried out in order to explain the response of the implemented motor-control system. To explain the origin of the higher-order harmonics of f_0, a nonlinear IPM is used. The nonlinearity due to the surface inclination can be explained using the nonlinear IPM. Section 5.6 concludes the paper highlighting the novel outcomes of the presented work.

5.2 Robot Walking Experiments

5.2.1 Motor Control System

The robot is equipped with 17 KONDO KRS-2552RHV DC servomotors [89] for walking or performing any other work. Among these 17 motors, 4 motors, one ankle-pitch motor (M_A) and one hip-pitch motor (M_H) on each leg, are controlled by the feedback

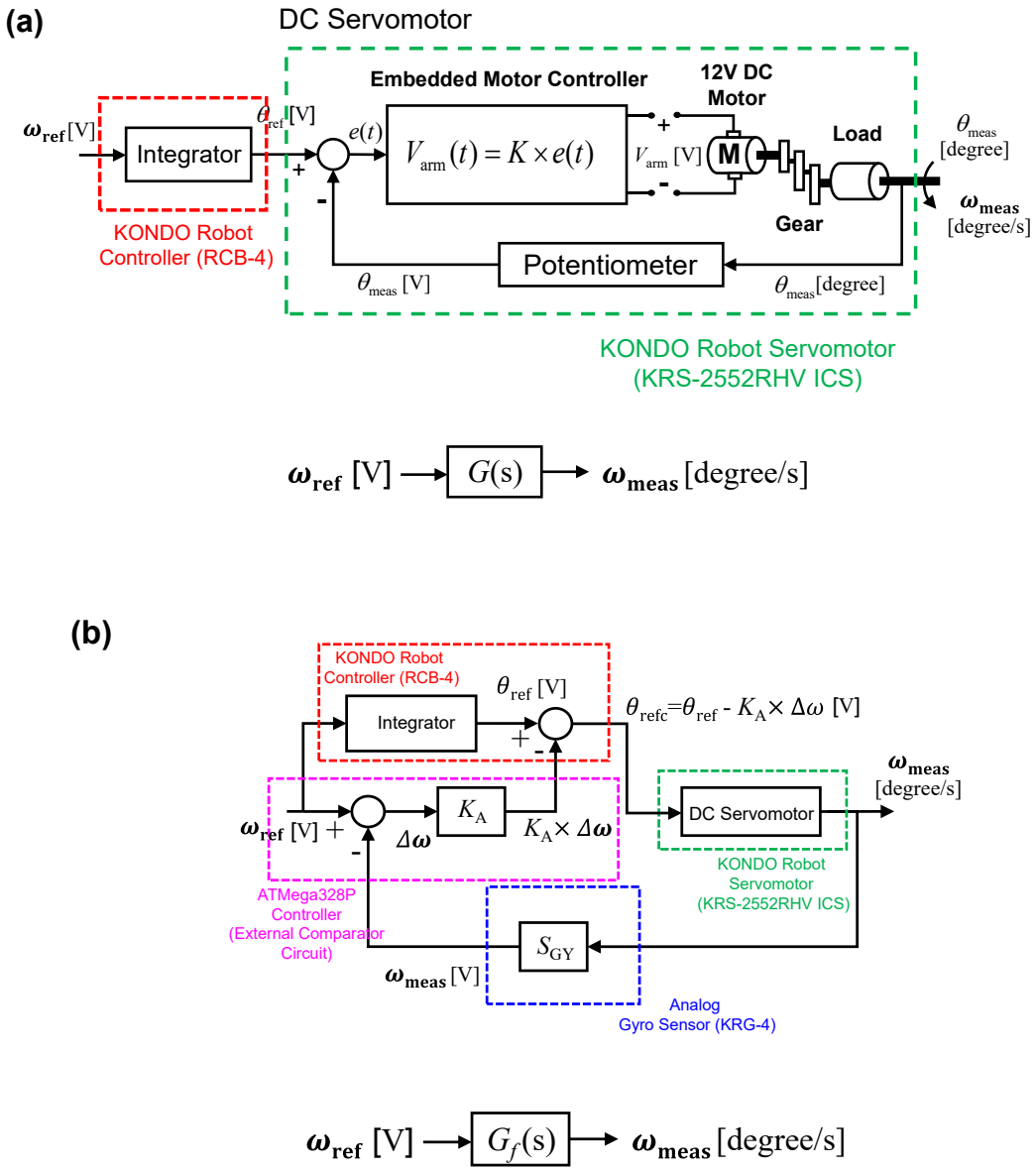

Fig. 5.4. (a) Schematic diagram of the control circuit of DC servomotor used in the experiment. The transfer-function formulation used for modeling the motor-control system without the gyro-sensor feedback loop. (b) Schematic diagram of the motor-control system, implemented for adjusting the robot's ankle-pitch motor on inclined surfaces.

angular-pitch velocity, in order to realize stable walking of the robot on an inclined surface. The internal control circuit of each DC servomotor is shown in Fig. 5.4(a). The DC servomotor has a 12V DC geared motor with a potentiometer-based position-feedback loop. The embedded controller is implemented on a PIC16F690 platform [90]. The controller controls the DC motor's armature voltage V_{arm}, based on the difference between a reference motor angle θ_{ref} (in [V]) and the motor angle θ_{meas} (in [V]). The motor angle θ_{meas} is measured by the potentiometer. The reference motor angle θ_{ref} (in [V]) is programmed in to the robot controller RCB-4 [91] integrating the reference angular–pitch velocity ω_{ref} (in [V]). To calculate the output angular-pitch velocity, a transfer-function formulation is required, as shown in Fig. 5.4(a) [92-98]. The transfer function of the motor-control system without the external gyro-sensor-feedback loop can be written in the s-domain (see Fig. 5.4(a)) as

$$G(s) = \frac{K}{Js^2 + Bs + K} \tag{5.1}$$

where J and B are equivalent inertia elements (inertia and viscous friction of the servo motor) and K is the proportional gain of the controller, embedded inside the KONDO servomotor KRS-2552RHV.

The discussed motor-control system is integrated with an additional gyro-sensor-based feedback controller, as shown in Fig. 5.4(b). In the motor-control system with gyro-sensor feedback, the angular-pitch velocity of the robot is measured by a single-axis analog gyro sensor KRG-4 [99], which is attached on the robot torso (in the backpack of the robot). The measured angular-pitch velocity (in [V]) by the gyro sensor is given by

$$\omega_{meas}\ [\text{V}] = S_{GY} \times \omega_{meas}\ [\text{degree/s}] \tag{5.2}$$

where S_{GY} is the sensitivity of this single-axis analog gyro sensor, equal to 0.67 mV·s/degree. The measured angular-pitch velocity ω_{meas} of the robot (in [V]) is fed back to an external comparator circuit which is implemented into an ATmega328P controller [100]. The comparator circuit calculates the difference between the measured angular-pitch velocity ω_{meas} (in [V]) and a reference angular-pitch velocity ω_{ref} (in [V]), which is also pre-programmed into the memory of the external controller. This difference is amplified with the externally "tunable" feedback gain K_A for the ankle-pitch motor (or K_H for the hip-pitch motor). The output of the amplifier is then fed back to the robot-controller RCB-4, to

adjust the reference value of the ankle-pitch-motor angle according the following the equation.

$$\begin{aligned}\theta_{\text{refc}} &= \theta_{\text{ref}} - K_{\text{A}} \times (\omega_{\text{ref}} - \omega_{\text{meas}})\ [\text{V}] \\ &= \theta_{\text{ref}} - K_{\text{A}} \times \Delta\omega\ [\text{V}]\end{aligned} \tag{5.3}$$

where K_{A} is the tunable feedback gain of the amplifier, θ_{ref} is the reference angle for ankle-pitch motor (in [V]) and θ_{refc} (in [V]) is the adjusted reference angle for motor rotation. The adjusted reference angle is then used to control the servomotor rotation as shown in Fig. 5.4(b). For other motors, such as the hip-pitch motors M_{H}, the control is independently done in the same way as for ankle-pitch motor M_{A}.

The feedback gain K_{A} (or K_{H}) increases the sensitivity of the motor-angle control on the comparator output. Therefore, for a higher effect of the comparator output, a larger K_{A} value is needed to adjust the motor angle by a larger extent. In the literature of compliance modelling for actuators [101], gain K_{A} effects the stiffness of a motor-load transmission system. The frequency-response analysis of such a motor-load-transmission systems shows, that the proportional feedback-gain largely effects the vibrations in the system. Therefore, a proportional control is implemented here to analyze the effect of gain K_{A} on the system performance, before extending it to controllers having multiple tunable gains, e.g., Proportional-Derivative (PD) controllers. This becomes clearer in the following section, when the effect of the gain K_{A} on the robot's gait data is discussed in detail.

When the feedback loop with the gyro-sensor control is implemented, it is observed that the viscous friction coefficient is reduced from B to B_f as

$$B_f = B - K_{\text{A}} S_{\text{GY}} \tag{5.4}$$

where S_{GY} is the gyro-sensor sensitivity and K_{A} is the tunable gain in the feedback loop. Due to the additional gyro-sensor-feedback loop, the modified transfer function G_f of the overall motor-control system (see Fig. 5.4(b)) is

$$G_f(s) = \frac{(1 - sK_{\text{A}}S_{\text{GY}})K}{Js^2 + B_f s + K} \tag{5.5}$$

5.2.2 Experimental Setup

A single-axis analog gyro sensor is attached on the robot torso as indicated in Fig. 5.1. The locations of ankle-pitch motor (M_{A}) and hip-pitch motor (M_{H}) are also indicated in

Fig. 5.1. To analyze the robot walking and the effect of the motor-control scheme for robot-posture balancing, a smooth surface is inclined by an angle ϕ, as can be seen in Fig. 5.2. The inclination of the surface is gradually increased from 0° in a stepwise manner, until the robot falls down during walking. The angular-pitch velocity of the robot is measured, when the robot walks on this surface. This angular-pitch velocity is a characteristic of the robot gait-pattern. The measurements are performed under following three conditions:

1. The robot is walking on the inclined surfaces without any gyro-sensor-based feedback control, until it becomes unstable beyond a critical inclination ϕ_{cr0}.
2. Beyond the critical inclination ϕ_{cr0}, the ankle-pitch motor (M_A) is controlled by the gyro-sensor feedback. This allows the robot to walk up to a higher critical surface inclination ϕ_{cr1}. The robot becomes unstable beyond ϕ_{cr1}.
3. Beyond ϕ_{cr1} the hip-pitch motor (M_H) is also controlled by the gyro-sensor feedback in addition to the ankle-pitch motor. This enables the robot to walk stably on inclined surfaces above the critical surface inclination ϕ_{cr1}.

The stepwise adjustments of the motor control, based on the gyro-sensor feedback, is schematically illustrated in Fig. 5.2.

5.2.3 Robot-Gait Implementation

The angular-pitch velocity of the robot is measured, when the robot is walking on an uninclined surface ($\phi = 0°$), as schematically illustrated in Fig. 5.3. The gait-cycle period (T_{gait}) of the robot is set to 2.31 seconds. In the walking program implemented in the robot controller RCB-4, there are a start phase (half a gait), four complete gait cycles and an end phase (half a gait). The measured angular-pitch velocity ω_{meas} of the robot-torso for $\phi = 0°$ is shown in Fig. 5.5(a). It can be observed that the pattern of ω_{meas} becomes quite identical after the second gait cycle. Therefore the ω_{meas} waveform of the third gait (Gait-3) cycle is taken as a reference pattern for ω_{meas} for further analysis of the robot's walking dynamics. The zoomed waveform of Gait-3 is shown in Fig. 5.5(b), where the schematic robot motions of this walking cycle are depicted above the graph. The schematic robot motion shows the dominant motor action during the walking. For $\phi = 0°$ the reference gait cycle is characterized by four peaks (1, 2, 3 and 4), as shown in Fig. 5.5(b). Peaks 1 and 2 occur due to the positive angular-pitch velocity of the robot while swinging the right leg during first half of the gait cycle.

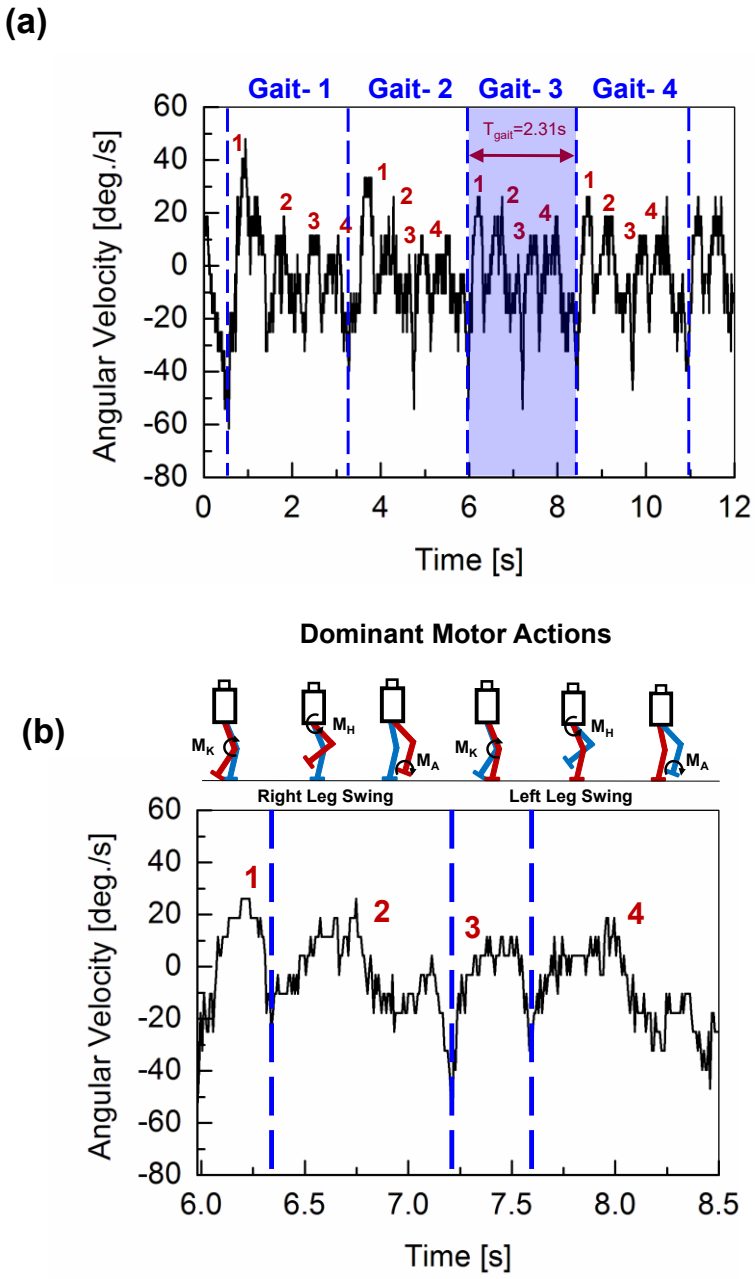

Fig. 5.5. (a) Angular-pitch velocity of the robot torso when the robot walks on an uninclined surface ($\phi = 0^o$). (b) The angular-pitch velocity of the third gait cycle as detected by the gyro sensor. The third gait cycle is shown in expanded form, to explain the gait pattern of the robot on the uninclined surface.

Similarly, peaks 3 and 4 occur while swinging the left leg during second half of the gait cycle. These four peaks characterize a gait cycle in the time-domain. In the following subsection, it will be discussed how these four peaks are changed due to the effect of surface inclination and gyro-sensor-based feedback control. This analysis is the core of this chapter.

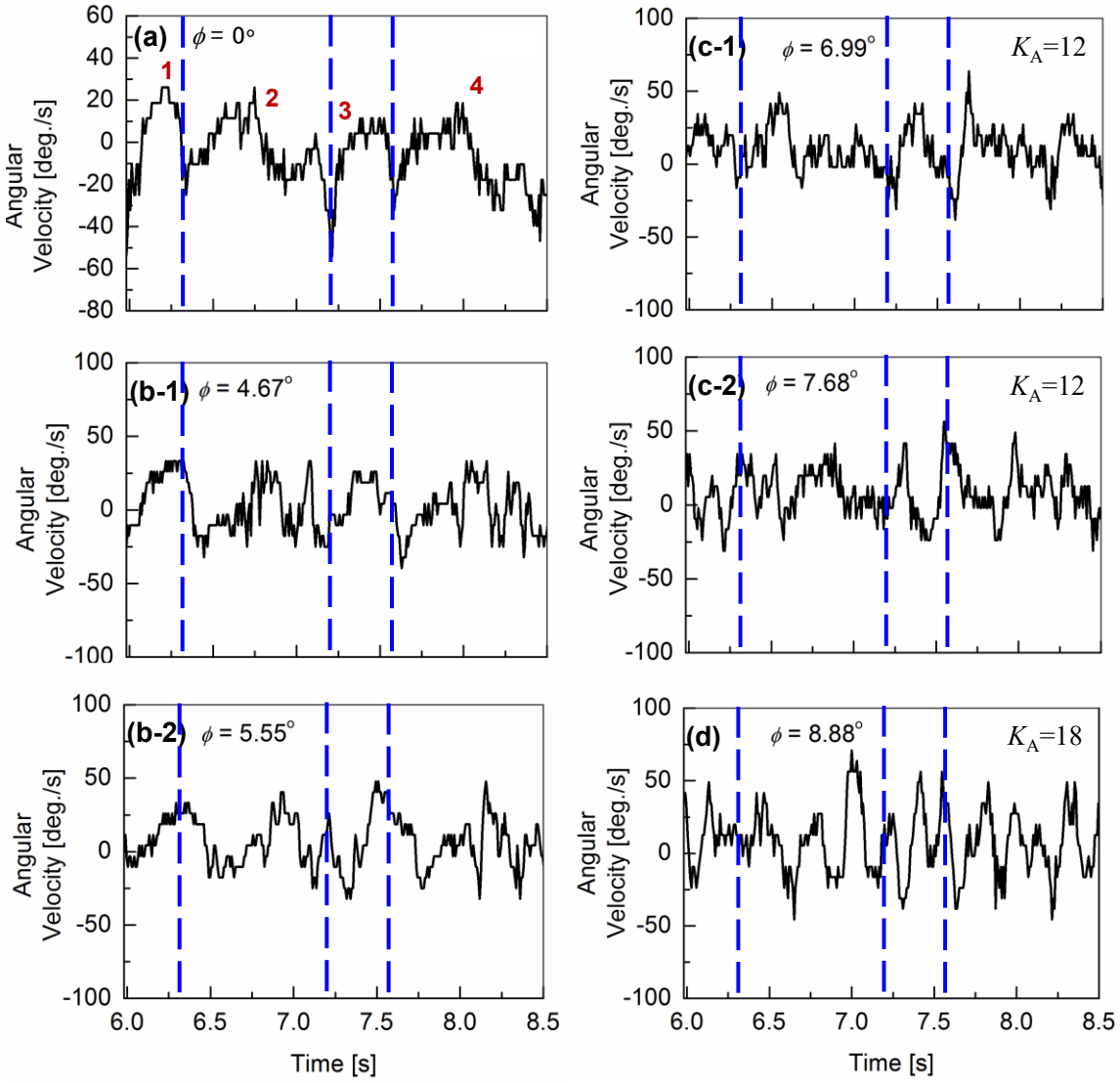

Fig. 5.6. Angular velocities of the robot's pitch motion during a gait cycle, measured for different surface inclinations. An increase in amplitude and number of oscillations is observed at higher surface inclinations with feedback control. The results are compared with angular-pitch velocities, measured for ϕ=0°.

The measured gait cycle for $\phi = 0^{o}$ is considered as the "fingerprint" of the robot walking, which provides the basic gait pattern of the robot.

5.2.4 Experimental Results

The angular-pitch velocities ω_{meas} of Gait-3 with different increased surface inclinations ϕ are shown in Fig. 5.6. The robot walking is studied first by increasing ϕ from 0° to ϕ_{cr0}=5.55°. In that case the robot's motor control system is not having the additional feedback loop of the gyro sensor. It can be seen, that additional oscillatory patterns appear

in the ω_{meas} waveforms and these become more obvious as ϕ increases. Due to an amplitude increase in the additional oscillatory patterns, the designated peaks 1, 2, 3 and 4 become indistinguishable. As ϕ approaches ϕ_{cr0}, the robot becomes more unstable due to the gravity compensation problem. Beyond the critical surface inclination ϕ_{cr0}, the robot falls down when it starts to walk. Therefore, the ankle-pitch motor M_A is controlled beyond ϕ_{cr0} = 5.55°. A proportional control system is implemented into the robot as shown in Fig. 5.4(a). This proportional control system uses a gain K_A to control the ankle-pitch motor angle, where K_A =12 makes the robot walking stable beyond ϕ_{cr0}, as shown in Fig. 5.6(c-1). At lower values of K_A, the compensating-torque at the ankle-pitch motor is not sufficient to adjust the gravity effect on the robot. With K_A=12 the robot can walk on surfaces with inclinations up to ϕ = 8.88°. Beyond ϕ_{cr0}=5.55° it is observed that the oscillatory nature of the angular-pitch velocity increases largely due to implementation of the gyro-sensor-based feedback-control system. The characterizing peaks (1, 2, 3 and 4) are no more observed distinctly and the pattern of the third gait cycle becomes more oscillatory as compared to the fundamental gait data (Fig. 5.6(a)). At ϕ = 8.88° it is observed, that even though the robot can walk on the downslope, it starts slipping on the surface. If K_A is increased further to 18, the slipping is reduced and the robot can then walk down the slope more safely. However, the robot body vibrates at much higher frequency when the gain K_A is increased than observed for a surface inclination of ϕ = 5.55°.

At ϕ = 9.7° the robot starts to slip again, even with K_A=18. If K_A is increased to a value higher than 18, the vibrations of the robot body dominates the robot motion, which makes the robot walking very unstable. Therefore, the hip-pitch motor M_H is additionally controlled beyond ϕ = 9.7°, in the same way as M_A. It is important to note here that M_A and M_H are controlled independently. This M_H motor control, while keeping K_A = 12 for M_A-control, reduces the slipping and makes the robot walking stable. But as two motors are controlled now, the oscillation increases as compared to the previous case when only ankle-pitch motor was controlled. The feedback gain K_H for the hip-pitch-motor control is varied from 12 to 14. It is observed, that the vibration increases at the higher value of K_H = 14 (see Fig. 5.7(a)), whereas the slipping dominates at lower values such as K_H = 12, similar to the results for the ankle-pitch-motor control with K_A. Therefore the K_H-value is set to 13, where both slipping and vibrations are optimized, and the robot can walk down the slope without falling for a surface inclination up to ϕ =10.2°, as verified in Fig. 5.7(b). For ϕ > 10.2°, the robot walking becomes again unstable, mostly because of an increased slipping.

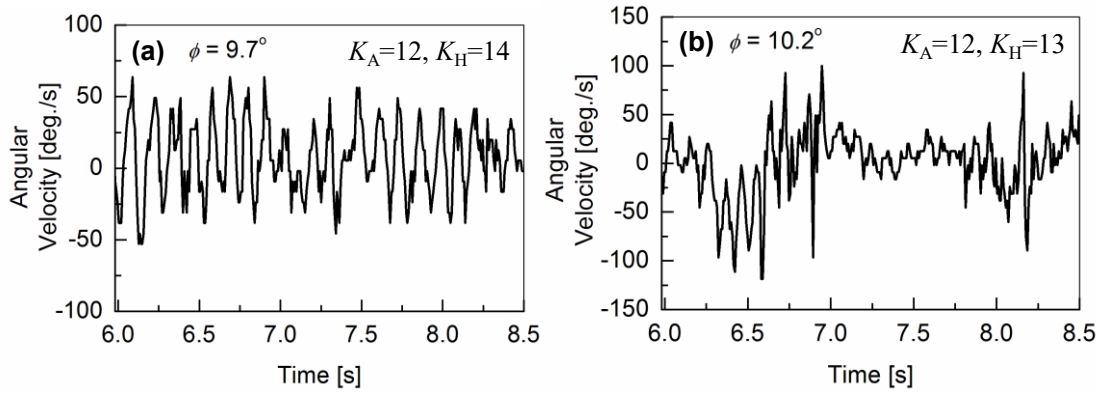

Fig. 5.7. Angular-pitch velocity for a gait cycle with both ankle-pitch-motor control and hip-pitch-motor control, measured at different higher surface inclinations. (a) Robot vibrations increase for K_H=14 in the hip-pitch-motor control. (b) K_A=12 and K_H=13 are an optimized motor-control setting, allowing stable down-slope walking up to inclinations of ϕ=10.2°.

5.3 Analysis of Experimental Results

The experimental results show that the gyro-sensor based feedback control enables the robot walking on inclined surfaces, but induces vibrations of the robot-body at the same time. Here, the focus is given to the origin of the vibrations. It can be observed in Fig. 5.6 and Fig. 5.7, that the ω_{meas} waveform becomes complex and that no clear peaks are visible at higher surface inclinations. To investigate the origin of the oscillation increase, a Fourier Transformation is carried out for the time-domain measurements of the angular-pitch velocity of the robot-torso. Fig. 5.8 and Fig. 5.9 depict the results for measured angular-pitch velocity waveforms ω_{meas} in the frequency domain. Without the M_A control for $\phi \leq$ 5.55°, a single dominant peak at f_0 =1.73 Hz is observed, which is the fundamental walking frequency (see Figs. 8(b-1) and 8(b-2)). The same measurements are repeated several times in order to verify the statistical significance, and are plotted together in the graphs of Fig. 5.8.

For $\phi \geq$ 6.99°, the feedback mechanism is implemented with higher K_A values, as shown in Figs. 5.8(c-1), 5.8(c-2) and 5.8(d). It is observed that contributions up to second-order harmonics (f_1 and f_2) are significant. These higher frequency oscillations refer to the oscillation increase in the time-domain measurements. For ϕ = 6.99° and 7.68° an additional frequency peak f_{A0} is observed at 2.58 Hz, as shown in Figs. 5.8(c-1) and 5.8(c-2), and this originates from the gyro-sensor-based feedback control of the ankle-pitch motor.

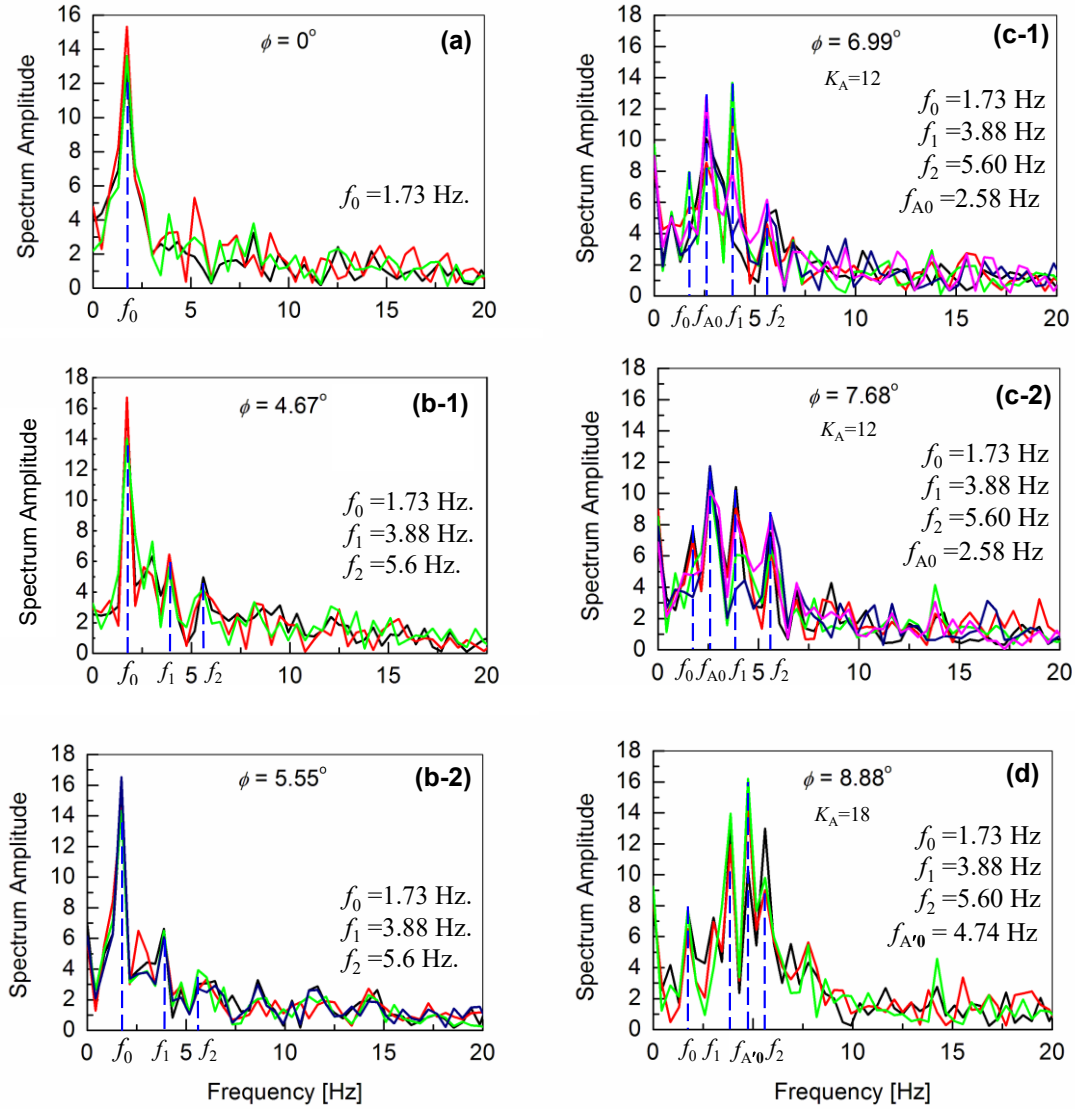

Fig. 5.8. Fourier analysis of the angular-pitch velocity waveforms measured by the gyro sensor for the robot-body, when the robot is walking stably on inclined surfaces without ((a), (b-1), (b-2)) and with ((c-1), (c-2), (d)) gyro-sensor feedback. The frequency f_{A0} = 2.58 Hz (see (c-1) and (c-2)) is induced by the motor feedback with K_A=12, which is shifted to $f_{A'0}$ = 4.74 Hz (see (d)) due to an increased K_A.

As the surface inclination increases further to ϕ = 8.88°, oscillation frequencies are shifted to higher values. This shift to higher frequencies becomes quite drastic when introducing the K_H control, as can be seen in Fig. 5.9. Under such a condition the robot-gait pattern is no more detectable in the time-domain measurements. At the surface inclination of ϕ = 8.88°, an increased feedback gain K_A of 18 is required, which however causes larger oscillatory behavior of the robot, which can be seen in Fig. 5.6(d).

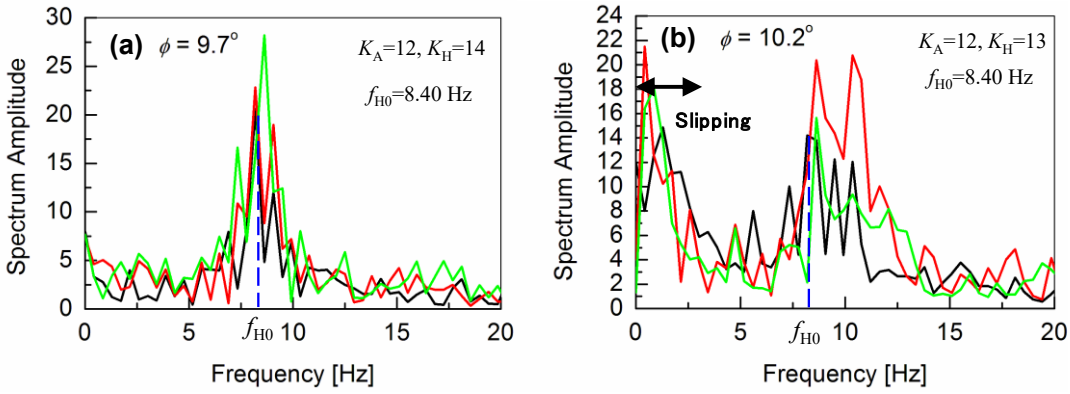

Fig. 5.9. Fourier transformation of the angular-pitch velocity, when both ankle-pitch and hip-pitch motors are controlled by the gyro sensor. It can be seen that the contribution due to the fundamental walking frequency of 1.73 Hz is no more observable. Instead a peak at higher frequency is observed. The measured time-domain waveform becomes more oscillatory, as shown in Fig. 5.7.

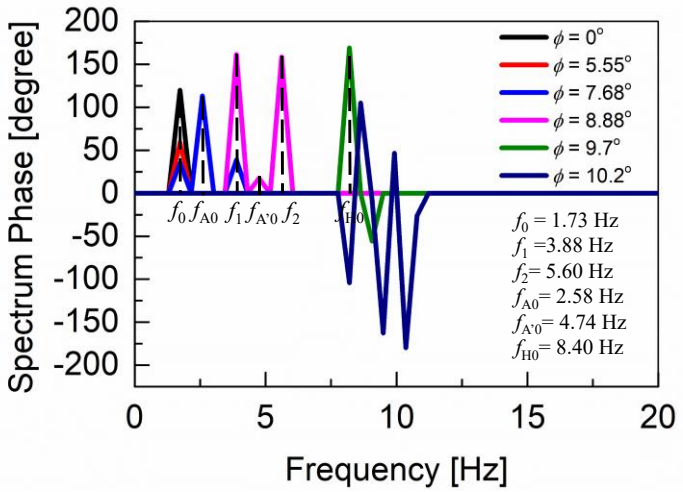

Fig. 5.10. Phase plots for the measured pitch velocity in the cases of various surface inclinations. The contributing frequencies are indicated, confirming the findings from the corresponding amplitude plots. A tolerance value of 33% of the absolute maximum in the amplitude spectrum is used for the phase-plot calculation.

Frequency responses of the measured angular-pitch velocity at $\phi = 9.7^{o}$ and $\phi = 10.2^{o}$ are shown in Fig. 5.9(a) and Fig. 5.9(b), respectively. The frequency peaks are observed at higher frequencies between 7.5 Hz and 10 Hz for both cases. Corresponding phase plots (spectrum phase vs. frequency) of the angular-pitch velocity are shown in Fig. 5.10. A relatively high tolerance value of 33% of the maximum absolute value in the amplitude spectrum is used during the calculation of these phase plots, in order to remove the

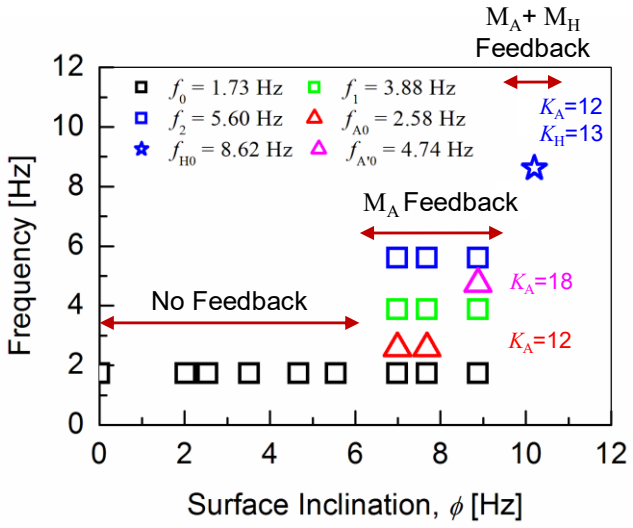

Fig. 5.11. Contributing frequencies as extracted from the frequency-response analysis of the angular-pitch velocity as a function of surface inclination ϕ.

unwanted effects of the quite large noise in the measured time-domain data. The phase plots show the peaks due to the contributing frequencies, as supported by the amplitude plots for the angular-pitch velocity. The data suggests, that the linearity of the gait pattern is completely lost, as can be observed in particular from the diminished amplitude at f_0=1.73 Hz. The dominant frequency peaks as a function of the surface inclination ϕ are summarized in Fig. 5.11. Initially the regular gait pattern of f_0 is observed. By introducing the feedback control, however, additional control frequencies appear. By increasing the K_A value to 18, the additional frequency due to feedback increases up to $f_{A'0}$ =4.74 Hz (see Fig. 5.8(d)). The introduction the K_H control causes an additional frequency at f_{H0} = 8.40 Hz, as shown in Fig. 5.9(a). This relatively high frequency controls the gait pattern of the robot, making the robot unstable due to increase in vibrations. By increasing the surface inclination up to ϕ =10.2°, strong peaks appear also at low frequency (see Fig. 5.9(b)), which are attributed to the disturbance caused to the walking due to the slipping on the surface.

5.4 Experiments with Robot-Foot Friction

It was found that the increase of the feedback gains K_A and K_H reduces slipping of the robot feet, but at the same time the vibration of the robot-body increases. These robot vibrations can be attributed to the joint angle control through the gyro sensor feedback. Figures 5.12(d), 5.12(d-2) and 5.12(d-3) summarize the features of the K_A control for ϕ =

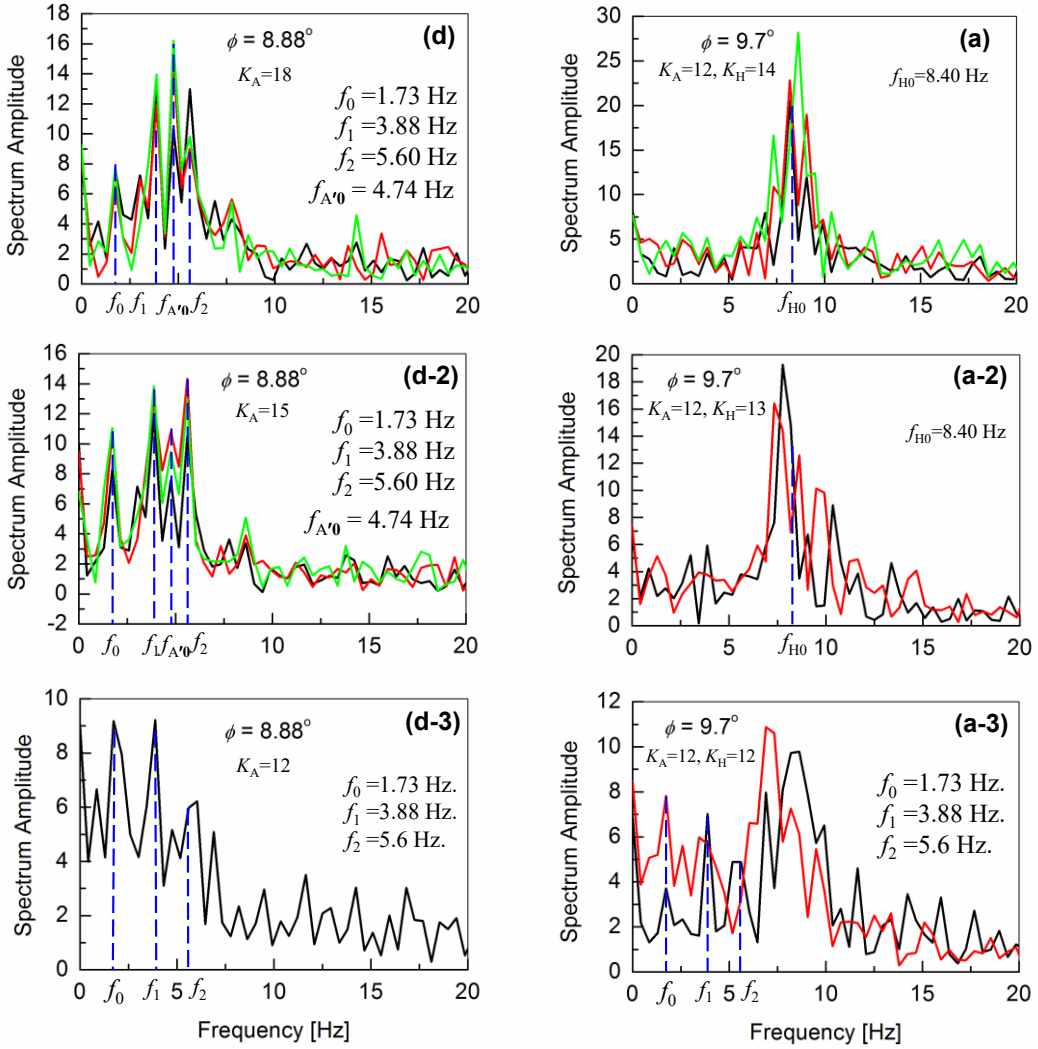

Fig. 5.12. Fourier analysis of the angular-pitch velocity of the robot walking on an inclined surface for $\phi = 8.88^o$ with varying K_A (18 in (d), 15 in (d-2) and 12 in (d-3)) and for $\phi = 9.7^o$ with varying K_H (14 in (a), 13 in (a-2) and 12 in (a-3)) By reducing K_A and K_H values, the robot posture becomes unstable due to slipping, as shown in (d-3) and (a-3).

8.88°. Even though the robot feet become quite slippery, the fundamental walking frequency f_0 is clearly observed for all K_A values. With increased K_A value, it can be seen that the nonlinearity of the gait-pattern increases. The nonlinearity continues to increase with the additional control of K_H. This can be seen in Figs. 5.12(a), 5.12(a-2) and 5.12(a-3) for ϕ = 9.7°, where the higher frequencies between 7.5 Hz and 10 Hz are due to the feedback-motor-control system for the hip-pitch motor M_H.

Till now the robot walking experiments have been carried out on an inclined surfaces with low friction, to verify major factors which prevent the robot from stable walking. In

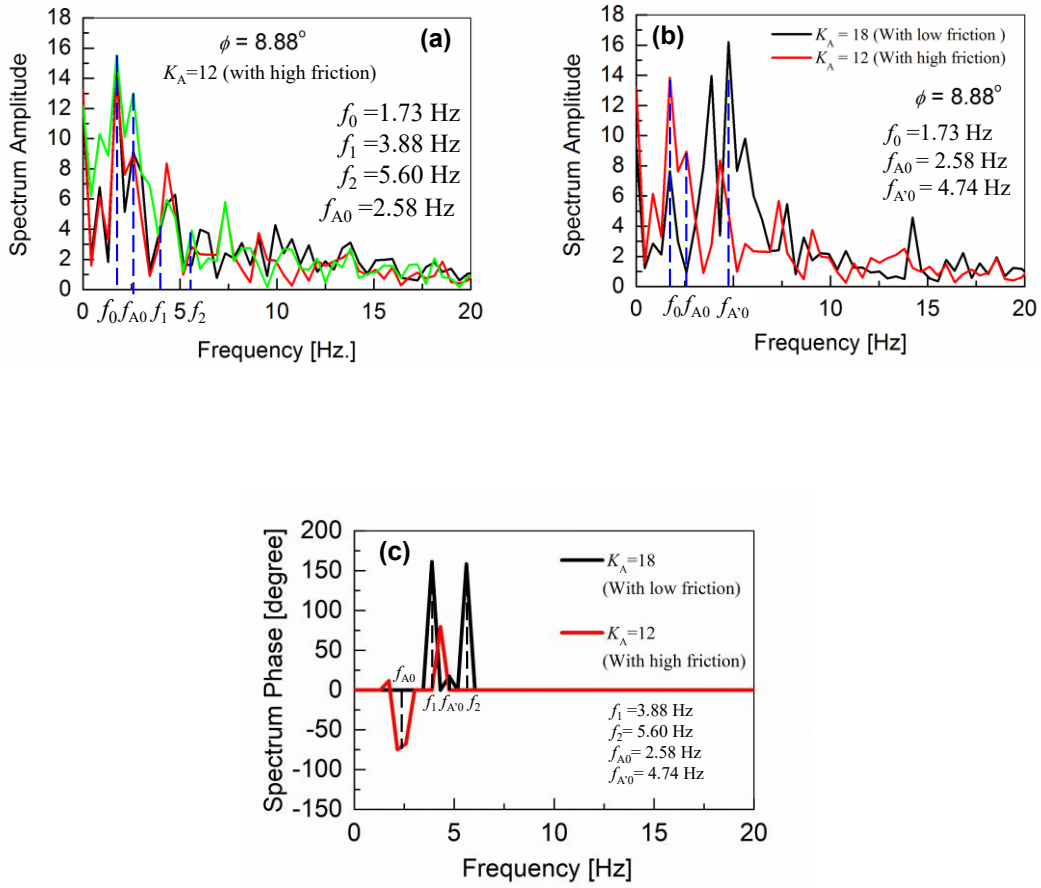

Fig. 5.13. (a) Amplitude plot, which shows the Fourier analysis of the angular-pitch velocity data when the robot is allowed to walk with higher feet friction and reduced value of K_A = 12 on a surface of ϕ = 8.88° inclination. (b) Comparison of amplitude plots, which demonstrates the shift in the additional frequency due to the feedback control from $f_{A'0}$=4.74 Hz to f_{A0}=2.58 Hz, when lowering K_A from 18 to 12, as becomes possible by the increased feet friction. (c) Phase plot, which confirms the frequency-peak shift to a lower value, due to lowering of the feedback gain K_A at higher surface friction. A tolerance value of 33% of the absolute maximum in the amplitude spectrum is used for the phase-plot calculation.

this section further experiments on an inclined surface with higher surface friction are described. The robot feet are attached with rubber soles. The experiments are performed at ϕ = 8.88°. The results with K_A=12 are shown in Fig. 5.13(a). In the case of low surface-friction (see Fig. 5.12(d)), the frequency f_{A0}=2.58 Hz is not observable, but shifted to $f_{A'0}$=4.74 Hz due to the increased value of K_A=18 to make the robot-posture stable. Though the robot was able to walk on the surface stably only with K_A=18 for the low friction surface, the robot can now walk stably with K_A=12 in the case of increased friction. In Fig. 5.13(b), the two results for different friction conditions are compared. The frequency f_0 becomes dominant and the f_{A0}=2.58Hz reappears for the high friction case. The spectrum-

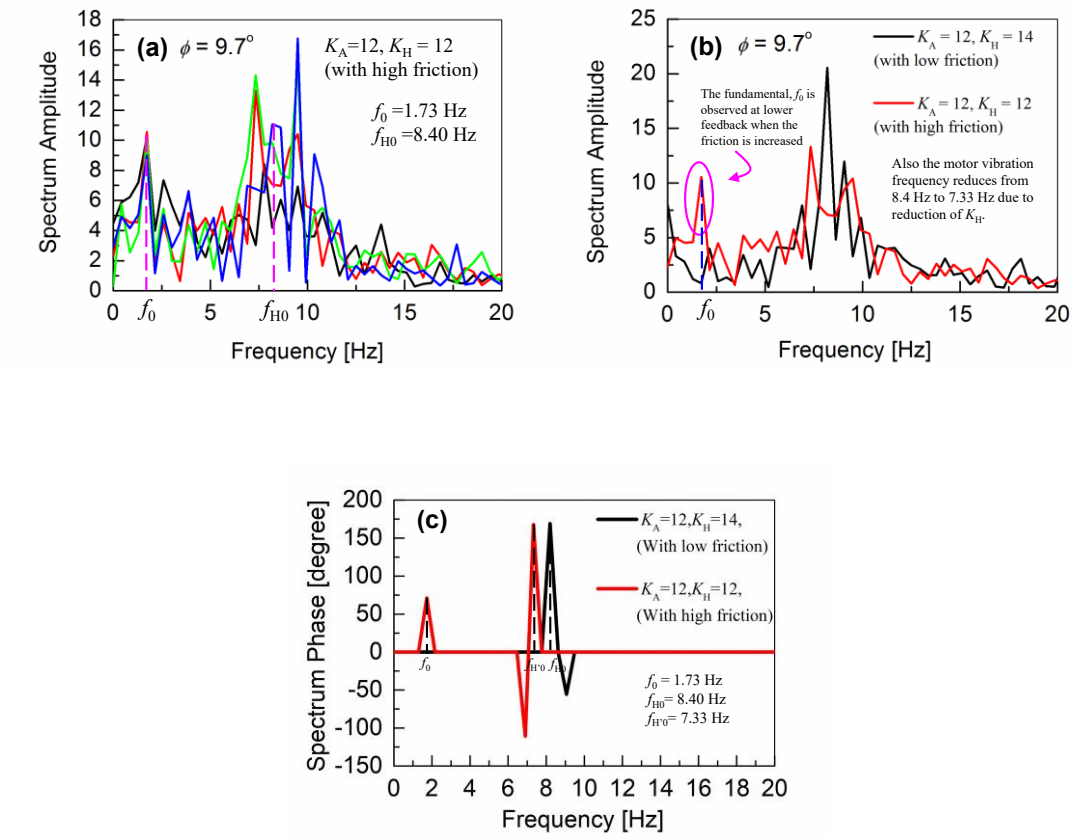

Fig. 5.14. (a) shows that robot can walk on a surface of $\phi = 9.7^o$ inclination with K_H =12, when the robot-feet friction is increased. (b) illustrates two important features, which result from the increased-friction-enabled K_H lowering: First, lowering of the frequency, induced by the additional hip-pitch motor control, from 8.40 Hz to 7.33 Hz. Second, reappearance of the peak at fundamental walking frequency f_0 = 1.73 Hz. (c) Corresponding phase plot, which supports the appearance of the peak at f_0 and the lowering of K_H. A tolerance value of 33% of the absolute maximum in the amplitude spectrum is used for the phase-plot calculation.

amplitude plot is supported by the corresponding phase plot Fig. 5.13(c), which shows shifting of the frequency peaks to lower values, due to lowering of the feedback gain K_A at higher surface friction.

Similar measurement results for $\phi = 9.7^o$, with increased friction, are shown in Fig. 5.14(a). The comparison with the low-friction results, where the robot needed a higher K_H value of 14 for stable walking, is given in Fig. 5.14(b). With increasing the surface friction, two important improvements are clearly observed in the gait-pattern. First, a stable walking for the robot was achieved with a lower K_H value of 12, having a peak at a lower frequency of 7.33 Hz (compared to 8.40 Hz at K_H = 14 for the lower friction case). Second, the

reappearance of the fundamental walking frequency f_0 is confirmed, as highlighted by the encircling in the graph, which is also supported by calculating the phase plot of the angular-pitch velocity, as shown in Fig. 5.14(c). This phase plot further verifies, that a frequency peak appears at f_0 in addition to the lowering of the contributing frequency from 8.40 Hz to 7.33 Hz, thus supporting the results obtained from the spectrum amplitude plot (see Fig. 5.14(b)). Therefore, the high-frequency vibration, observed around 8.40 Hz, is drastically reduced in magnitude and frequency, leading to a more stable gait pattern of the robot.

5.5 Model Development for Robot Balancing

5.5.1 Inverted Pendulum Model (IPM) for Robot Walking

For modeling the walking dynamics of the humanoid robot, a basic inverted pendulum in polar coordinates is considered, as shown in Fig. 5.15, which can be written as [57,102]

$$ml^2 \frac{d^2\theta(t)}{dt^2} - mgl \sin\theta(t) = 0 \tag{5.6}$$

where θ, m, l and g are angle of pitch rotation of the robot torso in the sagittal plane, robot mass, distance of robot's COM from the ankle-pitch motor and acceleration due to gravity, respectively, as also indicated in Fig. 5.15. The physical parameters of the robot are described before in Table I. The first derivative of $\theta(t)$ with respect to time is the angular-pitch velocity, measured in our experiments (see Fig. 5.6 and Fig. 5.7). Under the condition

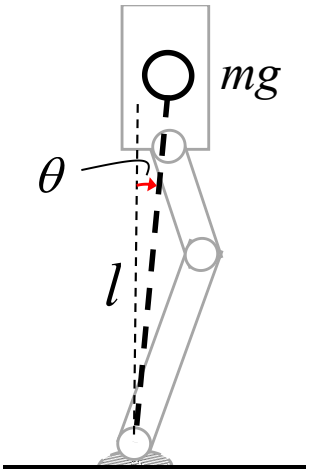

Fig. 5.15. IPM to explain the robot walking dynamics. The parameters θ, m, l and g are angle of robot-torso rotation in the sagittal plane, robot mass, robot-center-of-mass distance from the ankle-pitch motor and acceleration due to gravity, respectively.

of small $\theta(t)$, the solution of (5.6) becomes sinusoidal and the angular-pitch velocity can be written as

$$\omega(t) = a\cos 2\pi f_n t \tag{5.7}$$

Let a and f_n be the initial angular-pitch velocity and the natural frequency of the inverted pendulum, respectively, where f_n given by [102]

$$f_n = \frac{1}{2\pi}\sqrt{\frac{g}{l}} = 0.9 \text{ Hz} \tag{5.8}$$

Thus, the ideal walking motion of a humanoid robot can be modeled as the periodic motion of the inverted pendulum. In that case, one gait cycle can be divided into two half-cycles, where one half cycle is due to the left-leg movement and the other is due to the right-leg movement. Now, in each half cycle there are two motion phases– one Single Support Phase (SSP) and one Double Support Phase (DSP). The SSP of the left and the right leg can be treated identically. This is quite reasonable, because only frequency f_0=1.73 Hz is observed in the gait pattern. During the DSP motion, only the active-leg exchange happens, and thus the gait pattern is characterized nearly exclusively by SSP in the frequency-domain analysis. Therefore, based on the experimental observation and the outlined theoretical justification, we can conclude that the fundamental walking frequency f_0 of the robot's gait pattern should be twice of the natural frequency f_n of the IPM, given by (5.8). The theoretically calculated f_0 of 1.8 Hz is indeed close to the experimentally extracted value of 1.73 Hz.

Under an ideal walking condition, the reference angular-pitch velocity ω_{ref} is thus given by a single frequency f_0 with amplitude a.

$$\omega_{ref}(t) = a\cos 2\pi f_0 t \tag{5.9}$$

Consequently, only one frequency peak is expected at the f_0 =1.73 Hz in the Fourier-transformation of the angular-pitch velocity for ϕ=0, i.e., for an uninclined surface. Now, the output of the modified control system with gyro-sensor feedback (see Fig. 5.4(b)), in response to a sinusoidal input (5.9) of frequency f_0 =1.73 Hz, is then given by

$$\omega_0(s) = \frac{(1 - sK_A S_{GY})K}{Js^2 + B_f s + K} \times \frac{s}{s^2 + (2\pi f_0)^2} \tag{5.10}$$

where the transfer function of the system is given by (5.5). In the time domain, the output angular-pitch velocity can be obtained by an Inverse-Laplace Transform [92] of (5.10) as

$$\omega_0(t) = a_0 \cos(2\pi f_0 t) + b_0 e^{-\frac{B_f}{J}t} \cos(2\pi f_{A0} t) \tag{5.11}$$

where the frequency f_{A0} is the damped natural frequency of the motor-control system for the ankle-pitch motor. The two amplitudes a_0, b_0 can be written as [102]

$$f_{A0} = \sqrt{\frac{K}{J}\left(1 - \frac{{B_f}^2}{JK}\right)} = \sqrt{\frac{K}{J}\left(1 - \frac{(B - K_A S_{GY})^2}{JK}\right)} \tag{5.12}$$

$$a_0 = \frac{a}{\sqrt{(K - J(2\pi f_0)^2)^2 + (2(B - K_A S_{GY})\pi f_0)^2}} \tag{5.13}$$

$$b_0 = \sqrt{\left[\frac{B_f}{4\pi J f_0}\omega_0(t)\Big|_{t=0} + \frac{1}{2\pi f_0}\frac{d\omega_0(t)}{dt}\Big|_{t=0}\right]^2 + \omega_0(t)\Big|_{t=0}} \tag{5.14}$$

Thus, the measured output for the angular-pitch velocity $\omega_0(t)$ is expected to show fundamental frequency peaks at two frequencies of f_0 and f_{A0} in the corresponding Fourier transform. From (5.12) it can be seen, that as the feedback gain K_A is increased, the frequency f_{A0} also increases. This is confirmed by the experimental observations as shown in Figs. 5.8(c-1), 5.8(c-2) and 5.8(d).

5.5.2 Inverted Pendulum Model for Robot Walking

The analysis, carried out in last subsection, assumed the control system to be linear. This allows the use of transfer-function modeling. The time-domain output (see (5.11)) is obtained to explain the experimentally-measured results. The model (see (5.11)), discussed in last subsection, explains the output of a second-order system (see (5.5)) in response to a sinusoidal input of frequency 1.73 Hz. The output consists of the input frequency of 1.73 Hz and the damped natural frequency f_{A0}.

Here, the model (see (5.10)) is extended to include the nonlinearity of the robot dynamics, which is induced in the inverted pendulum by the surface inclination ϕ. First the origin of higher-order harmonics is explained and then the inclusion of the harmonics (nonlinearity) into the model (see (5.11)) is discussed. For understanding the nonlinearity, time-domain analysis of a nonlinear pendulum is considered. For an inclined surface, (5.6) changes to [97,102]

$$ml^2 \frac{d^2\theta(t)}{dt^2} + mgl\sin(\theta(t)+\phi) = 0 \tag{5.15}$$

where ϕ is the surface inclination. If we expand the sinusoidal term following the basic trigonometric identity [104], we get

$$ml^2 \frac{d^2\theta(t)}{dt^2} + mgl\left(\cos\phi\ \sin\theta(t) + \sin\phi\ \cos\theta(t)\right) = 0 \tag{5.16}$$

This result can be rewritten by series expansions of $\sin\theta(t)$ and $\cos\theta(t)$ into the form

$$ml^2 \frac{d^2\theta(t)}{dt^2} + mgl\cos\phi\left(\theta(t) - \frac{\theta^3(t)}{6} + \frac{\theta^5(t)}{120} - \ldots\right) + mgl\sin\phi\left(1 - \frac{\theta^2(t)}{2} + \frac{\theta^4(t)}{24} - \ldots\right) = 0 \tag{5.17}$$

The solution of (5.17) with a sinusoidal input of the fundamental walking frequency f_0 (see (5.9)) of the robot's gait pattern is given by [105-113]

$$\omega_{\text{meas}}(t) = A_0 + a_0\cos(2\pi f_0 t) + a_1\cos(2\pi f_1 t) + a_2\cos(6\pi f_2 t) \tag{5.18}$$

where a_0 is the amplitude of the fundamental walking-frequency component, given by (5.13). The amplitudes a_1 and a_2 of the harmonics are functions of the surface inclination ϕ, as shown in (5.19) and (5.20)

$$a_1 = \frac{g\cos\phi}{6l}a_0 \tag{5.19}$$

$$a_2 = \frac{g\sin\phi}{2l}a_0 \tag{5.20}$$

In both time-domain (Fig. 5.6 and Fig. 5.7) and frequency-domain (Fig. 5.8 and Fig. 5. 9), it is experimentally observed that the oscillation amplitudes become larger with an increase in surface inclination ϕ. From above investigation, the theoretical investigation confirms the experimental findings. The surface inclination ϕ has two main effects on the measured angular-pitch velocity of the robot. Firstly, there is an increase in nonlinearity, which causes the appearance of higher-order harmonics. Secondly, the oscillation amplitudes increase for larger surface inclination. From the results it is confirmed, that the harmonic coefficients a_1 and a_2 give dominating contributions of the robot motion under high ϕ values. Equation (5.18) explains the trend of the measured angular-pitch velocity for surface inclinations $\phi \leq 5.55^{\circ}$ (see Fig. 5.8(b-1) and Fig. 5.8(b-2)) and the origin of the

nonlinearity due to the higher-order harmonics of the fundamental frequency of 1.73 Hz. It is now important to incorporate these higher-order harmonics into the previously discussed model (see (5.11)).

When the feedback loop of K_A is applied for $\phi \geq 5.55^o$, an additional frequency peak is observed (see Figs. 5.8(c-1), 5.8(c-2) and 5.8(d)). The origin of the peak strength at this additional frequency f_{A0} is explained by (5.11). The theoretical expression for f_{A0} is given by (5.12).

The experimentally measured results can be explained by calculating the output of the second-order system (see 5.5) in response to an algebraic sum of sinusoids of fundamental frequency and its higher harmonics.

$$\omega_{meas}(s) = \frac{(1 - sK_A S_{GY})K}{Js^2 + B_f s + K} \times \left(\frac{s}{s^2 + (2\pi f_0)^2} + \frac{s}{s^2 + (2\pi f_1)^2} + \frac{s}{s^2 + (2\pi f_2)^2} \right) \quad (5.21)$$

The measured angular-pitch velocity can be analyzed with the following equation, obtained by inverse-Laplace transform of the (5.21).

$$\omega_{meas}(t) = A_0 + \sum_{n=0}^{2} a_n \cos 2\pi f_n t + B_0 + b_0 e^{-\frac{B_f}{J}t} \cos 2\pi f_{A0} t \quad (5.22)$$

where $\omega_{meas}(t)$ is the measured angular-pitch velocity when the gyro-sensor feedback is applied for motor control. As the surface inclination ϕ is increased, the feedback strength K_A has to be also increased to keep the robot posture stable. However, with increasing K_A the vibration of the robot body also increases. The frequency-domain analysis of the angular-pitch velocity is dominated by the K_A-induced damped natural frequency f_{A0}, given in (5.12), and the gravity-induced harmonics of the fundamental walking frequency f_0, given in (5.18). Nevertheless, to keep a sufficiently stable robot walking, the amplitude of f_0 must dominate over the other frequencies.

5.6 Conclusion

In this chapter the origin of the robot-posture instability is investigated, which occurs during walking on inclined surfaces. It was found, that the higher-order harmonics are induced by the distorting effects of the gravity force. The contribution of the harmonics increases when the surface inclination increases, resulting in the robot falling down. This is an original way to explain the instability of the robot walking frequency domain. To

protect the robot from falling down, a gyros sensor based feedback control has been implemented in the motor-control system of the robot. It is explained in detail that in order to maintain a stable walking, the fundamental walking frequency must be the only peak in the frequency domain. The frequency components due to the feedback-control must be kept lower than the fundamental walking frequency, so that a clear fundamental walking frequency is still observable. However, it can easily happen, that the necessary feedback control becomes too large for maintaining the fundamental robot posture on a largely inclined surface. Thus, strongly enhanced vibration of the robot body is observed, which causes instabilities to the robot-walking under large surface inclination becomes. For solving this stability problem, it was further demonstrated, that a larger friction between the robot feet and the surface provides an efficient way to improve the robot walking allowing to reduce the feedback gain. Reducing the feedback gain, causes reduction in the oscillations at higher frequencies. In summary, the frequency-domain analysis of the robot's periodic gait pattern tool for the understanding the instabilities in the robot-walking and for deriving suitable methods of gait-pattern stabilization under external disturbances.

Chapter 6: Conclusions and Future works

Light-weight humanoid robots have potential application for information acquisition inside a disaster hit environment where the load-bearing capabilities of the mechanical structures are reduced. In that case the walking stability of the robot is of great importance in such environments. The dissertation studies the walking control for lightweight robot on inclined surface. Three novel contributions of the dissertation are summarized as follows.

6.1 Novelty and Conclusions of the Dissertation

The most important new scientific results of the present dissertation can be summarized as follows:

6.1.1 Static stability of humanoid robot on inclined surface

The static stability of the robot (in a Single Support Phase) is investigated on an inclined surface, where the inclination is varied from 0 to 10.2 degrees. A force-sensor based position-control system is proposed and thereafter implemented in the robot hardware. This allows the robot to stand stably on one foot (Single Support Phase of walking) up to an inclined surface of 7.68 degrees. Beyond 7.68 degrees, the robot needs higher torque to stabilize its posture. In that case a gyro-sensor based position control for the hip servomotor is integrated. The position of the hip-motor is controlled by the angular-pitch velocity of the robot body sensed by the gyro sensor. This allows the robot to stand stable (in Single Support Phase) up to an inclined surface of 10.2 degrees.

6.1.2 Potential application of gyro sensor

An electromechanical model of the gyro sensor is experimentally verified from the dynamic characteristics of analog gyro sensor KRG-4. The KRG-4 gyro sensor is used in the experiments for the stability of the robot. The gyro sensor model is used to model the push recovery strategy for the robot on a plane surface. The model was experimentally verified by the push-recovery experiments.

6.1.3 Vibration control while walking on an inclined surface

At the end the the walking stability of the robot is investigated on an inclined surface and with the proposed gyro sensor based control system the robot can walk upto ana inclined surface of 10.2 degrees. In order to stabilize the robot walking on an inclined

surface, a gyro-sensor based feedback control systems is proposed. The experimental results shows that as the surface inclination is increased higher harmonics of the fundamental walking frequency and damped natural frequency of the control system effects the robot walking. This increases the vibration in the robot, thus making the robot walking unstable. An optimization of the controller gain is implemented based on the tradeoff between the surface friction and the vibration. Therefore adjusting the controller gain, the vibration is reduced.

6.2 Future Works

Humanoid robots are one of the most complex intelligent machine human beings have ever worked upon. There are many open research problems which are yet to be solved. This thesis gives rise to two interesting research problems in the field of 'light-weight' humanoid robot.

Surface friction is a very important physical phenomena observed in case of robot-walking on an inclined surface. Lower surface friction will most likely limit the critical surface inclination ϕ_{cr} for a given reference robot-posture. Therefore it is very important to incorporate the effect of surface friction into the IPM to study the dynamics of the robot theoretically. The problem faced during the surface friction is, it is very difficult to observe the effect of surface friction on the robot walking during the experiments. So, development of experimental setup to measure the effect of surface friction over robot-walking dynamics can be an envisaged future work.

Another possible future work can be the theoretical analysis of effect of mechanical stiffness of the robot joints (motor control system) on the vibration of the robot. The feedback gains of the gyro-sensor based control system effect the equivalent stiffness in the motor-load transmission system of the ankle-pitch motor and the hip-pitch motor. The study of vibration in a motor-load transmission system is widely studied. This thesis suggests that, the study can be taken to one step ahead to the effect of vibration on the robot walking on a given surface.

References

[1] Eaton, R.; Katupitiya, J.; Siew, K. W.; B. Howarth, Autonomous farming: Modeling and control of agricultural machinery in a unified framework, In Proceedings of 15th International Conference on Mechatronics and Machine Vision Practice, Auckland, New Zealand, 2008, vol. 1, pp. 499–504.

[2] Cheein, F. A. A.; Carelli, R. Agricultural robotics: Unmanned robotic service units in agricultural tasks. *IEEE Ind. Electron. Mag.* **2013**, *7*, 48-581.

[3] Michael, N.; Fink, J.; Kumar, V. Cooperative manipulation and transportation with aerial robots. *Auton. Robot.* **2011**, 30, 73–86.

[4] Burri, M.; Nikolic, J.; Hürzeler, C.; Caprari, G.; Siegwart, R. Aerial service robots for visual inspection of thermal power plant boiler systems. In Proceedings of 2nd International Conference on Applied Robotics for the Power Industry (CARPI), Zurich, Switzerland, 2012, pp.70-75.

[5] Casper, J.; Murphy, R. R. Human-robot interactions during the robot-assisted urban search and rescue response at the World Trade Center. *IEEE Trans. Syst., Man., Cybern. B* **2003**, 33, 138-153.

[6] Holt, M.; Campbell, R.J.; Nikitin, M.B. Fukushima Nuclear Disaster; Congressional Research Service: Washington, DC, USA, 2012.

[7] Yoshida, T.; Nagatani, K.; Tadokoro, S.; Nishimura, T.; Koyanagi, E. Improvements to the Rescue Robot Quince Toward Future Indoor Surveillance Missions in the Fukushima Daiichi Nuclear Power Plant, In *Field and Service Robotics*. Springer Tracts in Advanced Robotics; Yoshida K., Tadokoro S. Eds.; Springer, Berlin, Heidelberg, Germany, 2014; pp. 19-32.

[8] Taoyaka Society - a flexible, enduring, and peaceful society of coexistence. Available Online:https://taoyaka.hiroshima-u.ac.jp/english/about-us/program-features.html#:~:text=Onsite%20reverse%20innovation%20is%20comprised,addressing%20individually%20the%20various%20issues.

[9] I. Asimov, *Runaround*, 1942.

[10] Kajita, S.; Hirukawa, H.; Harada, K.; Yokoi, K. In *Introduction to Humanoid Robotics*, Springer-Verlag, Berlin Heidelberg, 2014; pp. 45-65, 69-97.

[11] Choreonoid Official Site. Available Online: https://choreonoid.org/en/

[12] DARPA Robotics Challenge (DRC) (Archived). Available Online : https://www.darpa.mil/program/darpa-robotics-challenge

[13] Okada, S and Takai, N. Classifications of Structural Types and Damage Patterns of Building for Earthquake Field Investigation. *J. Struct. Constr. Eng., AIJ*, 1999, No. 524, 65-72.

[14] KHR-3HV Humanoid Robot, Kondo Kagaku Co. Ltd. 2019. Available Online: https://kondo-robot.com/product/03110e

[15] Wang, S; Chaovalitwongse, W; Babuska, R. Machine Learning Algorithms in Bipedal Robot Control. *IEEE Trans. Syst., Man., Cybern. C* 2012, 5, 728-743.

[16] Dutta, S; Miura-Mattausch, M; Ochi, Y; Yorino, N; Mattausch HJ. Gyro-Sensor-Based Vibration Control for Dynamic Humanoid-Robot Walking on Inclined Surface. *Sensors*, **2020,** 20(24), 7139.

[17] Dutta, S; Maiti, TK; Miura-Mattausch, M; Ochi, Y; Yorino, N; Mattausch HJ. Analysis of Sensor-Based Real-Time Balancing of Humanoid Robots on Inclined Surfaces. *IEEE Access*, **2020,** 8, 212327-212338.

[18] Dutta, S; Maiti, TK; Ochi, Y; Miura-Mattausch, M; Bhattacharya, S; Navarro, D; Yorino, N; Mattausch HJ. Self-controlled walking robot with gyro sensor network for stable movement on non-smooth surfaces. In Proceedings of 2018 IEEE International Conference on Simulation, Modeling, and Programming for Autonomous Robots (SIMPAR), Brisbane, Australia, 2018, pp. 137-143.

[19] Dutta, S; Maiti, TK; Ochi, Y; Miura-Mattausch, M; Bhattacharya, S; Yorino, N; Mattausch HJ. Stability Analysis of Humanoid Robots with Gyro Sensors Subjected to External Push Forces. In Proceedings of 2nd International Symposium on Devices, Circuits and Systems (ISDCS), Hiroshima , Japan, 2019, pp. 1-4.

[20] Stephens, B. Humanoid push recovery. In Proceedings of 7th IEEE-RAS International Conference on Humanoid Robots. Pittsburgh, PA, USA, 2007, pp.589-595.

[21] A. Hornung, K. M. Wurm, and M. Bennewitz, "Humanoid robot localization in complex indoor environments," *IEEE/RSJ Int. Conf. on Intelligent Robots and Systems (IROS)*, Taiwan, 2010, pp.1690-1695.

[22] S. Kuindersma, R. Deits, M. Fallon, A. Valenzuela, H. Dai, F. Permenter, T. Koolen, P. Marion, and R. Tedrake, "Optimization-based locomotion planning, estimation, and control design for the atlas humanoid robot," *Autonomous Robots*, vol. 40, no. 3, pp.429-455, Mar. 2016.

[23] H. Dai and R. Tedrake, "Planning robust walking motion on uneven terrain via convex optimization," *IEEE-RAS 16th International Conference on Humanoid Robots (Humanoids)*, Mexico, 2016, pp.579-586.

[24] A. Hereid, E. A. Cousineau, C. M. Hubicki, A. D. Ames, "3D dynamic walking with underactuated humanoid robots: A direct collocation framework for optimizing hybrid zero dynamics," *IEEE Int. Conf. on Robotics and Automation (ICRA)*, Sweden, 2016, pp.1447–1454.

[25] M. Morisawa, S. Kajita, F. Kanehiro, K. Kaneko, K. Miura, and K. Yokoi, "Balance control based on Capture Point error compensation for biped walking on uneven terrain, " in *Proc. IEEE Int. Conf. Humanoid Robots (Humanoids).* Osaka, Japan, 2012, pp. 734-740.

[26] CM Chew, J. Pratt, G. Pratt, "Blind walking of a planer bipedal robot on sloped terrain," in *Proc. IEEE Int. Conf. on Robotics and Automation*, Kyongju, Korea, 1999, pp. 381-386.

[27] Y. Hidaka, K. Nishizawa and D. N. Nenchev, "Dynamic Stepping on Unknown Obstacles With Upper-Body Compliance and Angular Momentum Damping From the Reaction Null-Space," in *Proc. IEEE Intl. Conf. on Robotics and Automation*, Montreal, Canada, 2019, pp. 5273-5279.

[28] Q. Nguyen, A. Agrawal, W. Martin, H. Geyer and K. Sreenath, "Dynamic bipedal locomotion over stochastic discrete terrain," *The International Journal of Robotics Research*, vol. 37, no.13-14, pp. 1537-1553, Dec. 2018.

[29] G. Nelson, A. Saunders and R. Playter, "The PETMAN and Atlas Robotsat Boston Dynamics," *Humanoid Robotics: A Reference*. Berlin: Springer, pp. 169-186, 2019.

[30] Q. Li, Z. Yu, X. Chen, Q. Zhou, W. Zhang, L. Meng and Q. Huang, "Contact Force/Torque Control Based on Viscoelastic Model for Static Bipedal Walking on Indefinite Uneven Terrain," *IEEE Trans. On Automation Science and Engineering*, vol. 16, no. 4, pp. 1627-1639, Oct. 2019.

[31] Felix Segulla and Daniel Rixen, "A Force-Control Scheme for Biped Robots to Walk over Uneven Terrain Including Partial Footholds," *International Journal of Advanced Robotic Systems*, vol. 17, no. 1, pp. 1-14, Jan. 2020.

[32] M. Favre, B. Goodwine and J. P. Schmiedeler, "Terrain-blind walking of planer underactuated bipeds via velocity decomposition-enhanced control," *The International Journal of Robotics Research,* vol. 38, no. 10-11, pp. 1307-1323, Aug. 2019.

[33] D. Wahrmann, A.C. Hilderbrandt, T. Bates et al., "Vision-Based 3D Modeling of Unknown Dynamic Environments for Real-Time Humanoid Navigation," *International Journal of Humanoid Robotics*, vol. 16, no. 1, pp. 1-34, 2019.

[34] A.C. Hilderbrandt, R. Wittmann, F. Sygulla et al., "Versatile and robust bipedal walking in unknown environments: real-time collision avoidance and disturbance rejection," *Autonomous Robots*, vol. 43, pp. 1957-1976, 2019.

[35] S. Kajita, F. Kanehiro, K. Kaneko, K. Yokoi, and H. Hirukawa, "The 3D Linear Inverted Pendulum Mode: A simple modeling for a biped walking pattern generation," *IEEE/RSJ International Conference on Intelligent Robots and Systems (IROS)*, Maui, USA, 2001, pp. 239-246.

[36] T. McGeer, "Passive Dynamic Walking," *The International Journal of Robotics Research*, vol. 9, no. 2, pp. 62-82, Apr. 1990.

[37] S. H. Collins, M. Wisse, and A. Ruina, "A Three-Dimensional Passive-Dynamic Walking Robot with Two Legs and Knees," *The International Journal of Robotics Research*, vol. 20, no. 7, pp. 607-615, Jul. 2001.

[38] J. Chestnutt, M. Lau, G. Cheung, J. Kuffner, J. Hodgins, and T. Kanade, "Footstep Planning for the Honda ASIMO Humanoid," *IEEE Int. Conf. on Robotics and Automation*, Barcelona, Spain, 2005, pp.629-634.

[39] M. Vukobratovic and B. Borovac, "Zero-Moment Point-Thirty Five Years of Its Life," *International Journal of Humanoid Robotics*, vol. 1, no. 1, pp.157-173, 2004.

[40] ASIMO Technical Information, Honda Motor Co., Ltd., 2007.

[41] K. Kaneko, F. Kanehiro, M. Morisawa, T. Tsuji, K. Miura, S. Nakaoka, S. Kajita, K. Yokoi, "Hardware improvement of cybernetic human HRP-4C for entertainment use," *IEEE/RSJ International Conference on Intelligent Robots and Systems*, CA, USA, 2011, pp. 4392–4399.

[42] Development of a Humanoid Robot Prototype, HRP-5P, Capable of Heavy Labor, National Institute of Advanced Industrial Science and Technology (AIST), Nov. 2018.

[43] K. C. Lau et al., "A flexible surgical robotic systems for removal of early-stage gastrointestinal cancers by endoscopic submucosal dissection," *IEEE Transactions on Industrial Informatics,* vol. 12, no. 6, pp. 2365-2374, Dec. 2016.

[44] Z. Zhang et al., "Mutual-Collision-Avoidance Scheme Synthesized by Neural Networks for Dual Redundant Robot Manipulators Executing Cooperative Tasks," *IEEE Transactions on Neural Networks and Learning Systems*, to be published. DOI: 10.1109/TNNLS.2020.2980038.

[45] J.-G. Juang. "Locomotion control using environment information inputs," *Proceedings of International Conference on Information Intelligence and Systems,* Bethesda, MD, USA, 1999, pp. 196-201.

[46] J. P. Ferreira, M. Crisostomo, A. P. Coimbra, and B. Ribeiro, "Simulation control of a biped biped robot with support vector regression," *Proceedings of IEEE International Symposium on Intelligent Signal Processing,* Xiamen, China, 2007, pp. 1-6.

[47] X Da, R Hartley, JW Grizzle, "Supervised Learning for stabilizing underactuated bipedal robot locomotion, with outdoor experiments on the wave field," *Proceedings of IEEE International Conference on Robotics and Automation (ICRA)*, Singapore, 2017, pp. 3476-3483.

[48] W. Salatian, K. Y. Yi and Y. F. Zheng, "Reinforcement learning for a biped robot to climb sloping surfaces," *Journal of Robotic Systems*, 14(4): 283-296, 1997.

[49] Gen Endo et al., "Learning CPG-based biped locomotion with a policy gradient method: Application to a Humanoid Robot," *The International Journal of Robotics Research*, vol. 27, no. 2, pp. 213-228, Feb. 2008.

[50] S. Kajita and K. Tani, "Study of dynamic biped locomotion on rugged terrain-derivation and application of the linear inverted pendulum mode," *Proceedings of IEEE International Conference on Robotics and Automation (ICRA)*, Sacramento, CA, USA, 1991, pp. 1405-1411.

[51] S. G. Tzafestas, T. E, Krikochoritis and C. S. Tzafestas, "Robust sliding-mode control of nine-link biped robot walking," *Journal of Intelligent Robotics and Systems*, vol. 20, no. 2-4, pp. 375-402, Sept. 1997.

[52] H. Kooij et al., "An alternative approach to synthesizing bipedal walking," *Biological Cybernetics*, vol. 88, no. 1, pp. 46-59, Apr. 2003.

[53] Toricelli D. et al. (2020) Benchmarking Human Likeness of Bipedal Robot Locomotion: State of Art and Future Trends. In: Bonsignorio F.,Messina E., del Pobil A., Hallam J. (eds) Metrics of Sensory Motor Coordination and Integration in Robots and Animals. Cognitive Systems Monograph, vol.36. Springer, Cham.

[54] K. Tamura and A. Kawamura, "Robust and high-mobility walking control for uneven terrain without zero-moment-point feedback," in *Proc. IEEE Int. Conf. Ind. Tech. (ICIT).* Toronto, ON, Canada, 2017, pp. 866-871.

[55] SJ Yi, BT Zhang, D. D Lee, "Online Learning of Uneven Terrain for Humanoid Bipedal Walking," in *Proc. AAAI Conf. on Artificial Intelligence (AAAI-10)*, Atlanta, Georgia, USA, 2010, pp. 1639-1644.

[56] H. Hemami and C. L. Golliday, "The inverted pendulum and biped stability," *Mathematical Biosciences*, vol. 34, no. 1-2, pp. 95-110, Nov. 1977.

[57] H. Hemami, F.C. Weimer, and S. H. Koozekanani, "Some aspects of the inverted pendulum problem for modelling of locomotion systems," *IEEE Transaction on Automatic Control*, vol.18, no. 5, pp. 658-661, Dec. 1973.

[58] R. B. McGhee and M. B Kuhner, "On the dynamic stability of legged locomotion systems," *Proc. 3rd International Symposium on External Control of Human Extremities, Dubrovnik, Yugoslovia,* 1969, pp. 431-442.

[59] M. Vukobratovic, A. Frank and D. Juricic, "On the stability of biped locomotion," *IEEE Transactions on Biomedical Engineering*, vol. 17, no. 1, pp. 25-36, Jan. 1970.

[60] S. Kajita and K. Tani, "Experimental study of biped dynamic walking," *IEEE Control Systems*, vol. 16, no.1, pp. 13-19, Feb. 1996.

[61] R. Murphy, Introduction to AI robotics, MIT press, 2000.

[62] T. K. Maiti, L. Chen, M. Miura-Mattausch, S. K. Koul, and H. J. Mattausch, "Physics Based System Simulation for Robot Electro-Mechanical Control Design," in *IEEE Electron Dev. Tech. Manuf. Conf.*, pp.259–261, Feb. 2017, Japan.

[63] T. K. Maiti, Y. Ochi, D. Navarro, M. Miura-Mattausch, and H. J. Mattausch, "Walking robot movement on non-smooth surface controlled by pressure sensor," *Adv. Mat. Lett.* 2018.

[64] H.Hemami and P. Camana, "Nonlinear feedback in simple locomotion systems," *IEEE Transactions on Automatic Control*, vol. 21, no. 6, pp.855-860, Dec. 1976.

[65] A. Hofmann, "Robust execution of bipedal walking tasks from biomechanical principles," Ph.D. dissertation, Massachusetts Institute of Technology, Jan. 2006.

[66] J. Pratt, J. Carff, S. Drakunov, and A. Goswami, "Capture point : A step towards humanoid push recovery," *6th IEEE-RAS International Conference on Humanoid Robots*, pp. 200-207, Dec. 2006.

[67] Ayyappa, E. Normal human locomotion, part 1: Basic concepts and terminology. *J. Prosthet. Orthot.* **1997**, *9*, 10-17.

[68] Ayyappa, E. Normal human locomotion, part 2: Motion, ground-reaction force and muscle activity. *JPO: J. Prosthet. Orthot.* **1997**, *9*, 49-57.

[69] Schneider, E.; Chao, E. Y. Fourier analysis of ground reaction forces in normals and patients with knee joint disease. *J. Biomech.* **1983***, 16*, 591-601.

[70] Chao, E. Y.; Laughman, R. K.; Schneider, E.; Stauffer, R. N. Normative data of knee joint motion and ground reaction forces in adult level walking. *J. Biomech.* **1983**, *16*, 219-233.

[71] Giakas, G.; Baltzopoulos, V. Time and frequency domain analysis of ground reaction forces during walking: an investigation of variability and symmetry. *Gait. Posture.* **1997**, *5*, 189-197.

[72] Crowe, A.; Schiereck, P.; De Boer, R. W.; Keessen, W. Characterization of human gait by means of body center of mass oscillations derived from ground reaction forces. *IEEE Trans. Biomed. Eng.* **1995**, *42*, 293-303.

[73] Crowe, A.; Schiereck, P.; de Boer, R.; Keessen, W. Characterization of gait of young adult females by means of body centre of mass oscillations derived from ground reaction forces. *Gait. Posture.* **1993**, *1*, 61-68.

[74] Wurdeman, S. R.; Huisinga, J. M.; Filipi, M.; Stergiou, N. Multiple sclerosis affects the frequency content in the vertical ground reaction forces during walking. *Clin. Biomech.* **2011**, *26*, 207-212.

[75] Tafazzoli, F.; Safabakhsh, R. Model-based human gait recognition using leg and arm movements. *Eng. Appl. Artif. Intel.* **2010**, *23*, 1237-1246.

[76] Suzuki, K.; Imai, H.; Kawamura, Y.; Sankai, Y. Gait control of human and humanoid on irregular terrain considering interaction with environment. In Proceedings of IEEE International Workshop on Robot and Human Interactive Communication, CA, USA, 2003, pp. 277-284.

[77] Bötzel, K.; Olivares, A.; Cunha, J. P.; Sáez, J. M. G.; Weiss, R.; Plate, A. Quantification of gait parameters with inertial sensors and inverse kinematics. *J. Biomech.* **2018**, *72*, 207-214.

[78] Cela, A.; Yebes, J. J.; Arroyo, R.; Bergasa, L. M.; Barea, R.; López, E. Complete Low-Cost Implementation of a Teleoperated Control System for a Humanoid Robot. *Sensors* **2013,** *13,* 1385-1401.

[79] Morimoto, J.; Endo, G.; Nakanishi, J.; Cheng, G. A biologically inspired biped locomotion strategy for humanoid robots: Modulation of sinusoidal patterns by a coupled oscillator model. *IEEE Trans. Robot.* **2008**, *24*, 185-191.

[80] Khan, U. I.; Chen, Z. Natural Oscillation and Optimal Gaits for Humanoid Biped Models. In Proceedings of IEEE-RAS International Conference on Humanoid Robots, Beijing China, 2018, pp. 196-201.

[81] Kajita, S.; Asano, F.; Mitsuharu, M.; Miura, K.; Kaneka, K.; Kanehiro, F.; Kazuhito, Y. Vertical vibration suppression for a position controlled biped robot. In Proceedings of IEEE International Conference on Robotics and Automation (ICRA), Karlsruhe, Germany, 2013, pp. 1629-1634.

[82] Cheng, C.; Chang, J.; Lv, W.; Li, K.; Li, Z; Yuan, C.; Ma, S. Frequency-Temporal Disagreement Adaptation for Robotic Terrain Classification via Vibration in a Dynamic Environment. *Sensors* **2020**, *20*, 6550 (19 Pages).

[83] Liu, H.; Cui, S.; Liu, Y.; Ren, Y.; Sun, Y. Design and Vibration Suppression Control of a Modular Elastic Joint. *Sensors* **2018**, *18*, 1869 (19 Pages).

[84] Kim, J-Y.; Park, I-W.; Oh, J-H. Walking Control Algorithm of Biped Humanoid Robot on Uneven and Inclined Floor. *J. Intel. Robot. Syst.* **2007,** *48*, 457-484.

[85] Vukobratovic, M.; Borovac, B. Zero-Moment Point-Thirty Five Years of Its Life. *Int. J. Humanoid Robot.* **2004**, 1, 157-173.

[86] Joe, H-M.; Oh, J-H. A Robust Balance-Control Framework for the Terrain-Blind Bipedal Walking of a Humanoid Robot on Unknown and Uneven Terrain. *Sensors* **2018**, *18*, 1869 (19 Pages).

[87] T. K. Maiti, L. Chen, H. Zenitani, H. Miyamoto, M. Miura-Mattausch, and H. J. Mattausch, "Compact Electro-Mechanical-Fluidic Model for Actuated Fluid Flow System," *IEEE Journal on Multiscale and Multiphysics Computational Techniques*, vol. 2, pp. 124-133, Jul. 2017.

[88] T. K. Maiti, L. Chen, M. Miura-Mattausch, S. K. Koul, and H. J. Mattausch, "Physics Based System Simulation for Robot Electro-Mechanical Control Design," *IEEE Electro. Dev. Tech. and Manuf. Conf.*, Japan, 2017, pp.259-261.

[89] KHR-3HV Humanoid Robot, Kondo Kagaku Co. Ltd. 2019. Available Online https://kondo-robot.com/product/03067e (accessed on 27.11.2020).

[90] PIC16F690. Available Online: https://www.microchip.com/wwwproducts/en/PIC16F690 (accessed on 27.11.2020)

[91] KHR-3HV Humanoid Robot, Kondo Kagaku Co. Ltd. 2019. Available Online: https://kondo-robot.com/product/03076. (accessed on 26.11.2020).

[92] Ogata, K.; Yang, Y. *Modern control engineering*. Upper Saddle River, NJ: Prentice hall, 2010; pp. 27-29.

[93] Corke, P. *Robotics, vision and control: fundamental algorithms in MATLAB® second, completely revised* (Vol. 118). Springer, 2017; pp. 251-257

[94] Siciliano, B., Sciavicco, L., Villani, L., & Oriolo, G. *Robotics: modelling, planning and control*. Springer Science & Business Media, 2010; pp. 198-209

[95] Scarpino, M. *Motors for makers: a guide to steppers, servos, and other electrical machines*. Que Publishing., 2015; pp.78-85.

[96] Urrea, C.; Kern, J. A new model for analog servo motors. Simulations and experimental results. *Canadian J. Automat. Contr. Intel. Syst.* **2011**, *2*, 29-38.

[97] Wada, T.; Ishikawa, M.; Kitayoshi, R.; Maruta, I.; Sugie, T. Practical modeling and system identification of R/C servo motors. In Proceedings of IEEE Control Applications & Intelligent Control, Russia, 2009, pp. 1378-1383.

[98] Sakai, F.; Kamiya, Y.; Seki, H.; Hikizu, M. Dynamic Characteristics of DC Servo Motor Driven by Conventional Servo Driver-Estimation of Circuit Constants in Conventional Servo Driver. *J. Japan Soc. Precis. Eng.* **2000**, *66*(2), 266-271.

[99] KHR-3HV Humanoid Robot, Kondo Kagaku Co. Ltd. 2019. Available Online: https://kondo-robot.com/product/03003 (accessed on 26.11.2020).

[100] Atmel, "ATmega328P: 8-bit AVR Microcontroller", 2015. Available Online: https://www.microchip.com/wwwproducts/en/ATmega328P (accessed on 29.11.2020)

[101] Ellis, George. *Control System Design Guide*, 4th ed.; Butterworth-Heinemann, Waltham, USA, 2012; pp. 364-366.

[102] Cannon, R. H. *Dynamics of physical systems*. Courier Corporation, USA, 2003; pp. 171-172

[103] Li, Z.; Zhou, C.; Tsagarakis, N.; Caldwell, D. Compliance control for stabilizing the humanoid on the changing slope based on terrain inclination estimation. *Auton. Robot.* **2016**, *40*, 955-971.

[104] Loney, S. L. *Plane trigonometry*, Cambridge University Press, London, 1893; pp. 87-88.

[105] Euler, L. De novo genere oscillationum. *Commentarii academiæ scientiarum Petropolitanæ*, 1750. pp. 128-149.

[106] Euler, L. The Rational Mechanics of Flexible or Elastic Bodies: Introduction to Vol. X and XI. Springer Science & Business Media, 1960. pp. 1638-1788.

[107] Von Helmholtz, H. On the Sensations of Tone as a Physiological Basis for the Theory of Music. 2nd ed.; Longmans, Green, 1885; pp.411-413.

[108] Strutt, J. W., & Rayleigh, B. *The Theory of Sound*. Dover, USA, 1945; pp. 74-84.

[109] Duffing, G. Forced oscillations with variable natural frequency and their technical significance. *Vieweg & Sohn*. 1918.

[110] Kovacic, I., & Brennan, M. J. The Duffing equation: nonlinear oscillators and their behaviour. John Wiley & Sons. 2011. pp. 28-29.

[111] Spong, M. W. The swing up control problem for the acrobot. *IEEE Control Syst. Mag.* **1995**, *15*, 49-55.

[112] Nijmeijer, H.; Berghuis, H. On Lyapunov control of the Duffing equation. *IEEE Trans. Circuits Syst. I. Fundam. Theory Appl.* **1995**, *42*, 473-477

[113] Sandberg, I. W. On the response of nonlinear control systems to periodic input signals. *Bell Syst. Tech. J.* **1964**, *43*, 911-926.

Appendix A: Development of AIGAMO-I: A Remote Controlled Weeding Robot for Organic Rice Farming

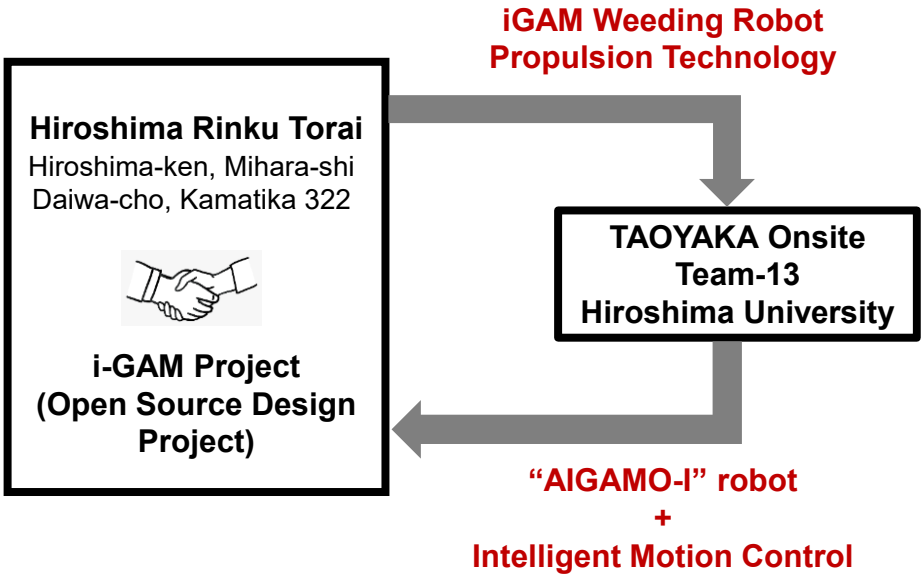

Fig. A.1. Overview of the TAOYAKA Onsite Team Project

The TAOYAKA Onsite Team Project is a project carried out under the flagship of TAOYAKA Program for Leading Graduate Schools. The project title was "Development of a Weeding Robot to Support Organic Rice Farmers". Under the project a remote-controlled weeding robot, "AIGAMO-I". First, a prototype was developed and tested for its buoyancy. Then the robot-body is re-designed and 3D-printed. The robot was tested in the Monozukuri Plaza, Hiroshima University. The project overview is shown in Fig A.1. The development involved close-cooperation with local community like Hiroshima Rinku Torai in Mihara, Hiroshima Prefecture of Japan. The community was using a very primitive design of a robot which they named "i-GAM". The robot was integrated with two 12V DC motors running two screw-propellers. The motors were pre-programmed about the direction of rotation, and based on the direction the robot was changing its direction of movement in the field. The robot moved randomly in different directions.

The robot had two main problems. First, it was pre-programmed which makes its movement very much restricted in the field. Second, it was not enabled with any motion control system. The author of this thesis attempted to solve these two problems. The target of the project was to develop the motion control technology for the robot and give back to

the community. The developed robot was tested in the university workshop, but unfortunately could not tested in the rice field due to lack of the time. The one-year long project finished in the month of April, 2019. Though the project finished officially, the research group has continued the development of the robot and envisioned to give it back to the community in the near future. The timeline of the project is shown in Fig. A.2 and the robot is shown in Fig. A.3.

Fig. A.2. The timeline of the development of the weeding robot AIGAMO-I

Physical parameters	
Dimension	30 19 10 cm
Weight	3.5 Kg
Motor	Brushed DC
Control Board	Arduino Uno
Motor Shield	LM358
IMU	MPU6050 1
RF Transceiver	nrF24L01 1
Battery	12 V 2

Fig. A.3. Weeding robot AIGAMO-I (right) and the principal physical parameters (left).

List of Publications

A. Transactions/ International Journal Papers

A-(1) **Sunandan Dutta**, Mitiko Miura-Mattausch, Yoshihiro Ochi, Naoto Yorino and Hans Jürgen Mattausch, "Gyro-Sensor-Based Vibration Control for Dynamic Humanoid-Robot Walking on Inclined Surfaces," *Sensors*, Vol. 20, 7139, Dec. 2020.

A-(2) **Sunandan Dutta**, Tapas Kumar Maiti, Mitiko Miura-Mattausch, Yoshihiro Ochi, Naoto Yorino and Hans Jürgen Mattausch, "Analysis of Sensor-Based Real-Time Balancing of Humanoid Robots on Inclined Surfaces," *IEEE Access*, Vol. 8, pp. 212327-212338, Dec. 2020.

B. International Conference Papers Related to This Thesis

B-(1) **Sunandan Dutta**, Tapas Kumar Maiti, Yoshihiro Ochi, Mitiko Miura-Mattausch, Sandip Bhattacharya, Naoto Yorino, Hans Jürgen Mattausch, "Stability Analysis of Humanoid Robots with Gyro Sensors Subjected to External Push Forces," *Proceedings of the 2nd International Symposium on Devices, Circuits and Systems (ISDCS 2019)*, pp.1-4, Mar.4 - 6, 2019, Hiroshima, Japan.

B-(2) **Sunandan Dutta**, Tapas Kumar Maiti, Yoshihiro Ochi, Mitiko Miura-Mattausch, Sandip Bhattacharya, Naoto Yorino, Hans Jürgen Mattausch, "Self-controlled walking robot with gyro sensor network for stable movement on non-smooth surfaces," *Proceedings of the IEEE International Conference on Simulation, Modeling and Programming for Autonomous Robots (SIMPAR 2018)*, pp.137-143, May.16 - 18, 2018, Brisbane, Australia.

.

Contents of the Thesis and Published Papers Relationship

Chapters	Title of chapters	Published papers
Chapter 1	Introduction	A-(1), A-(2), B-(1), B-(2)
Chapter 2	Literature Review	A-(1), A-(2), B-(1), B-(2)
Chapter 3	Force Sensor Based Postural Stability Control	A-(2)
Chapter 4	Gyro Senor Based Postural Stability Control	B-(1), B-(2)
Chapter 5	Vibration Control in Humanoid Robots	A-(1)
Chapter 6	Conclusions and Future works	A-(1), A-(2), B-(1), B-(2)